Title
Aortic intimal resident macrophages are essential for maintenance of the non-thrombogenic intravascular state

Author
Hernandez, Gloria Elise

Publication Date
2021

Peer reviewed|Thesis/dissertation

UNIVERSITY OF CALIFORNIA
Los Angeles

Aortic intimal resident macrophages are essential for maintenance of the non-thrombogenic intravascular state

A dissertation submitted
in partial satisfaction of the requirements for the degree Doctor of Philosophy
in Molecular Biology

by

Gloria Elise Hernandez

2021

ABSTRACT OF DISSERTATION

Aortic intimal resident macrophages are essential for maintenance of the non-thrombogenic intravascular state

by

Gloria Elise Hernandez
Doctorate of Philosophy, Molecular Biology
University of California, Los Angeles 2021
Professor M.Luisa Iruela-Arispe, Co-Chair
Professor A. Jake Lusis, Co-Chair

Despite advances in our understanding of cardiovascular risk factors, cardiovascular disease (CVD) continues to be the leading cause of mortality worldwide. The underlying pathology involved in many forms of CVD is atherosclerosis, a condition characterized by lipid deposition and chronic inflammation within the arterial wall of large blood vessels. The aorta is the largest artery of the body and subjected to significant physical forces due to the pressure of blood emanating from the heat. In this manner, distinct areas of the aorta are subjected to oscillatory, laminar, disturbed, and pulsatile flow due to their shape and proximity to the heart. Regions that experience oscillatory or “disturbed” blood flow are prone to developing atherosclerotic plaques whereas regions that experience uniform laminar flow are athero-protected. Further understanding of how different flow dynamics impact the tunica intima during homeostasis will help clarify the differential impact of distinct types of physiological shear stresses and the unique region-specific susceptibilities to disease development.

Here, we show that the closure of the ductus arteriosus immediately post-birth initiates drastic hemodynamic changes in the aorta. Using single-cell RNA-sequencing, we found that the closure of the ductus arteriosus requires vimentin, the most abundant intermediate filament in vascular cells. Deletion of vimentin in mice caused patent ductus arteriosus, a congenital heart defect where the ductus fails to close. Additionally, we identified a tissue-resident macrophage population that is not pathologically induced, instead it is developmentally programmed to cope with the natural hemodynamic changes at birth that result in localized disturbed flow dynamics. This aortic intima-resident macrophage (Mac^{AIR}) population shares the luminal surface with the endothelium becoming interwoven in the tunica intima. Moreover, we found that Mac^{AIRs} are essential to regulate thrombin activity and clear fibrin deposits in regions of turbulent blood flow. Infection with SARS-Cov-2 also promoted rapid loss of intimal macrophages and robust accumulation of intravascular fibrin on the surface of the endothelium in infected rhesus macaque. These findings advance our knowledge of how vascular endothelial cells profit from this unique interaction with macrophages to preserve a non-thrombogenic surface, prevent intravascular clotting, and ensure vascular health.

This dissertation of Gloria Elise Hernandez is approved.

Timothy O'Sullivan

Thomas Vondriska

Elaine F. Reed

M. Luisa Iruela-Arispe, Committee Co-Chair

Jake Lusis, Committee Co-Chair

University of California, Los Angeles

2021

Dedication

To my mother Nancy Shaul, who sacrificed so much and worked so hard so that I may have the opportunity to follow my dreams

To my beloved grandparents Tony Fortes, Solidad Fortes, and Pauline Hasting.

Table of contents

LIST OF FIGURES

ACKNOWLEDGEMENTS

Pursuing a Ph.D. and a career in research has been the most challenging and the most fulfilling experience, and I have many people to thank for their help and encouragement along the way.

I would like to thank my thesis advisor Dr. Luisa Iruela-Arispe for her unconditional support of my personal and academic career. Thank you for taking a chance and believing in me and for all your amazing mentorship. You provided the perfect research environment for me to grow as a scientist and as a person and pushed me to reach my full potential. You are such a rare and special mentor and even though we had to move halfway across the county, I would have followed you anywhere. Also, thank you for making science fun and exciting. I will always cherish our fun times in the mouse room together.

Thank you to all the Arispe lab members for your constant support, extensive discussions, and fun times in lab, especially the undergraduate students I mentored, including Guadalupe Martinez and Nadia Firozabadi. A special thank you to our amazing lab and mouse colony managers Snezana Mirkov and Michelle Steele. I am also grateful for the constant support from the administration and staff within the UCLA MBIDP and GPB, including Dr. Jeff Long, Dr.Greg Pagyne, Dr. Luisa Iruela-Arispe, Dr. Hillary Collar, Helen Houldsworth, Ashley TerHorst, Stephanie Cuellar, and Vanessa Gonzalez.

I would also like to acknowledge my previous mentors who introduced me to the exciting world of research and at a critical time in my career, infused me with the necessary self-confidence to pursue a career in the sciences, including Dr. Anna Beaudin and Dr. Camilla Forsberg.

I would like to thank my fiancé Justin Kwai and my brother Nick Hernandez as well as the rest of my family and my friends, who encouraged and supported my interest in science. Thank you for being my community that I leaned on. I could not have gotten through graduate school without this amazing support system.

Finally, I would like to extend my most heartfelt thank you to my parents, Nancy and Jae Shaul, and Jimmie Hernandez, for being my greatest inspiration and without whose love and support I would not be here. All that I am, I owe you. Thank you for always believing in me.

Chapter 1 was adapted from Hernandez GE and Iruela-Arispe ML (2020). “The many flavors of monocyte / macrophage-endothelial cell interactions.” *Current Opinion of Hematology 27(3):181-189.* PMID:32167947. We would like to acknowledge Dr. Jesse Williams for his review and edits. We would like to apologize to all the authors whose work could not be cited due to space limitations. Figures were created with BioRender. Funding was provided by from a grant from the National Institutes of Health (R35HL140014). GEH is supported by Howard Hughes Medical Institute Gilliam Fellowship (GT11560). Authorship contributions were Writing, Review, and Editing – GEH, MIA.

Chapter 2 was adapted from Ma F*, Hernandez GE*, Romay M, Iruela-Arispe ML (2021). “Single-cell RNA sequencing to study vascular diversity and function.” *Current Opinion of Hematology 28(3):221-229.* PMID:33714967. Figures were created using BioRender. This work was supported from a grant from the National Institutes of Health (R35HL140014). FM is supported by the US Department of Energy Office of Science under Award DE-FC02-02ER63421. MR is supported by the National Institutes of Health Ruth L. Kirschstein National Research Service Award (5T32HL134633-4) and GEH is supported by Howard Hughes Medical Institute Gilliam Fellowship (GT11560). Authorship contributions were: Review -MR, Writing, Review, and Editing – MF, GEH, MIA (*Contributed equally).

Chapter 3 is unpublished data that is currently under peer-review at Arteriosclerosis, Thrombosis and Vascular Biology (ATVB). It reflects work performed by from Salvador J*, Hernandez GE*, Ma F, Pellegrini M, Goldman R, Ridge KM, Iruela-Arispe ML (2021). This work was supported from a grant from the National Institutes of Health (R35HL140014) and GEH is supported by Howard Hughes Medical Institute Gilliam Fellowship (GT11560). We would like to thank the Broad Stem Cell Research Center (BSCRC) and Jonsson Comprehensive Center

(JCC) at UCLA for sequencing of scRNAseq libraries; the BSCRC flow core at UCLA and the Mouse Histology and Phenotyping core at Northwestern University (NU). A special thanks to Michelle Steel and Snezana Mirkov for managing animal colonies and for assistance with husbandry and animal experiments.

Chapter 4 was adapted from Hernandez GE, Ma F, Martinez G, Firozabadi NB, Salvador J, Juang LJ, Leung J, Zhao P, López DA, Ardehali R, Beaudin AE, Kastrup CJ, Pellegrini M, Flick MJ, Iruela-Arispe ML (2021). "Aortic intimal resident macrophages are essential for maintenance of the non-thrombogenic intravascular state." *In press, Nature Cardio Vascular Researh.* We are grateful to Gwedalyn Randolph and Jesse Williams for the extensive discussions about intima resident macrophages and for the generous transfer of the Cx3cr1^{creERT};CSF1R^{lslDTR} transgenic mouse. We are also thankful to William Mueller for Pecam1 antibodies. We are thankful to Karen Ridge for the generous transfer of the Vimentin-/- mice. We also would like to thank the Broad Stem Cell Research Center (BSCRC) and Jonsson Comprehensive Center (JCC) at UCLA for sequencing of scRNAseq libraries; the BSCRC flow core at UCLA and the Robert H. Lurie Comprehensive Cancer Center (RHLCCC) flow core at Northwestern University (NU), Feinberg School of Medicine; the Mouse Histology and Phenotyping core at NU; and the Center for Advanced Microscopy at NU.A special thanks to Michelle Steel and Snezana Mirkov for managing animal colonies and for assistance with husbandry and animal experiments. Additionally, thank you to Samuel Buchanan for help with cell size quantifications. We would also like to thank Farida V. Korobova from the Center for Advanced Microscopy at NU for support with the Scanning Electron Microscopy. We thank the members of the Arispe lab and the Feinberg Cardiovascular and Renal Research Institute at Northwestern University for extensive discussions. Illustrations were created with BioRender.com. This work was supported by R35HL140014 to M.L. Iruela-Arispe and Howard Hughes Medical Institute Gilliam Fellowship (GT11560) to Gloria Hernandez. DAL is supported by NIH/NICHD training grant T32HD007491.

Chapter 5 is unpublished data. It reflects work performed by Hernandez GE, Ma F, Firozabadi NB, Carias AM, Madden P, Wang X, Veazey RS, Blair RV, Roy CJ, Dodson A, Zouantcha S, Cook A, Lewis MG, Potter EL, Todd JP, Oederer M, Hope, TJ, and Iruela-Arispe ML. We would like to acknowledge the Tulane National Primate Research Center (Covington, LA) and Bioqual Inc. (Rockville, MD) for their help in the primate studies. Illustrations were created with BioRender.com. This work was supported by R35HL140014 to M.L. Iruela-Arispe and Howard Hughes Medical Institute Gilliam Fellowship (GT11560) to Gloria Hernandez.

VITA

EDUCATION

University of California, Los Angeles 2016 to present
Doctorate of Philosophy Candidate in Molecular Biology, Cell and Developmental Biology concentration
Thesis: Aortic Intimal Resident Macrophages are Essential for Maintenance of the Non-thrombogenic Intravascular State
Advisor: Dr. Luisa Iruela-Arispe
(Arispe Lab relocated to Northwestern University, November 2019)

University of California, Santa Cruz 2010 to 2014
Bachelor of Science in Bioengineering, Molecular Biology concentration, Honors in Major

FUNDING

- Howard Hughes Medical Institute (HHMI) Gilliam Fellowship (#GT11560), 2019 to present
- F31 Ruth L. Kirschstein National Research Service Award (NRSA) Individual Predoctoral Fellowship to Promote Diversity in Health-Related Research, PA-18-666, 2019 (award declined).
- Vascular Biology Training (VBTG) Grant, UCLA, Ruth L. Kirschstein National Research Service Award T32HL069766U, 2018-2019 (accepted) and 2019-2020 (award declined)

HONORS AND AWARDS

- Best Talk, Young Investigators Meeting, Kloster Seeon Meeting—Angiogensis. Seeon-Seebruck, Germany, 2021
- 3rd Place Poster Prize, Kloster Seeon Meeting—Angiogenesis. Seeon-Seebruck, Germany, 2021.
- National Science Foundation (NSF) Graduate Research Fellowship Program (GRFP), List of Honorable Mention 2018
- Ford Foundation Predoctoral Fellowship, List of Honorable Mention 2018
- Honors in Major, 2014

TEACHING EXPERIENCE

Research Mentor
Nadia Firozabadi (Undergraduate Researcher), *Northwestern University* March 2020 to present
Maya Kardouh, (Undergraduate Researcher), *UCLA* June 2019 to October 2019
Guadalupe Martinez (Undergraduate Researcher), *UCLA* August 2018 to October 2019
Teaching Assistant Fall Quarter, 2017 and 2018
University of California, Los Angeles
Course Title: Molecular, Cellular and Developmental Biology (MCDB) 165A, Biology of the Cell

LEADERSHIP EXPERIENCE

Co-organizer of the 5th Young Investigators Meeting, Kloster Seeon Meeting--Angiogenesis
Seeon-Seebruck, Germany, September 2021
Co-Chair of the Scientific Excellence through Diversity Seminar (SEDS) Series
University of California, Los Angeles, August 2018- October 2019
Administrator Chair of the Association of Multi-Ethnic Bioscientists' Advancement (AMEBA)
University of California, Los Angeles, June 2018- September 2021

PUBLICATIONS

- Ma F*, **Hernandez GE***, Romay M, Iruela-Arispe ML. Single-cell RNA sequencing to study vascular diversity and function. *Curr Opin Hematol. 28(3):221-229*. PMID: 33714967 *Contributed equally to this review
- Hilfenhaus G, Campos A, Freshman J, Prajapati D, **Hernandez GE**, et al,. High-content screen identifies drugs that restrict tumor cell extravasation across the endothelial barrier. *Cancer Research*. 81(3):619-633. PMID: 33218969.

• **Hernandez GE**, Iruela-Arispe ML. 2020. The many flavors of monocyte / macrophage-endothelial cell interactions. *Current Opinion of Hematology 27(3):181-189.* PMID: 32167947
• McDonald AI, Shirali AS, Aragon R, Feiyang M, **Hernandez GE**, et al., 2018. Endothelial regeneration of large vessels is a biphasic process driven by local cells with distinct proliferative capabilities. *Cell Stem Cell.* 23: 210-225. PMCID: PMC30075129
• Ziyad S, Riordan JD, Cavanaugh AM, Su T, **Hernandez GE**, et al., 2018. A forward genetic screen targeting the endothelium reveals a regulatory role for the lipid kinase Pi4ka in myelo- and erythropoiesis. *Cell Reports 22(5):1211-1224*. PMCID: PMC58280303
• Beaudin AE, Boyer SW, Perez-Cunningham J, **Hernandez GE**, et al., 2016. A Transient developmental hematopoietic stem cell gives rise to innate-like B and T cells. *Cell Stem Cell 19, 1-16.* PMCID: PMC5524382

Manuscripts In Press/Under Review:
•**Hernandez GE**, Ma F, Martinez, G, et al., 2021. Aortic intimal resident macrophages are essential for maintenance of the non-thrombogenic intravascular state. *In Press, Nature Cardiovascular Research*
• Salvador, J*, **Hernandez GE***, et al. 2021 Absence of the intermediate filament results in patent ductus arteriosus. *Submitted, ATVB Brief Reports*. *Contributed equally to this manuscript
•Romay MC, Ma F, **Hernandez GE**, et al. 2021. Positional transcriptomics shed light on site-specific pathologies of the aorta. *Under review, Circulation.*
•Apostol AC, Lopez DA, Lebish EJ, Valencia CD, Romero-Mulero MC, Pavlovich P, **Hernandez GE**, et al., 2021. Prenatal inflammation perturbs fetal hematopoietic development and causes persistent changes to postnatal immunity. *Under review, Nature Immunology.*
•Romay MC, Ma F, **Hernandez GE**, et al. 2021. Altered cerebral vascular function driven by vessel tortuosity and impaired vascular smooth muscle cell contractility in Notcht3 deficiency. *In preparation*

PROFESSIONAL TALKS
• Young Investigators Meeting (YIM), Kloster Seeon Meeting—Angiogenisis. September 2021.
• Cell and Developmental Biology Trainee Seminar, Northwestern University. May 2020.
• Immunology, Inflammation, Infection and Transplantation (I3T) Research in Progress Seminar Series, UCLA. October 2019
• Molecular Biology Interdepartmental Program (MBIDP) retreat, Lake Arrowhead, CA. September 2019.
• Hematology Club, UCLA. June 2019.
• Program Project Grant (PPG)—Atherosclerosis seminar, UCLA. April 2019.
• MBIDP Student Seminar, UCLA. March 2019.

POSTER PRESENTATIONS
Presented at Kloster Seeon Meeting—Angiogenisis. Seeon-Seebruck, Germany. September 24-27, 2021.
Presented at Annual HHMI Gilliam Meeting. Virtual. September 21-23, 2020.
Presented at AHA Vascular Discovery: from Genes to Medicine. Virtual. Chicago, IL. May 5-7, 2020
Presented at Annual HHMI Gilliam Meeting. Chevy Chase, MD. September 23-25, 2019
Presented at Gordon Research Conference (GRC)--Angiogenesis. Newport, Rhode Island. August 5, 2019.
Presented at Gordon Research Conference (GRC)--Atherosclerosis. Newry, Maine. June 18, 2019.
Presented at UCLA Molecular, Cellular, and Developmental Biology Retreat. Lake Arrowhead, California. November 20, 2018.
Present at UCLA Cardiovascular Symposium. Los Angeles, California. October 2018.
Presented at UCLA's Molecular Biology Interdepartmental Doctoral Program (MBIDP) retreat. Ventura, California, March 17, 2018.
Presented at UCSC Undergraduate Symposium. Santa Cruz, California, June 12, 2014

Chapter 1. Introduction: The many flavors of monocyte / macrophage—endothelial cell interactions

ABSTRACT

Purpose of review

The well-recognized plasticity and diversity typical of monocytes and macrophages have recently been expanded by the knowledge that additional macrophage lineages originated directly from embryonic progenitors, populate and establish residency in all tissues examined so far. This review aims to summarize our current understanding on the diversity of monocyte/macrophage subtypes associated with the vasculature, their specific origins, and nature of their cross-talk with the endothelium.

Recent findings

Taking stock of the many interactions between the endothelium and monocytes / macrophages reveals a far more intricate and ever-growing depth. In addition to circulating and surveilling the endothelium, monocytes can specifically be differentiated into patrolling cells that crawl on the surface of the endothelium and promote homeostasis. The conversion of classical to patrolling is endothelium-dependent uncovering an important functional link. In addition to patrolling cells, the endothelium also recruits and harbor an intimal-resident myeloid population that resides in the tunica intima in the absence of pathological insults. Moreover, the adventitia is populated with resident macrophages that support blood vessel integrity and prevent fibrosis.

Summary

The last few years have witnessed a significant expansion in our knowledge of the many subtypes of monocytes and macrophages and their corresponding functional interactions with

the vascular wall. In addition to surveying the endothelium for opportunities of diapedeses, monocyte and macrophages take residence in both the intima (as patrolling or resident) and in the adventitia. Their contributions to vascular function are broad and critical to homeostasis, regeneration, and expansion.

Keywords: Blood vessels, collaterals, perivascular, tunica adventitia, tunica intima, vascular inflammation

INTRODUCTION

As the selective gatekeeper between blood and tissues, the endothelium specifically interacts and activates immune cells to facilitate their trafficking. These heterotypic cell interactions are usually brief and are meant to gain access to specific tissue/organ sites. Nonetheless, in contrast to other immune cells, the interactions between endothelium and monocytes/macrophages appear to be far more diverse, interdependent, and specialized.

During developmental angiogenesis, macrophages establish bridges that bring tip cells from adjacent sprouts in proximity facilitating the formation of a new vascular branch [1]. In this manner, macrophages have been acknowledged to actively participate in vascular expansion. Monocyte / macrophages also contribute to angiogenesis through a variety of mechanisms including secretion of VEGF and other cytokines [2], promote intima regeneration [3*], and contribute to collateral growth under hypoxic conditions [2,4]. In small vessels, perivascular macrophages can also regulate permeability responses [*5,6**]. Clearly amongst all bone-marrow derived cells, heterotypic associations between endothelial and monocytes / macrophages are versatile and broad. This wide functional diversity has uncovered the realization of multiple subtypes of monocytes and macrophages that interact with the vascular wall and that are derived from distinct precursors. In fact, blood vessels, particularly in the

adventitia are initially populated by macrophages directly derived from embryonic progenitors and supplemented by infiltrating monocytes that contribute to the resident pool of macrophages post-birth [7**]. How this distinct origin and long-term residency impacts their function in comparison to monocyte-derived macrophages is yet to be understood.

Here we examine a fast-growing body of new information on monocyte / macrophage interactions with the vascular wall. Our objective is to offer a timely and informed summary of the current knowledge on the subject, bringing to light differences in origin, molecular cross-talk with the endothelium and functional relationships.

PATROLLING MONOCYTES

Monocytes circulate and constantly survey the endothelium, in some cases this surveillance results in extravasation. Once in the extravascular space, these highly plastic cells can display wide functional diversity in response to their environment [8]. However, in other cases, interaction with the endothelium does not result in vascular extravasation instead, monocytes constantly crawl on the endothelial surface. These two major monocyte subpopulations can be molecularly identified by their cell surface profile which is shared by both mouse and human [9]. Specifically: $Ly6c^{hi}Ccr2^{hi}Cx3cr1^{lo}$ ($CD14^{+}CD16^{-}$ in humans) defines "**inflammatory**" or **"classical" monocytes** that are abundant and highly responsive to inflammatory signals, these cells can infiltrate tissues and differentiate into macrophages [8]. In contrast, $Ly6c^{lo}Ccr2^{lo}Cx3cr11^{hi}$ ($CD14^{+}CD16^{+}$ in humans), also referred as "**non-classical" or "patrolling" monocytes** patrol the endothelium by crawling along the luminal aspect of blood vessels in both the micro- and macro-vasculature (**Fig. 1.1a**). This second monocyte subtype is thought to support the endothelium and maintain its homeostasis [10,11]. Patrolling monocytes have a half-life of 2.3-12 days [12], depending on the environment, and constantly attaching to the tunica intima of the circulatory system, and interacting with the endothelium [9].

During steady-state, Ly6c^{hi} classical monocytes are the precursors to Ly6c^{low} patrolling monocytes [12]. The process of conversion from classical to patrolling requires contact with the endothelium and activation of the Notch pathway [13*]. Specifically, activation of Notch2 in monocytes by Dll1 in endothelial cells effectively mediates the transition from classical to patrolling in several vascular beds [13*]. In addition to Notch, the transcription factor *Nr4a1* (Nur77) is a critical regulator of patrolling, while not affecting classical monocytes [14]. Several studies have demonstrated that depletion in Nr4a1 impairs differentiation and survival of patrolling monocytes [14–16]. A caveat of these studies is the broad expression of Nr4a1 which could impact related cell subtypes. Recently, two studies further refined the link between Nr4a1 and monocytes. One study performed targeted inactivation of a sub-domain within the Nr4a1 enhancer that is exclusively utilized by patrolling but not other monocytes (**Fig. 1.1a**) [15**]. The other showed a critical role for C/EBPβ in the regulation of Nr4a1 expression during monocyte conversion using a single cell transcriptomics approach [17*]. Both studies confirmed the absolute requirement of Nr4a1 in the conversion of classical to patrolling monocytes. Furthermore, myeloid depletion of Klf2, an upstream regulator of Nr4a1, explicitly reduced patrolling monocytes [15**].

In the microvasculature of the dermis, kidney, and mesentery, patrolling monocytes crawl along the endothelium regardless of the direction of blood flow [16]. However, in large arteries like the carotid, patrolling monocytes preferentially migrate in the direction of blood flow [18**]. The crawling process requires $\alpha_L\beta2$ integrin (or LFA-1), a highly expressed receptor in patrolling monocytes in all healthy tissues [10]. Intracellular adhesion molecule-1 (Icam-1) is the major endothelial ligand for $\alpha_L\beta2$, while Icam-2 enhances, but it is dispensable for adhesion [16]. Besides $\alpha_L\beta2$, the patrolling function of monocytes is thought to require $\alpha_4\beta_1$ (or very-late antigen 4, VLA-4), but alone, $\alpha_4\beta_1$ is unable to fully support this function [18**]. Recently, $\alpha_4\beta_1$ has been implicated in patrolling of renal glomeruli [19].

Patrolling monocytes express high levels of Cx3cr1. Consequently, monoallelic Cx3cr1-GFP knock-in mice ($Cx3cr1^{GFP/+}$) are the most commonly used labeling strategy to distinguish patrolling (GFP^{hi}) versus other monocytes (GFP^{lo}), although this reporter mouse also labels other immune cell populations (i.e. tissue-resident macrophages, dendritic cells, and subsets of NK and T cells) [20]. Deficiency of Cx3cr1 results in an overall reduction of patrolling monocytes; however, motility of these monocytes in the microvasculature and in large arteries is independent of Cx3cr1 [16,18**].

On the endothelial side, in addition to Icam-1/2, patrolling monocyte-endothelial interactions also require the cystein-rich angiogenic inducer 61 (Cyr61 or Ccn1), a matricellular protein with chemoattractant properties for monocytes that is produced and secreted by endothelial cells, fibroblasts, and other cell types [21]. Endothelium bound-Ccn1 promotes efficient surveillance of patrolling monocytes at steady-state, but this molecule is not required for adhesion to the endothelium [21].

Functionally, patrolling monocytes, which express high levels of toll-like receptors (TLRs), behave as the “housekeepers” of the vasculature [16,22]. They have phagocytosis capabilities that allows them to scavenge microparticles and remove cellular debris from the endothelial surface at sites of necrosis in a TLR-7-dependent manner [10,16] (**Fig 1.1b**). In addition, patrolling monocytes have proangiogenic properties and aide in organ repair [3*,23, 24*–26].

Recently, Gitzin et al. showed that following carotid injury, patrolling monocytes are recruited to the endothelium at wound sites to promote endothelial cell proliferation and tissue repair [3*]. In this study, the authors showed that carotid injury induces endothelial cell expression of Cx3cr1 at the wound site which results in the recruitment of patrolling monocytes. Depletion of patrolling monocytes using *Cx3cr1* loss-of-function ($Cx3cr1^{GFP/GFP}$) mice impaired endothelial regeneration. Lastly, *in-vitro* experiments suggest patrolling monocytes mediate endothelial cell proliferation through secretion of Vefg-a [3*].

In disease, patrolling monocytes largely play protective roles and contribute to the resolution of inflammation. During atherosclerosis, patrolling monocytes are functionally atheroprotective [18**,27,28]. Monocyte crawling is increased at early stages of the disease, through CD36-mediated uptake of oxidized lipids (OxLDL) [29*]. Depletion of patrolling monocytes in atherosclerotic models results in aggravated atherosclerosis [18**,28]. Following myocardium infarction, patrolling monocytes are part of a second-wave of inflammatory cell recruitment that aids to repair, promote angiogenesis and improve myofibroblast accumulation, as well as deposition of collagen necessary for granulation tissue formation [23,25]. In renal ischemia reperfusion injury CD169+ monocytes, which include both classical and patrolling, play an anti-inflammatory role by regulating Icam-1 expression on endothelial cells [26]. Mice depleted of Cd169 had exacerbated renal reperfusion injury [26]. To clarify the subset of CD169+ monocytes contributing to the resolution of the pathology, the authors performed adoptive transfer experiments. Transfer of Ly6c^{lo} patrolling monocytes into CD169-depleted mice rescued the mice from lethal renal injury and normalized renal endothelial cell Icam-1 expression levels. These findings indicate that CD169+ Ly6c^{lo} patrolling monocytes play a major role in regulating inflammation in renal reperfusion injury [26]. Additionally, patrolling monocytes contribute to cancer immune-surveillance by orchestrating an antitumor response through recruitment NK cells, and thus, controlling lung metastasis in the mouse [30]. In other diseases, like systemic lupus erythematosus and arthritis, patrolling monocytes have been implicated in the pathogenesis of disease [31,32].

MONOCYTES/MACROPHAGE IN COLLATERAL ARTERIAL REMODELING

In adults, arteriogenesis refers to the growth or remodeling of arteries (collaterals) triggered by the occlusion of an upstream vascular branch. Although the mechanisms of collateral growth are still unclear [4], monocytes and macrophages have been identified as important players in the process.

Studies suggesting the importance of monocyte/macrophages in collateral arteriogenesis can be traced back to the 1970s, when Schaper et al. [33] showed a large number of monocytes adhering to the surface of endothelial cells following canine chronic coronary artery occlusion. Subsequently, monocyte/macrophage accumulation was also noted around collateral arteries in rabbit and murine hindlimb ischemia models [34,35]. Monocyte recruitment requires the upregulation of chemoattractant or activating cytokines and adhesion molecules [36]. During collateral arteriogenesis, the usually quiescent endothelium becomes activated, resulting in the upregulation of Icam-1, vascular cell adhesion molecule-1 (Vcam-1) and chemokines such as monocyte chemoattractant protein 1 (Mcp-1 or Ccl2), amongst others [2,4]. Mcp-1 is the ligand for C-C chemokine receptor (Ccr2), which is required for classical monocyte recruitment [37]. Mcp-1 plays a significant and beneficial role during collateral arteriogenesis. Mice depleted of Mcp-1 (Ccl2-/-) had lower monocyte recruitment, reduced collateral artery regeneration, and low perfusion recovery [37,38]. Furthermore, administration of Mcp-1 during hindlimb ischemia increased collateral artery regeneration [34,39]. Recently, it was shown that nuclear factor of activated T cells 5 (Nfat5) controls Mcp-1 release in endothelial cells during hindlimb ischemia [40*]. Specifically, reduction of Nfat5 by shRNA adenovirus resulted in attenuated arteriogenesis in rat hindlimb ischemia [40*].

Experiments using Ccr2-depleted (Ccr2-/-) mice, where classical monocyte egression from the bone marrow and/or infiltration into damaged tissues is abrogated [41] has also supported a critical role for monocytes in collateral formation [37,42]. Bone-marrow transplantations of Ccr2-/- mice into wild-type recipients (Ccr2-WT) has revealed that both arteriolar remodeling and monocyte/macrophage recruitment are significantly impaired in a dorsal skinfold model of injury [43]. Importantly, not all macrophages are derived from Ccr2 classical monocytes. As previously discussed, a major subset of adventitia-resident macrophages originate from embryonic precursors and proliferate to maintain the lineage through self-renewal [7**]. This subtype of macrophage (tissue-resident) is not affected by Ccr2

depletion and abundantly populate the perivascular wall. It is also possible that these cells, in addition to monocyte-derived macrophages, contribute to collateral formation.

In myocardial infarction and hindlimb ischemia, early invading Ly6c^{hi} monocytes give rise to ischemic macrophages that undergo phenotypic changes overtime [25,44*]. What exactly promotes macrophage differentiation and maturation in ischemic tissue? Previously it has been shown that endothelial cells can promote macrophage polarization [5*]. Further supporting this concept, Krishnasamy et al. [44*] recently showed that macrophage maturation from Ly6c^{hi} monocytes and inflammatory polarization after hindlimb ischemia is regulated by endothelial Dll1. Mice with either endothelial-specific deletion of Dll1 (*Dll1* $^{i\Delta EC}$) or myeloid cell-specific Notch-deficiency not only exhibited a low perfusion recovery and a reduction in collateral branch formation, but also in low macrophage numbers and macrophage activation state [44*]. Therefore, monocyte-derived macrophage maturation is dependent on canonical Notch signaling, which is essential for collateral arteriogenesis following ischemia. Additionally, monocytes/macrophages are believed to be the major source of matrix metalloproteinases (Mmps) and other growth factors like vascular endothelial growth factor (Vegf), which leads to the rearrangement of extracellular matrix and remodeling of arterioles [37,45,46]. Whether monocyte-derived macrophages or adventitia-resident macrophages are the most critical source of these secreted proteins for collateral formation is not yet fully understood. Defined lineage-tracing experiments could help clarify the individual and overlapping contributions of these two subpopulations associated with the vascular wall.

ARTERIAL “ADVENTITIA-RESIDENT” MACROPHAGES

Genetic tracing studies and others have shown that arterial “adventitia-resident” macrophages densely populate the tunica adventitia: the outermost layer of connective tissue common to all blood vessels [6**,7**,47**]. These cells can be recognized by expression of Lyve-1, as well as

Csf1r (CD115), CD11b, F4/80, and CD64 (FcγR1), and CD206 [6**,7**,47**,48**]. As other macrophages, adventitia-resident macrophages are dependent on Csfr1-Csf1 signaling for survival and their maintenance requires Cx3cr1 activation, where endothelial cells and Pdgfrα+ mesenchymal cells constitute the primary source of Cx3cl1 [7**,47**].

In recent years, our knowledge of the ontogeny of tissue-resident macrophages has changed drastically. It is now understood that most tissue-resident macrophages arise from embryonic precursors, that seed tissues during development. These cells are capable of self-renewal and fully independent of bone marrow-derived cells [12,49,50] (**Fig. 1.1a**). Two waves of precursors have been reported for adventitial macrophages. Tracing studies identified Cx3cr1+ embryonic progenitors as a definitive source of adventitial macrophages. These cells are observed by embryonic day 16.5 (E16.5) in the mouse aorta [7**]. Subsequently, the adventitia receives a second wave of precursors, this time originated from circulating monocytes. In adulthood, adventitia-resident macrophages are maintained via self-renewal, independent of circulating monocytes [7**]. In addition, following bacterial (LPS) infection, adventitia-resident macrophages are severely depleted, but eventually reach steady-state levels through self-renewal [7**].

In terms of cell-surface profile, a recent study have identified two independent populations of monocyte-derived tissue-resident macrophages characterized by distinct gene expression profiles: Lyve^{lo}MHCII^{hi}Cx3cr1^{hi} (Lyve^{lo}MHCII^{hi}) and Lyve1^{hi}MHCII^{lo}Cx3cr1^{lo} (Lyve1^{hi}MHCII^{lo}), the latter speaks to adventitia-resident macrophages [6**]. These parallel populations were found in the heart, fat, dermis, and lung, as well as in human lung and fat [6**]. This study elegantly showed specific niches to these two macrophage populations, concluding that Lyve^{lo}MHCII^{hi} macrophages preferentially reside adjacent to nerve bundles and fibers whereas Lyve1^{hi}MHCII^{lo} macrophages are prevalent to blood vessels across tissues [6**]. Specific depletion of Lyve1^{hi}MHCII^{lo} macrophages in a mouse model resulted in exacerbated experimental lung and heart fibrosis [6**]. The authors conclude that Lyve1^{hi}MHCII^{lo}

macrophages support blood vessel integrity at steady-state since depletion of these macrophages leads to better infiltration of monocytes and other inflammatory cells upon fibrosis.

In general, tissue-resident macrophages have a diverse array of functions; in addition to their conventional immune regulation, they also participate in homeostasis, repair and angiogenesis [5,49,50]. For example, embryonic tissue macrophages in the brain act as fusion cells that physically bridge tip cells of sprouting vessels to promote vascular anastomosis [1]. Specifically in relation to adventitial-resident macrophages, depletion studies using Csf1r inhibitors or *Lyve1*$^{wt/cre}$;*Csf1r*$^{flox/flox}$ mice resulted in an increase in collagen deposition within the arterial wall and arterial stiffnes [47**]. *In vitro* co-culture experiments further suggested that adventitia-resident macrophages regulate collagen content via Mmp9-dependent proteolysis [47**]. Since Lyve-1 is the receptor for the extracellular matrix glycosaminoglycan hyaluronan (HA), blocking antibodies were used against the Lyve-1 binding site, which resulted in the reduction of collagen degradation *in vitro* [47**]. Therefore, the authors speculate that adventitia-resident macrophages regulate collagen levels through HA-dependent smooth muscle cell adhesion and thus, modulate smooth muscle cell function.

INTIMAL CD11C+ MYELOID CELLS

Endothelial cells provide an antithrombotic surface by forming tight barriers through homotypic cell interactions that effectively separate the blood from the surrounding tissues. In general, only under inflammatory conditions are endothelial cells capable of recruiting immune cells and form transient heterotypic interactions that promote their extravasation at sites of inflammation. However, in large arteries there appears to be an exception to the transient nature of these interactions. Early morphological observations have suggested that a **resident myeloid population** might occupy the intimal layer of healthy (uninflamed) vessels in regions of turbulent flow like the lesser curvature of aortic arch, bifurcation, and branch openings [51,52].

In healthy C57BL/6 mice, an intimal CD11c+ myeloid cell population was also observed in the aorta at regions that experience disturbed blood flow (**Fig. 2.2a**) [53,54]. Very rarely were these CD11c+ myeloid cells described in the intima of the descending aorta, which experiences uniform laminar flow, suggesting that their recruitment and/or residency might be flow-type dependent [54]. Intimal CD11c+ myeloid cells increase with age in the ascending aorta and were found to populate the thoracic aorta of 60wk old mice [55]. These myeloid cells reside in the subintimal space with long cellular processes projecting into the lumen [53,54]. Collectively, these intimal cells are CD11c+, MHCII+, CD68+, Cx3cr1+ as validated by immunofluorescence and reporter mice [53–55]. Additionally, they express the dendritic markers αEβ7 (CD103) [56] and 33d1, although the latter remains controversial [56–58]. A previous study showed that FACS sorted CD11c+MHCII+ aortic cells have low phagocytic activity and are strong stimulators of T-cell proliferation, functionally supporting their classification as dendritic cells [56]. However, their identity as *dendritic* or *macrophage* is still in under debate. Using single-cell RNAseq Chakarov et al. [6**] recently characterized a tissue-resident macrophage population with a conserved phenotype across tissues. The profile identified by the authors matches the aortic intimal CD11c+ myeloid population. This finding prompts the question: Are the aortic intimal immune cells actually macrophages? Detailed transcriptomic profiling using single cell RNA-sequencing combined with precise immunofluorescence could help elucidate the cellular identity of the CD11c+ myeloid cells.

The accumulation of intimal CD11c+ myeloid cells seems to be partially dependent on Cx3cr1. In Cx3cr1-defiecient mice, there is 40% less CD11c+ myeloid cells in the ascending aorta [55]. Furthermore, intimal CD11c+ myeloid cells are believed to be Flt3L-dependent [56]. Treatment of Flt3L increases intimal CD11c+ cells by 2.5 fold and the number of these intimal myeloid cells were remarkably reduced in Flt3-/- mice [56]. Using BrdU labeling experiments, it is believed that there is a low-grade contribution of recruited blood monocytes to the normal

intima that serve as the predominant source of intimal CD11c+ myeloid cells [54]. However, additional studies involving parabiosis, transplants, and lineage tracing are needed to further advance our understanding on how intimal CD11c+ myeloid cells are maintained throughout adulthood. Moreover, at what age do CD11c+ myeloid cells seed the intima of the aorta? Understanding their origin could shed light into their physiological roles.

The function of intimal CD11c+ myeloid cells remains unknown. What is the relationship between these myeloid cells and endothelial cells? Are these myeloid cells necessary to maintain vascular homeostasis? Paulson et al. [57] showed that a single injection of tamoxifen to mice bearing the CD11c promoter-DTR transgene (CD11c-DTR mice) depletes the intimal myeloid cells by approximately 98% after 24hrs post-injection. Interestingly, approximately 75% of intimal CD11c+ myeloid cells are recovered by 21-days post-depletion and are re-localized to the lesser curvature of the aortic arch [57]. This implies the necessity for these cells by the endothelium in this region. Further studies to define the consequences of depletion of intimal CD11c+ cells in vascular homeostasis are still needed.

Recently, Roufaiel et al., [59*] showed that intimal CD11c+ myeloid cells have the potential to clear *chlamydia muridarum* in the arterial wall through reverse transendothelial migration (**Fig. 2.2b**). Upon infection of *chlamydia muridarum* (or with injection of LPS and PolyIC), there is a decrease in the number of intimal CD11c+ myeloid cells in the ascending aortic arch. Consequently, clearance of *chlamydia muridarum* 16S rRNA in the intima correlated with the reduction of CD11c+ myeloid cells present in the intima [59*]. These findings indicate that intimal CD11c+ myeloid cells have important innate-like functions in the normal artery.

The location of intimal CD11c+ myeloid cell makes them likely suspects in the initiation of atherosclerosis. Intimal CD11c+ myeloid cells are capable of uptaking neutral lipids just after 5 days of high-fat diet in Ldlr-depleted (Ldlr-/-) mice, a popular atherosclerotic model (**Fig. 2.2c**) [57]. Depleting these cells using CD11c-DTR mice crossed to Ldlr-/- mice prior to the induction of hypercholesterolemia resulted in the overall reduction of early lipid accumulation in the aortic

wall [57]. In addition, lipid accumulation was found only in extracellular spaces, suggesting intimal CD11c+ myeloid cells play a role in lipid endocytosis during the earliest stages of plaque formation [57]. It has been suggested that the “resident” intimal CD11c+ cells significantly increase in number in advanced atherosclerosis based on the number of CD11c+MCII+ cells present [56]. Although expansion of cells matching this phenotype is evident, it is difficult to discriminate between the resident *versus* the recruited immune cell populations based on these markers alone since recruited cells can adopt these phenotypes [56,58]. Additionally, there is remarkable immune cell heterogeneity in atherosclerotic aorta. Recent scRNAseq studies identified up to 11 distinct leukocyte populations in the atherosclerotic aorta when compared to control aortas, with diverse macrophage and dendritic cell populations [48**,60**]. Therefore, lineage tracing experiments during the different stages of atherosclerosis are needed to enable the distinction between resident and *de novo* recruited cells.

CONCLUSIONS

In the last five years, our understanding of the spectrum of endothelial – monocyte / macrophage has significantly expanded along with the realization that macrophages do take long-term residence in organs, including the vascular wall. Their roles are broad and, not surprisingly, dependent on environmental conditions.

Research focus would benefit from combinatorial studies that bring lineage tracing and functional analysis in the context of both physiological and pathological conditions. Major obstacles in clarifying specific functions relate to the potential for functional compensation. Thus, studies that aim at understanding cellular redundancy by selectively eliminating lineages at specific times and sites would aid in clarifying to what degree can monocytes substitute for developmentally-derived long-term lineages. As the functional interdependencies between endothelium and mononuclear lineages become untangled, the information will expand our

ability to systematically evaluate how cell-cell interactions impacts tissue adaptability and resilience to stressors.

ACKNOWLEDGEMENT

We would like to acknowledge Dr. Jesse Williams for his review and edits. We would like to apologize to all the authors whose work could not be cited due to space limitations. Figures were created with BioRender.

FINANCIAL SUPPORT AND SPONSORSHIP

This work was supported from a grant from the National Institutes of Health (R35HL140014). GEH is supported by Howard Hughes Medical Institute Gilliam Fellowship (GT11560).

CONFLICTS OF INTEREST

There are no conflicts of interests.

FIGURES

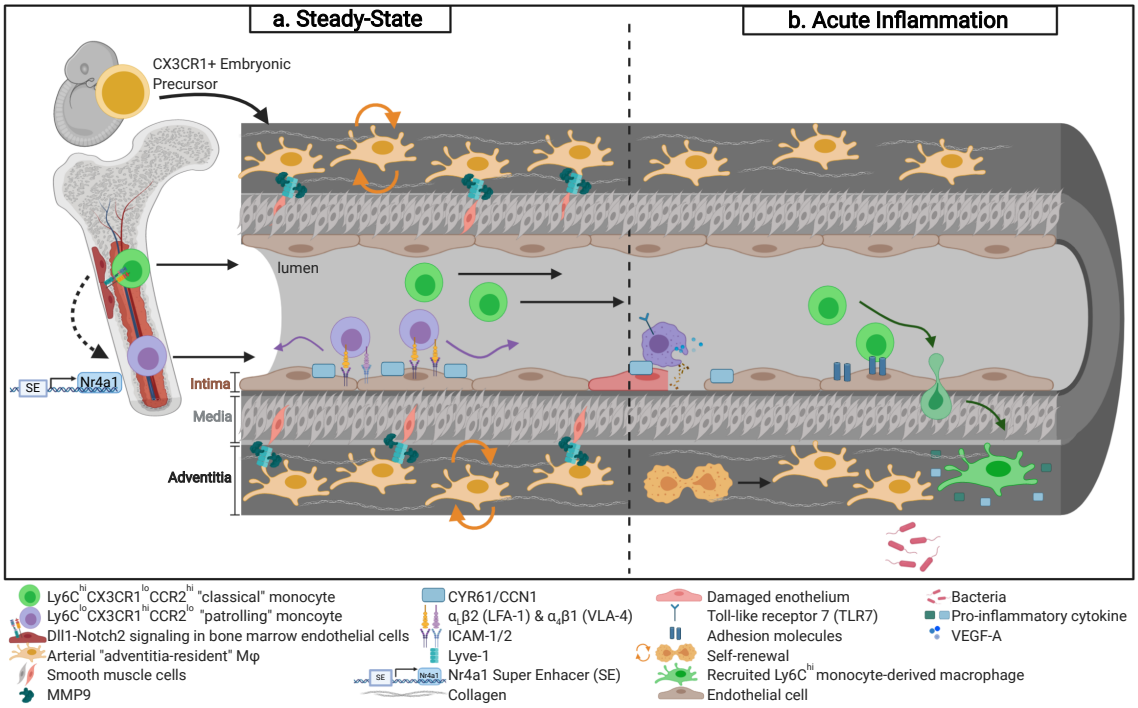

Figure 1.1. Recruitment and dynamics of vascular and perivascular monocyte/macrophages

(a) Arterial “adventitia-resident” macrophages are derived from CX3CR1+ embryonic precursors and seed the perivasculature prior to birth (orange cells). Throughout adulthood, adventitia-resident macrophages are maintained by self-renewal. Adventitia-resident macrophages regulate collagen content via matrix metalloproteinase-p (Mmp9) proteolysis, which is dependent on Lyve-1 and smooth muscle cell binding. At stead-state, Ly6C^{hi} classical monocytes (in green) are the precursors to Ly6C^{lo} patrolling monocytes (in purple). Monocyte conversion is dependent on Dll1/Notch2 signaling in distinct vascular beds. Additionally, Nr4a1 super enhancer regulates patrolling monocyte development and is essential for monocyte survival. In the circulation, patrolling monocytes crawling requires $\alpha_L\beta2$ integrin (or LFA-1) and other adhesion molecules highlighted. Furthermore, endothelial cystein-rich angiogenic inducer 61 (Cyr61 or Ccn1) promotes efficient surveillance. (b) Patrolling monocytes remove cellular debris from the endothelial surface at sites of necrosis in a TLR-7-dependent manner. At sites of injured endothelium, patrolling monocytes may facilitate endothelial proliferation through secretion of Vegfa. Moreover, activated endothelium upregulates adhesion molecules that enable monocyte capture, rolling, and extravasation into tissue and migrate to inflammatory stimuli. Recruited monocytes differentiate into macrophages as part of a pro-inflammatory

response. Adventitia-resident macrophages are severely depleted during bacterial infection but are able to regain steady-state levels through self-renewal.

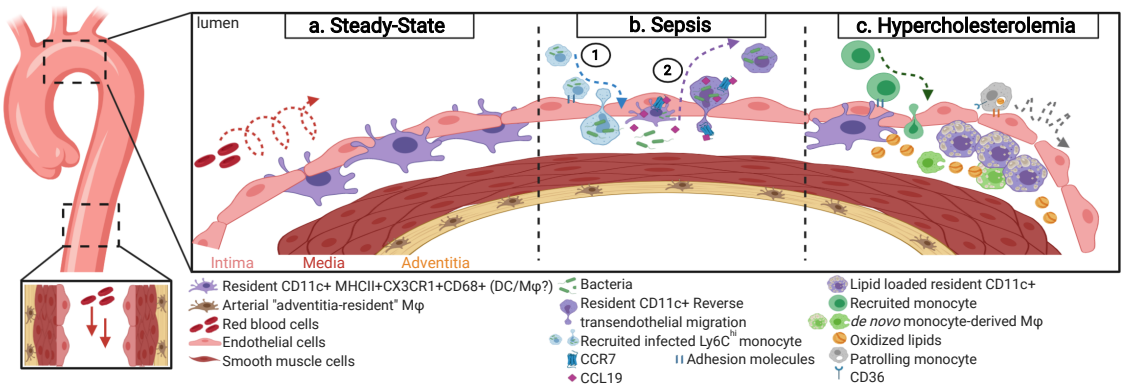

Figure 1.2. Intimal resident CD11c+ myeloid cells in arteries during health and disease

(a) In regions that experience disturb blood flow, like the lesser curvature of the aortic arch, resident CD11c+ myeloid cells (in purple) accumulate in the subintimal space of healthy aortae. Resident CD11c+ myeloid cells rarely accumulate in descending aortae, which experiences uniform laminar blood flow. (b) 1. Circulating monocytes (in blue) become infected with bacteria, gain access to the subintima space, and disseminate the infection. 2. Upon infection, resident CD11c+ myeloid cells upregulate Ccl19 and Ccr7, which is necessary for these cells clear the infection via reverse transendothelial migration, and enter the circulation. (c) At early stages of hypercholesterolemia, resident CD11c+ myeloid cells uptake oxidized lipids, contributing to the initial lesion bed. Additionally, CD36-mediate uptake of oxidized lipid by patrolling monocytes increases crawling.

REFERENCES

Papers of particular interest, published within the annual period of review, have been highlighted as:

* of special interest

** of outstanding interest

1. Fantin A, Vieira JM, Gestri G, et al. Tissue macrophages act as cellular chaperones for vascular anastomosis downstream of VEGF-mediated endothelial tip cell induction. Blood. 2010;116:829–840.

2. Corliss BA, Azimi MS, Munson JM, et al. Macrophages: an inflammatory link between angiogenesis and lymphangiogenesis. Microcirculation. 2016;23:95–121.

3*. Getzin T, Krishnasamy K, Gamrekelashvili J, et al. The chemokine receptor CX3CR1 coordinates monocyte recruitment and endothelial regeneration after arterial injury. EMBO Mol. Med. 2018;10:151–159.

Investigates the role of patrolling monocytes in endothelial regeneration following carotid injury using mice depleted of patrolling monocytes.

4. Cai W, Schaper W. Mechanisms of arteriogenesis. Acta Biochim. Biophys. Sin. (Shanghai). 2008;40:681–692.

5*. He H, Mack JJ, Güç E, et al. Perivascular macrophages limit permeability. Arterioscler. Thromb. Vasc. Biol. 2016;36:2203–2212.

Identifies that macrophages, in addition to other mural cells like pericytes, control vascular permeability.

6**. Chakarov S, Lim HY, Tan L, et al. Two distinct interstitial macrophage populations coexist across tissues in specific subtissular niches. Science. 2019;363.

Uncovers two distinct monocyte-derived tissue-resident macrophages populations across tissues. One population is localized adjacent to nerve bundles whereas the other population is a perivascular macrophage associated with blood vessels that contributes to vascular integrity.

7**. Ensan S, Li A, Besla R, et al. Self-renewing resident arterial macrophages arise from embryonic CX3CR1(+) precursors and circulating monocytes immediately after birth. Nat. Immunol. 2016;17:159–168.

Identifies the transcriptional signature of arterial "adventitia-resident" macrophages using RNA sequencing, determines their developmental origin using lineage tracing, and explores modes of replenishment of this population throughout adulthood.

8. Geissmann F, Manz MG, Jung S, et al. Development of monocytes, macrophages, and dendritic cells. Science. 2010;327:656–661.
9. Geissmann F, Jung S, Littman DR. Blood monocytes consist of two principal subsets with distinct migratory properties. Immunity. 2003;19:71–82.
10. Auffray C, Fogg D, Garfa M, et al. Monitoring of blood vessels and tissues by a population of monocytes with patrolling behavior. Science. 2007;317:666–670.
11. Auffray C, Sieweke MH, Geissmann F. Blood monocytes: development, heterogeneity, and relationship with dendritic cells. Annu. Rev. Immunol. 2009;27:669–692.
12. Yona S, Kim K-W, Wolf Y, et al. Fate mapping reveals origins and dynamics of monocytes and tissue macrophages under homeostasis. Immunity. 2013;38:79–91.
13*. Gamrekelashvili J, Giagnorio R, Jussofie J, et al. Regulation of monocyte cell fate by blood vessels mediated by Notch signalling. Nat. Commun. 2016;7:12597.
Recognizes that monocyte conversion is regulated by endothelial cells in specific vascular beds and dependent on Dll1-Notch2 signaling. Conditional deletion of Notch2 in monocytes impairs Ly6C^{lo} patrolling monocyte development.
14. Hanna RN, Carlin LM, Hubbeling HG, et al. The transcription factor NR4A1 (Nur77) controls bone marrow differentiation and the survival of Ly6C- monocytes. Nat. Immunol. 2011;12:778–785.
15**. Thomas GD, Hanna RN, Vasudevan NT, et al. Deleting an Nr4a1 Super-Enhancer Subdomain Ablates Ly6Clow Monocytes while Preserving Macrophage Gene Function. Immunity. 2016;45:975–987.
Identifies a specific enhancer at the Nr4a1locus exclusively utilized by patrolling monocytes. Taking advantage of this information, the work was able to dissect the biological impact of Nr4a1 function to patrolling monocytes. The study also shows that monocyte conversion is regulated by KLF2.
16. Carlin LM, Stamatiades EG, Auffray C, et al. Nr4a1-dependent Ly6C(low) monocytes monitor endothelial cells and orchestrate their disposal. Cell. 2013;153:362–375.
17*. Mildner A, Schönheit J, Giladi A, et al. Genomic Characterization of Murine Monocytes Reveals C/EBPβ Transcription Factor Dependence of Ly6C- Cells. Immunity. 2017;46:849–862.e7.
Highlights that transcription factor C/EBPβ regulates Nr4a1 expression, which is essential for monocyte conversion.
18**. Quintar A, McArdle S, Wolf D, et al. Endothelial protective monocyte patrolling in large arteries intensified by western diet and atherosclerosis. Circ. Res. 2017;120:1789–1799.

First to reveal that Ly6c^{lo} monocytes have unique patrolling characteristics in large arteries compared to the microvasculature. Additionally, depletion of patrolling monocytes exacerbates atherosclerosis.
19. Finsterbusch M, Hall P, Li A, et al. Patrolling monocytes promote intravascular neutrophil activation and glomerular injury in the acutely inflamed glomerulus. Proc. Natl. Acad. Sci. USA. 2016;113:E5172–81.
20. Jung S, Aliberti J, Graemmel P, et al. Analysis of fractalkine receptor CX(3)CR1 function by targeted deletion and green fluorescent protein reporter gene insertion. Mol. Cell. Biol. 2000;20:4106–4114.
21. Imhof BA, Jemelin S, Ballet R, et al. CCN1/CYR61-mediated meticulous patrolling by Ly6Clow monocytes fuels vascular inflammation. Proc. Natl. Acad. Sci. USA. 2016;113:E4847–56.
22. Cros J, Cagnard N, Woollard K, et al. Human CD14dim monocytes patrol and sense nucleic acids and viruses via TLR7 and TLR8 receptors. Immunity. 2010;33:375–386.
23. Nahrendorf M, Swirski FK, Aikawa E, et al. The healing myocardium sequentially mobilizes two monocyte subsets with divergent and complementary functions. J. Exp. Med. 2007;204:3037–3047.
24*. Olingy CE, San Emeterio CL, Ogle ME, et al. Non-classical monocytes are biased progenitors of wound healing macrophages during soft tissue injury. Sci. Rep. 2017;7:447. Reveals that Ly6C^{lo} patrolling monocytes preferentially give rise to CD206+ macrophages and examine their contributions to wound healing using a dorsal skinfold window chamber injury model.
25. Hilgendorf I, Gerhardt LMS, Tan TC, et al. Ly-6Chigh monocytes depend on Nr4a1 to balance both inflammatory and reparative phases in the infarcted myocardium. Circ. Res. 2014;114:1611–1622.
26. Karasawa K, Asano K, Moriyama S, et al. Vascular-resident CD169-positive monocytes and macrophages control neutrophil accumulation in the kidney with ischemia-reperfusion injury. J. Am. Soc. Nephrol. 2015;26:896–906.
27. Hamers AAJ, Vos M, Rassam F, et al. Bone marrow-specific deficiency of nuclear receptor Nur77 enhances atherosclerosis. Circ. Res. 2012;110:428–438.
28. Hanna RN, Shaked I, Hubbeling HG, et al. NR4A1 (Nur77) deletion polarizes macrophages toward an inflammatory phenotype and increases atherosclerosis. Circ. Res. 2012;110:416–427.

29*. Marcovecchio PM, Thomas GD, Mikulski Z, et al. Scavenger receptor CD36 directs nonclassical monocyte patrolling along the endothelium during early atherogenesis. Arterioscler. Thromb. Vasc. Biol. 2017;37:2043–2052.
Uses intravital imaging to show that patrolling is increased in non-classical monocytes upon hypercholesterolemia. Additionally, oxidized lipid uptake increases patrolling in a CD36 dependent manner.
30. Hanna RN, Cekic C, Sag D, et al. Patrolling monocytes control tumor metastasis to the lung. Science. 2015;350:985–990.
31. Mukherjee R, Kanti Barman P, Kumar Thatoi P, et al. Non-Classical monocytes display inflammatory features: Validation in Sepsis and Systemic Lupus Erythematous. Sci. Rep. 2015;5:13886.
32. Misharin AV, Cuda CM, Saber R, et al. Nonclassical Ly6C(-) monocytes drive the development of inflammatory arthritis in mice. Cell Rep. 2014;9:591–604.
33. Schaper J, König R, Franz D, Schaper W. The endothelial surface of growing coronary collateral arteries. Intimal margination and diapedesis of monocytes. A combined SEM and TEM study. Virchows Arch A Pathol Anat Histol. 1976;370:193–205.
34. Heil M, Ziegelhoeffer T, Pipp F, et al. Blood monocyte concentration is critical for enhancement of collateral artery growth. Am. J. Physiol. Heart Circ. Physiol. 2002;283:H2411–9.
35. Arras M, Ito WD, Scholz D, et al. Monocyte activation in angiogenesis and collateral growth in the rabbit hindlimb. J. Clin. Invest. 1998;101:40–50.
36. Liao L-S, Bai Y-P. The dynamics of monocytes in the process of collateralization. Aging Med (Milton). 2019;2:50–55.
37. Shireman PK. The chemokine system in arteriogenesis and hind limb ischemia. J. Vasc. Surg. 2007;45 Suppl A:A48–56.
38. Voskuil M, Hoefer IE, van Royen N, et al. Abnormal monocyte recruitment and collateral artery formation in monocyte chemoattractant protein-1 deficient mice. Vasc Med. 2004;9:287–292.
39. Voskuil M, van Royen N, Hoefer IE, et al. Modulation of collateral artery growth in a porcine hindlimb ligation model using MCP-1. Am. J. Physiol. Heart Circ. Physiol. 2003;284:H1422–8.
40*. Lin X-C, Pan M, Zhu L-P, et al. NFAT5 promotes arteriogenesis via MCP-1-dependent monocyte recruitment. J. Cell Mol. Med. 2019;

Highlights an important role of NFAT5 in collateral arteriogenesis in a rat hindlimb ischemia model. Knockdown of NFAT5 inhibits monocyte recruitment by lowering MCP-1 expression in endothelial cells, which attenuates perfusion recovery.
41. Tsou C-L, Peters W, Si Y, et al. Critical roles for CCR2 and MCP-3 in monocyte mobilization from bone marrow and recruitment to inflammatory sites. J. Clin. Invest. 2007;117:902–909.
42. Heil M, Ziegelhoeffer T, Wagner S, et al. Collateral artery growth (arteriogenesis) after experimental arterial occlusion is impaired in mice lacking CC-chemokine receptor-2. Circ. Res. 2004;94:671–677.
43. Nickerson MM, Song J, Meisner JK, Bajikar S, et al. Bone marrow-derived cell-specific chemokine (C-C motif) receptor-2 expression is required for arteriolar remodeling. Arterioscler. Thromb. Vasc. Biol. 2009;29:1794–1801.
44*. Krishnasamy K, Limbourg A, Kapanadze T, et al. Blood vessel control of macrophage maturation promotes arteriogenesis in ischemia. Nat. Commun. 2017;8:952.
Shows that monocyte-derived macrophage maturation is dependent on endothelial Dll1 expression and canonical Notch signaling during hindlimb ischemia.
45. Dodd T, Jadhav R, Wiggins L, et al. MMPs 2 and 9 are essential for coronary collateral growth and are prominently regulated by p38 MAPK. J. Mol. Cell Cardiol. 2011;51:1015–1025.
46. Morrison AR, Yarovinsky TO, Young BD, et al. Chemokine-coupled β2 integrin-induced macrophage Rac2-Myosin IIA interaction regulates VEGF-A mRNA stability and arteriogenesis. J. Exp. Med. 2014;211:1957–1968.
47*. Lim HY, Lim SY, Tan CK, et al. Hyaluronan Receptor LYVE-1-Expressing Macrophages Maintain Arterial Tone through Hyaluronan-Mediated Regulation of Smooth Muscle Cell Collagen. Immunity. 2018;49:326–341.e7.
Elucidates the physiological role of Lyve-1+ arterial "adventitia-resident" macrophages. Lyve-1+ macrophages interact directly with smooth muscle cells via Lyve1 and release MMP9 to regulate collagen production in order to regulate arterial vessel homeostasis. Depletion of Lyve-1+ macrophages results in arterial stiffness/fibrosis.
48**. Kim K, Shim D, Lee JS, et al. Transcriptome analysis reveals nonfoamy rather than foamy plaque macrophages are proinflammatory in atherosclerotic murine models. Circ. Res. 2018;123:1127–1142.
Reports the transcriptional heterogeneity of immune cells that accumulate in atherosclerotic aorta using single-cell RNA sequencing of FACS sorted CD45+ cells. Additionally, developed a lipid-based flow cytometry method coupled with bulk RNA-sequencing that revealed intimal foam macrophages expressed fewer inflammatory genes than intimal nonfoam cells.

49. Hoeffel G, Ginhoux F. Fetal monocytes and the origins of tissue-resident macrophages. Cell Immunol. 2018;330:5–15.
50. Williams JW, Giannarelli C, Rahman A, et al. Macrophage biology, classification, and phenotype in cardiovascular disease: JACC macrophage in CVD series (part 1). J. Am. Coll. Cardiol. 2018;72:2166–2180.
51. Malinauskas RA, Herrmann RA, Truskey GA. The distribution of intimal white blood cells in the normal rabbit aorta. Atherosclerosis. 1995;115:147–163.
52. Millonig G, Niederegger H, Rabl W, et al. Network of vascular-associated dendritic cells in intima of healthy young individuals. Arterioscler. Thromb. Vasc. Biol. 2001;21:503–508.
53. Choi J-H, Do Y, Cheong C, et al. Identification of antigen-presenting dendritic cells in mouse aorta and cardiac valves. J. Exp. Med. 2009;206:497–505.
54. Jongstra-Bilen J, Haidari M, Zhu S-N, et al. Low-grade chronic inflammation in regions of the normal mouse arterial intima predisposed to atherosclerosis. J. Exp. Med. 2006;203:2073–2083.
55. Liu P, Yu Y-RA, Spencer JA, et al. CX3CR1 deficiency impairs dendritic cell accumulation in arterial intima and reduces atherosclerotic burden. Arterioscler. Thromb. Vasc. Biol. 2008;28:243–250.
56. Choi J-H, Cheong C, Dandamudi DB, et al. Flt3 signaling-dependent dendritic cells protect against atherosclerosis. Immunity. 2011;35:819–831.
57. Paulson KE, Zhu S-N, Chen M, et al. Resident intimal dendritic cells accumulate lipid and contribute to the initiation of atherosclerosis. Circ. Res. 2010;106:383–390.
58. Zhu S-N, Chen M, Jongstra-Bilen J, Cybulsky MI. GM-CSF regulates intimal cell proliferation in nascent atherosclerotic lesions. J. Exp. Med. 2009;206:2141–2149.
59*. Roufaiel M, Gracey E, Siu A, et al. CCL19-CCR7-dependent reverse transendothelial migration of myeloid cells clears Chlamydia muridarum from the arterial intima. Nat. Immunol. 2016;17:1263–1272.
Uncovers the role of intimal dendritic cells during pathological processes. The authors demonstrated that intimal dendritic cells exhibit immunological functions and can undergo reverse transendothelial migration.
60**. Winkels H, Ehinger E, Vassallo M, et al. Atlas of the Immune Cell Repertoire in Mouse Atherosclerosis Defined by Single-Cell RNA-Sequencing and Mass Cytometry. Circ. Res. 2018;122:1675–1688.
Single-Cell RNA-Sequencing and Mass Cytometry. Circ. Res. 2018;122:1675–1688.

Clarifies the transcriptional and phenotypic heterogeneity of immune cells in atherosclerotic plaques using single-cell RNA sequencing and Mass Cytometry.

Chapter 2. Single cell RNA-sequencing to study vascular diversity and function

ABSTRACT

Purpose of review

Single-cell RNA sequencing (scRNA-seq) can capture the transcriptional profile of thousands of individual cells concurrently from complex tissues and with remarkable resolution. Either with the goal of seeking information about distinct cell subtypes or responses to a stimulus, the approach has provided robust information and promoted impressive advances in cardiovascular research. The goal of this review is to highlight strategies and approaches to leverage this technology and bypass potential caveats related to evaluation of the vascular cells.

Recent findings

As the most recent technological development, details associated with experimental strategies, analysis and interpretation of scRNA-seq data are still being discussed and scrutinized by investigators across the vascular field. Compilation of this information is valuable for those using the technology, but particularly important to those about to start utilizing scRNA-seq to seek transcriptome information of vascular cells.

Summary

As our field progresses to catalog transcriptomes from distinct vascular beds, it is undeniable that scRNA-seq technology is here to stay. Sharing approaches to improve the quality of cell dissociation procedures, analysis and a consensus of best practices is critical as information from this powerful experimental platform continues to emerge.

Keywords: Blood vessels, endothelial cells, smooth muscle cells, vascular heterogeneity, transcriptome

INTRODUCTION

The ability to obtain transcriptional information from individual cells has significantly expanded our understanding of the heterogeneity, repair, pathology, metabolic adaptation, and aging of blood vessels [1,2,3**,4**,5*,6*]. In contrast to bulk RNA sequencing, single-cell RNA sequencing (scRNA-seq) offers unbiased assessment of transcriptional responses to specific stimuli and clarifies pathological states at the singular cellular level with remarkable resolution. scRNA-seq has also allowed us to distinguish between minor transcriptional drifts experienced by an entire population from pronounced changes restricted to a very small subset of cells, in a manner that would be undistinguishable by bulk RNAseq. In terms of vascular development, scRNA-seq has offered unprecedented power to detect points of transition with high level of granularity, clarifying cellular trajectories and percentages of cells at distinct stages of a given differentiation process [7*,8].

In less than five years, more than 200 papers have been published containing scRNA-seq information and datasets on vascular cells. Currently, there are several atlases and databases from mice and human tissues being compiled, curated and expanded. Based on emerging transcriptional markers, we can now clearly identify endothelial cells from capillaries, arteries and veins, and pint-point features that distinguish endothelial cells from lung, brain, liver, kidney and other organs [3**]. More recently, the development of spatial transcriptomics has further expanded the capacity of the technology by mapping transcriptional information to specific coordinates within a given tissue section. It is undeniable that the power of scRNA-seq will continue to impact discoveries in cardiovascular research and expand clinical read-outs by allowing the detection of patient-specific responses to treatments and improve the characterization of side-effects.

Several excellent reviews have covered multiple aspects of scRNA-seq, ranging from workflow and technical details to major highlights achieved by this technology in the vascular field [1,2,9,10]. Here our intention is not to duplicate the information in those publications, instead to focus on specific challenges facing the profile of vascular cells. Despite its impressive reach, the use of scRNA-seq is not devoid of problems and caveats. This review presents avenues to resolve some of those issues, discusses the pros and cons of sequencing depth, and data analyses focusing on vascular cells.

CELL DISSOCIATION AND ENRICHMENT

Perhaps the most important step in scRNA-seq relates to the generation of single cell suspensions from complex tissues and organs. This is not straightforward and it becomes even more challenging when profiling organs with differential proportions of connective tissue, pathology or age. Furthermore, different vascular beds vary in resistance to dissociation protocols. Generation of tissue debris and cell death is inherent to these techniques, and these can become unwelcome incorporations to the data collected. Through experience and in reviewing published reports, three main criteria are critical in relation to scRNA-seq for blood vessels:

First, one protocol does not fit all. Each organ requires its own procedure with precise working knowledge of dissociation enzymes (or sequential combination of enzymes). Young and old organs also differ in extracellular matrix composition and level of cross-linking.

Second, cell debris, if not removed, will be unavoidably present during the generation of cDNA and the same applies to undissociated (doublet) cells. While recognition of debris and doublets can be addressed during bioinformatic analyses; their elimination during the isolation procedure is preferable, as their presence decreases sequencing depth.

Third, the length of time needed to prepare cell suspensions can alter transcription and give false read-outs. Furthermore, endothelial cells and smooth muscle cells are highly susceptible to anoikis, and thus, speed of tissue processing is critical.

In short, dissociation protocols must be optimized to generate homogeneous cell suspensions, remove debris, and be reproducible. Speed is a premium and delays can make-or-break an scRNA-seq experiment. A few detailed protocols (reproduced now by several other laboratories) have been published for specific organs [11,12]. Trying these a few times, validating viability and eliminating cell debris prior to cDNA generation is highly encouraged.

Other important considerations:

(a) Reduction of cell debris can be done by cycles of spins and washes. Low speed and short spins allow intact cells to be pelleted while debris remain in suspension. Additionally, commercial kits are available to aid in the removal of cellular debris.

(b) Reduction of doublets - use of versene (EDTA buffered solution) during the isolation procedure can significantly aid in reducing adhesion between endothelial cells, through effective chelation of calcium. Naturally, if collagenases are selected for tissue dissociation the use of EDTA will be problematic, as collagenases which are metalloproteinases, require divalent cations for their function. In this case, incorporation of versene prior to and/or after dissociation would be recommended.

(c) Speed in tissue dissociation can be improved by mechanical fragmentation (preferentially with scalpel instead of scissors to minimize damage).

No matter how careful, every tissue-dissociation protocol results in some degree of cells being ruptured, releasing of their mRNAs into the media. This cell-free RNA or also termed “ambient RNA” can be reduced through washes. In the case of endothelial cells, however, nucleic acids can tightly bind to the positively charged glycocalyx and through this process ambient mRNA get carried with intact endothelial cells into the process of cDNA isolation, regardless of the number of washes. To eliminate ambient RNA, cell lysates can be exposed to

RNAseA prior to cDNA generation. Even a very short exposure to RNAseA (3-5min) can remove the majority of ambient RNA. It is critical, however, that cells are washed in a buffer containing RNAseA inhibitor to effectively remove the enzyme prior to initiating the procedures for generation of libraries. We found significant improvement in the final read-outs when an RNAseA step is incorporated.

Our lab has extensive experience with isolation of cells for the murine aorta in a manner that is highly reproducible and can be optimized for the enrichment of endothelial cells and / or smooth muscle cells [5*,13] (**Figure 2.1**). In the case of enrichment for endothelial cells, we find that digestion of the entire vessel is not efficient, instead exposure of the tunica intima and direct trypsinization is the best way to obtain large numbers of intact cells in a timely manner. Specifically, our protocol includes initial perfusion with versene and removal of the aorta, followed by dissection of the adventitia under the dissecting microscope. The aorta is then cut open along its length with small scissors and pinned on a silicone-covered plate as a sheet having the endothelium facing up. Subsequently, open vessels are exposed to 1X trypsin for 5min at 37^{o}C and finally scrapped with a thin scalpel. The cell suspension is then placed on a tube containing tissue culture media with 5% fetal calf serum to inactivate the trypsin. Cells are then spun and washed with PBS containing BSA, exposed to RNAseA for 5min to remove RNAs bound to endothelial surface, spun and washed with two cycles of low speed short duration centrifugations. Endothelial cells are then counted and evaluated for viability. This initial quality control is the first “go or no-go” step. Preparations with more than 30% death cells should be aborted at this stage. Using this protocol, we have reproducibly achieved 97% cell viability. This type of procedure provides a significant enrichment for endothelial cells. Smaller amounts of cells from the adventitia (fibroblasts and inflammatory cells) are also routinely collected using this procedure, as well as a small fraction of smooth muscle cells.

When evaluation of smooth muscle cells from the aorta is desired, we find that digestion with liberase (Sigma-Aldrich), provides the very best yields when compared to collagenase or

sequential collagenase/trypsin. After perfusion with versene and removal of the fatty adventitia, we mince the aorta into small fragments with spatula blades while the tissue remains submerged in versine solution and proceed to transfer the fragments into a freshly prepared liberase solution (2.5% Liberase TH from frozen stock , 0.01U DNase1, in 1X HBSS). The strategy is similar to the protocol described by Wirka et al. with some modifications [14**]. Vessel fragments are rotated in liberase solution for 30min pipetting up and down every 5-10min to aid dissociation. After desired digestion is achieved, an equal volume of tissue culture media with 10% FCS is added and the entire suspension is filtered through a 20uM cell strainer. The filtered suspension is spun at 1000rpm for 2min and resuspended in 0.4% BSA-PBS, counted and evaluated for viability. As with endothelial cells, we only proceed for cDNA prep if at least 70% of cells are viable.

Depletion of red blood cells (RBCs) post-cell dissociation is not technically necessary but it is very helpful to improve representation of cells from the vessel wall. When present in high numbers RBCs add to the total number of “cells”, reducing the depth of sequencing and offering no information to answer questions related to endothelial, smooth muscle, or pericyte biology. Removal of RBCs with an RBC lysis buffer after the cell dissociation is advised.

Enrichment of endothelial and smooth muscle cells from large vessels is far easier to achieve than enrichment of these cells from smaller vessels where dissection is impractical. For this, whole tissue digestion is often followed by flow cytometry and sorting (FACS) or other enrichment step. While FACS has the welcoming benefit of removing debris and dead cells generated during initial tissue dissociation; the high pressure of sorting cells can induce artificial stress, affect expression profiles [15] and/or promote cell death post-sorting. Furthermore, endothelial cells and smooth muscle cells are highly sensitive to remaining in cell suspension for long periods of time aggravating anoikis and further contributing to debris. Because of these caveats, comparisons between sorted and non-sorted preparations, albeit at lower depth, is advised to understand potential problems with the chosen isolation procedure. In some cases,

unsorted tissue suspensions can provide a path to improved rigor and reproducibility of the data and still provide sufficient depth for discovery. In some cases, investigators have included actinomycin D in the isolation buffers to prevent de-novo transcription post-isolation. Importantly, validation of differential expression is required to ensure that isolation methods themselves have not artificially imposed alterations on the transcriptomes under study.

CELL NUMBER VERSUS DEPTH WHEN GENERATING cDNA LIBRARIES

When generating scRNA-seq libraries, it is important to prioritize the goal of the study in order to determine how many cells to sequence and to what depth of coverage (reads per cell). Single-cell sequencing depth is determined by the number of transcripts detected from each cell. Many factors contribute to the depth, including how many cells, or pooled libraries, are being sequenced per lane and the sequencing power of the instrument being used (i.e. NovaSeq6000 vs HiSeq4000, etc.). In practice, most experiments analyze fewer than 10,000 cells and have coverage which would allow analysis of 2,000 to 4,000 transcripts. Naturally multiple independent experiments can be combined to increase power. However, raising cell number in one experiment, introduces a practical limitation in the total number of reads that can be sequenced per cell and thus, decreasing the overall depth (reads per cell). If the goal of the study is to identify a rare cell population or to scan cells for mixed populations, then opting for more cells but lower read depth is practical and economical [16]. However, lower read depth will not necessarily provide detailed information on gene expression within any given single cell and makes it difficult to distinguish technical dropout of transcripts from true biological variation between cells [17]. Conversely, if the main goal of the study is to characterize the transcriptome of a particular cell with the greatest possible resolution or to carry out a more detailed examination of gene-to-gene expression, then high read depth is required. In our experience, obtaining valuable information about discrete transcriptional changes requires high representation of the cell type of interest and relatively lower number of cells. This strategy

increases depth of sequencing per cell (reads per cell) and improves ability to identify transcriptional alterations between two groups.

Depth of transcriptional read-out is also affected by how many libraries are sequenced per lane. We find that sequencing two libraries containing ~5000 cells per library on one lane of HiSeq4000 after the EC- or SMC enrichment procedure described above and using the 10X Genomics platform provides excellent outcomes towards identifying transcriptional changes to an insult, state, or genetic perturbation. Additionally, we have used the NovaSeq6000, which allows sequencing more cells and more libraries in one lane while still reaching sequencing saturation and obtaining outstanding depth; albeit, this platform is a more expensive option.

QUALITY CONTROL

There are many levels of quality control (QC) when dealing with scRNA-seq (**Figure 2.2**). Before committing to library generation, it is important to ensure that the cell isolation method being used is in fact enriching for the desired cell population. As discussed previously, isolating vascular cells can be a difficult task and it is standard to retrieve many RBCs and other contaminating cells from the blood if regular steps are not carefully incorporated into the protocol and study design. Assessing the quality of the cell isolation and the degree of enrichment for the cells of interest, either by flow cytometry or other methods (e.g., microscopy) is critical prior to library construction. Note, isolated cells should not remain in suspension while type of quality control is being determined. Both 10X Genomics protocols and fluidic procedures have pause points that enable a go vs no-go decision step. Additionally, high cell viability is essential for reliable and optimal results, as dead or apoptotic cells will release ambient RNA, which increases the background noise and compromises data quality. Furthermore, low cell viability reduces or changes transcriptional output as cells may be under stress. Most platforms recommend a minimum of 70% cell viability. Before sequencing, the final library should also be evaluated using either a Bioanalyzer High Sensitivity chip or a TapeStation High Sensitivity

Screen Tape for library quality control and qualitative analysis. Depending on the platform and expected cell types, the overall traces and shape of the electropherogram will vary. Most User Guides will describe the desired size of the library fragments. The peak profile is highly informative on the quality of the library, as if too small or too big can affect the sequencing results. Additional layers of post-sequencing QC, ranging from data filtration, quality metrics, doublets and ambient RNA exclusion will be discussed below.

BIOINFORMATICS

An scRNA-seq library on human or mouse samples typically yields thousands of cells with around 20,000 genes detected in total. These experiments generate much larger volumes of data than bulk RNA-seq. Thus, fast and efficient bioinformatics methods are essential for scRNA-seq analysis. While multiple tools exist for scRNA-seq analysis, there are several core steps implemented in most of these tools [18]. These common steps include quality control, normalization, dimensionality reduction, clustering, cell type annotation and differential expression analysis.

In the quality control step, cells are generally filtered by the number of genes, the number of unique molecular identifiers (UMIs) and the percentage of mitochondrial genes expressed. When comparing multiple samples that were generated from distinct libraries, it is critical to correct for potential batch effects among the samples [19*]. Typically, batch effects can be identified in the clustering and cell type annotation step. When endothelial cells and smooth muscle cells from different samples segregate into totally distinct clusters, it is likely that batch effects are present in the data-set, as it is unlikely that any type of treatment will impact transcriptome in such a drastic manner. Unless, one can see that other cell types from the two distinct datasets overlap and only one population segregates. If this is the case, it is likely that the separation is caused by real biological alterations.

One of the common factors leading to batch effect is ambient RNA contamination, where cell-free RNA was captured and assigned to a cell during library construction. For example, hemoglobin genes from the red blood cells and immunoglobulin genes from the plasma cells can diffuse, resulting in detection in every cell in the library. Two algorithms, EmptyDrops [20] and SoupX [21**], were developed to eliminate the contamination. These tools first detect empty droplets (or wells) in the library, and evaluate the transcript abundance in these empty droplets. The transcripts highly detected in the empty droplets are considered ambient RNA contamination, whose expressions are then subtracted from all the cells.

Another common problem during library construction are doublets, where two cells are captured by the same droplet. These can also be identified and removed using data analysis. Specifically DoubletFinder [22] predicts doublets by using the cells expression pattern, and comparing it to the average expression of randomly chosen cell pairs. After quality control, the expression values are normalized by the total expression of each cell and log-transformed. Data are then scaled for individual genes.

In order to visualize the cells in two dimensional plots and preserve the structure of the dataset, principal component analysis (PCA) and uniform manifold approximation and projection (UMAP) [23] are usually applied to reduce the dimensionality. Graph-based clustering [24] and K-nearest neighbors are applied to group the cells with similar expression patterns into distinct clusters. Each cluster is compared to all the other clusters to find the cluster marker genes, and canonical cell lineage genes are overlapped with the cluster marker genes to annotate the cell types [25*]. PECAM1 and CDH5 serve as good markers to identify endothelial cells in any dataset. We find that even when dividing, endothelial cells never lose expression of these two markers. For the endothelial subtypes, SOX17, GJA4 and GJA5 are used to identify arterial endothelial cells. NR2F2, NPR2 and APLNR are used to identify venous endothelial cells. MEST, PLVAP, CTLA2A are used to identify capillary endothelial cells. MMRN1 and LYVE1 are used to identify lymphatic endothelial cells. ACTA2, TAGLN and MYH11 serve as good markers

for vascular smooth muscle cells. After cell type annotation, differential expression analysis can be carried out between cell types or between distinct states / experimental treatment for the same cell type.

ANALYSES AND INTERPRETATION OF DATA

Post-analyses, scRNA-seq datasets provide a wealth of information that must be understood and carefully interpreted. More frequently than not, small variations in multiple genes and pathways, rather than with large alterations in few genes are noted. How to determine what is important?

While scRNA-seq is a very powerful technique, in most cases it is the beginning rather than the end of an experimental journey. Validation of affected transcripts is critical and specific experiments to address hypotheses raised by the data are essential. Previous knowledge of the physiology, pathology, and / or the system being interrogated is key to distilling the information obtained from scRNA-seq. Frequently, the use of Gene Ontology (GO) (http://geneontology.org) platforms are applied to the dataset. The ease of these platforms makes GO a frequent destination in the midst of data-analysis, but one that can be frustrating. Gene Ontology covers three major domains: Cellular Components, Molecular Function and Biological Process. If used, running the data with all three, instead of only one is important. This being said, it is critical to understand that these engines use publications to annotate and generate categories. As consequence, an enrichment in TGFbeta and BMP induced transcripts might read as “bone development” even though there are no bone-related cells in the dataset. Thus, how useful are GOs? GOs can guide experimental efforts, as they provide global information of genetic changes, but in isolation (absence of other experiments or interpretation) GOs might not be all that useful. Perhaps as publications expand and GOs get further annotated, the veracity of a given GO might improve with increased utility.

A platform that can be useful as a first go is String. Like GO, String also relies on published information. But as a first go, it offers names and functions of genes as a list, and potential interactions as per publications (https://string-db.org/cgi/input?sessionId=bQaxu93uR7yX&input_page_show_search=on).

Another tool used for scRNA-seq data interpretation is pseudo-temporal trajectory. This option is particularly valuable if the cells being examined undergo a dynamic process such as differentiation, proliferation or migration. Furthermore, this technology is extremely useful when differentiation of cells from progenitors is a key question to be answered from the dataset. For example, identification of genes that are associated with the differentiation of hematopoietic stem cells from endothelial cells (hemogenic endothelium) [7*]. Pseudo-temporal analysis aligns and orders the cells based on the progression through a process experienced by the cells in relation to global transcriptome information. Compared to clustering analysis, instead of grouping the cells into discrete clusters, trajectory inference arranges the cells in a continuum, which better characterizes the dynamic process undergone by the cell. Differential expression in pseudo-temporal analysis reveals the expression pattern of genes along the pseudo-time linearly, enabling the investigation of the expression fluctuation compared to a single number showing the fold change. To date, more than 70 trajectory inference methods have been developed. A recent benchmark study [26] investigated the accuracy, scalability, stability and usability of these methods, and suggested that PAGA [27], Slingshot [28] and Monocle [29] as the most favored methods for the pseudo-temporal analysis. In addition to pseudo-temporal analyses based on the gene expression levels, trajectory can also be constructed using the RNA velocity in single cells [30]. RNA velocity measures the ratio of spliced and unspliced transcripts, which can be used to predict the future state of the cells on a time scale of hours. The tool, scVelo [31**], built for RNA velocity analysis solves the splicing kinetics, and provides unsupervised results disclosing the transition from the starting cells to the ending cells.

VALIDATION OF THE DATA

As all techniques and models, scRNA-seq can incorporate caveats in datasets and the usefulness of the data obtained is only as good as its accuracy. Validation of the information obtained through an independent experimental strategy is an essential step in the trajectory of data interpretation and generation of conclusions from any scRNA-seq experiment. It can be, however, daunting (and expensive) to undertake validation of scRNA-seq datasets. While multiple experimental approaches can be used, two in particular, are favored by most investigators: in situ hybridization (now using RNA-SCOPE) and immunocytochemistry. The second having the added value of querying whether the protein parallels transcriptomic read-outs. Problems with immunocytochemical approaches: availability of antibodies, validation of antibodies (using tissues from KO mice or CRISPRcells), specie-recognition of available antibodies, ability of antibodies to work on immunocytochemistry on tissue sections (also frozen or fixed), and ability to detect and quantify changes. Clearly the process is not trivial, and in our experience, we tend to find that only 1 out of 5 antibodies actually works as advertised. Sharing this information with colleagues can be a big help, particularly within a community. If not, verifying that antibodies have been used in publications with the same species and techniques is also important.

The next question is how many independent validations is sufficient to trust the dataset. Here, the specific context of the initial question and the conclusions stated from the scRNA-seq data are important. This being said, a good rule of thumb is three independent targets. It is also valuable to keep in mind that not always RNA and protein go hand-and-hand.

SPATIAL INFORMATION AND MULTIOMES

While scRNA-seq provides unprecedented opportunities to study the heterogeneity of transcriptomics within a tissue, the spatial locations of the cells is lost by the need to dissociate the tissue to obtain single-cell suspensions. Recent advances in spatial sequencing (spatial-

seq) tackle this issue by extracting and barcoding the RNAs directly from the tissue [32]. In scRNA-seq, the barcodes are used to assign the transcripts to individual cells, similarly, the barcodes in spatial-seq are used to trace the extraction location of transcripts. Spatial-seq reveals the relative distance between cell types, thus facilitates the cell-cell interaction under the assumption that adjacent cells are more likely to interact [33*]. One drawback of spatial-seq is lower resolution compared to scRNA-seq, as each capturing area may contain multiple cells of different cell types. Thus, deconvolution needs to be applied in silico to characterize the composition of the cell types. This problem will be solved in the future as technologies keep evolving until single cell resolution is achieved.

Besides single cell or spatial transcriptomics, other technologies that profile chromatin accessibility [34], DNA methylation [35] and protein [36] were developed at the individual cell level, allowing the analyses of single cell multiomics. Recently, 10X Genomics introduced a single cell multiome platform that unifies the transcriptome and epigenome by applying scRNA-seq and scATAC-seq in the same cell. CITE-seq [36] uses oligonucleotide-labeled antibodies to measure the abundance of the protein level, in which the oligonucleotides can be sequenced similarly as the scRNA-seq barcodes, hence characterizing the transcriptome and the designated proteins in the same cell at the same time. Integrative analysis of multiomics data ensures more accurate regulatory relationships among the different omics layers, and will likely become standard for biological interpretation.

CONCLUSIONS

In the last five years, scRNA-seq technology has become an important platform from which to obtain valuable information related to pathological states, treatments, and genetic perturbations. In addition, the technology has expanded our understanding of vascular diversity and heterogeneity in relation to organ specificity and it has clarified developmental trajectories of endothelial and smooth muscle cells. Because of its applicability and reach, scRNA-seq has

also become almost an expectation from reviewers. Needless to say, the power of the technology is undeniable. However, there are a number of important considerations and caveats that can impinge on the interpretation of the data. We have touched on some of these based on our own experience, discussion with colleagues, and through evaluating the literature. We hope that this information is of value to those starting to embrace this technology. As key questions are addressed, the field will ultimately generate complete mouse and human cell atlases which will be extremely useful for future research. Additional needs will push the limits of the technology to incorporate other omics into 3-dimensional tissue maps. In the short term, retrieval of transcriptome data from frozen human samples is progressing. Protocols for optimizing nuclei isolation from frozen specimens have gained momentum and reproducibility allowing for generation for reliable scRNA-seq data. This development can significantly broaden the reach of the technique and its applicability to retrospective human tissues.

As we continue to expand our understanding of the transcriptome, it is critical to recognize that we have currently become very “transcriptome-centric”. The future will likely expand single cell techniques to encompass cellular compartments, dynamic oscillations and post-translational modifications (*the post-omics?*) in biological processes.

ACKNOWLEDGEMENT

Figures generated with BioRender.

FINANCIAL SUPPORT AND SPONSORSHIP

This work was supported from a grant from the National Institutes of Health (R35HL140014). FM is supported by the US Department of Energy Office of Science under Award DE-FC02-02ER63421. MR is supported by the National Institutes of Health Ruth L. Kirschstein National Research Service Award (5T32HL134633-4) and GEH is supported by Howard Hughes Medical Institute Gilliam Fellowship (GT11560).

CONFLICTS OF INTEREST

There are no conflicts of interests.

FIGURES

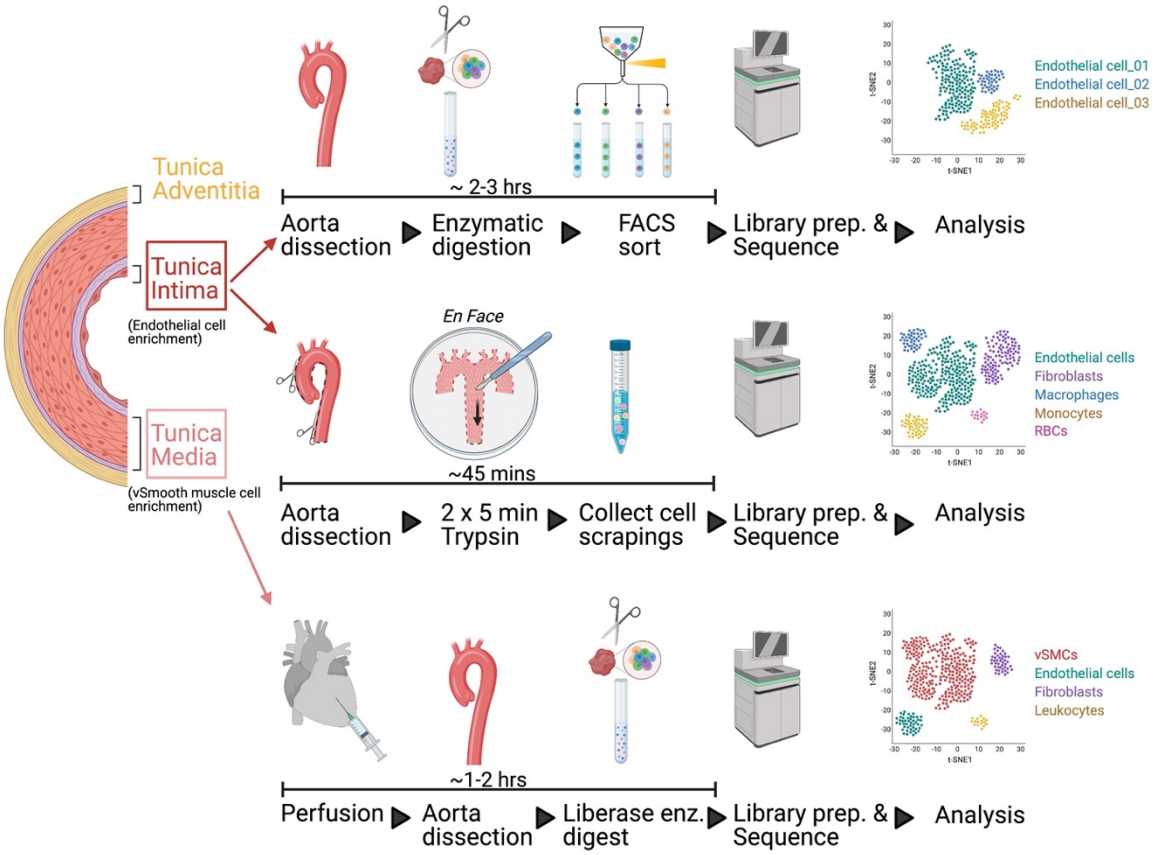

Figure 2.1. Cell dissociation and single-cell preparation of vascular cells.

A,B) Two isolation methods used to capture and enrich for the cells in the tunica intima. **A)** The aortae are dissected and enzymatically digested, followed by cell sorting based on subjective markers. The sorted cells are then used to generate libraries. **B)** The aortae are dissected and cut through the dorsal portion of the segmented wall opening the tubular structure as a flat plan (*en face)*. The aortae are then pinned to a silicone dish with the tunica intima facing up and washed with versene and incubated with trypsin for 5 minutes. After trypsin, the tunica intima is gently scraped using a feather scalpel and the cells are collected and used for library

generation. **C)** Isolation method used to enrich vascular smooth muscle cells (vSMCs). Mice are injected with heparin, perfused with versene, and then aortae are dissected and digested using a liberase enzyme cocktail. Single-cell suspension is then used to generate libraries. tSNE plots are representative of the cell types captured using each method.

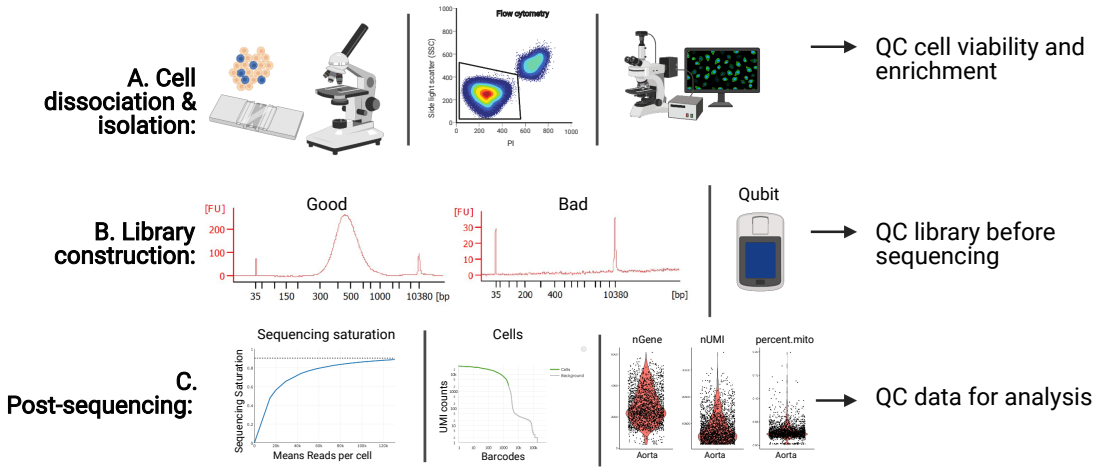

Figure 2.2. Quality control measurements executed during scRNA-seq

A) Prior to library generation, quality control (QC) measurements of cell viability and enrichment (i.e. using hemocytometers, flow cytometry, microscopy etc.) are critical for downstream single-cell quality. **B)** Post-library construction QC using a High sensitivity TapeStation or a Bioanalyzer, as well as measuring library concentration with Qubit, will shed light on the quality of the library prior to paying for sequencing. **C)** Quality assessment of scRNA-seq data is essential before downstream analysis. Assessing the sequencing saturation, the number of cells, genes, and mitochondrial genes detected, are a few QC post-sequencing metrics used.

REFERENCES

Papers of particular interest, published within the annual period of review, have been highlighted as:

* of special interest

** of outstanding interest

1. Paik DT, Cho S, Tian L, et al. Single-cell RNA sequencing in cardiovascular development, disease and medicine. *Nat. Rev. Cardiol.* 2020, 17:457–473.

2. Jakab M, Augustin HG: Understanding angiodiversity: insights from single cell biology. *Development* 2020, 147.

3. **Kalucka J, de Rooij LPMH, Goveia J, et al. Single-Cell Transcriptome Atlas of Murine Endothelial Cells. *Cell* 2020, 180:764–779.e20.
This study provides a single-cell endothelial cell atlas of healthy, murine tissues.

4. **Paik DT, Tian L, Williams IM, et al. Single-Cell RNA Sequencing Unveils Unique Transcriptomic Signatures of Organ-Specific Endothelial Cells. *Circulation* 2020, 142:1848–1862.
This study identified transcriptional networks, sex differences, and angiocrine signaling pathways in endothelial cells from various mouse tissues.

5. *McDonald AI, Shirali AS, Aragón R, et al. Endothelial Regeneration of Large Vessels Is a Biphasic Process Driven by Local Cells with Distinct Proliferative Capacities. *Cell Stem Cell* 2018, 23:210–225.e6.
This study shows that endothelial cell regeneration in aorta is driven by distinct populations arising from differentiated endothelial cells.

6. *Dumas SJ, Meta E, Borri M, et al. Single-Cell RNA Sequencing Reveals Renal Endothelium Heterogeneity and Metabolic Adaptation to Water Deprivation. *J. Am. Soc. Nephrol.* 2020, 31:118–138.
This study provides a high-resolution atlas of the renal endothelium as well as identifies a new role of oxidative phosphorylation in the metabolic adaptation of medullary renal endothelial cells to water deprivation.

7. *Zeng Y, He J, Bai Z, et al. Tracing the first hematopoietic stem cell generation in human embryo by single-cell RNA sequencing. *Cell Res.* 2019, 29:881–894.
This study constructed the first genome-scale gene expression landscape covering the entire course of endothelial-to-Hematopoietic transition during human embryogenesis using scRNA-seq.

8. Sharma B, Chang A, Red-Horse K. Coronary artery development: progenitor cells and differentiation pathways. *Annu. Rev. Physiol.* 2017, 79:1–19.

9. Iqbal F, Lupieri A, Aikawa M, Aikawa E. Harnessing Single-Cell RNA Sequencing to Better Understand How Diseased Cells Behave the Way They Do in Cardiovascular Disease. *Arterioscler. Thromb. Vasc. Biol.* 2020, doi:10.1161/ATVBAHA.120.314776.

10. Chavkin NW, Hirschi KK. Single cell analysis in vascular biology. *Front. Cardiovasc. Med.* 2020, 7:42.

11. Vanlandewijck M, He L, Mäe MA, et al. A molecular atlas of cell types and zonation in the brain vasculature. *Nature* 2018, 554:475–480.

12. Su T, Stanley G, Sinha R, et al. Single-cell analysis of early progenitor cells that build coronary arteries. *Nature* 2018, 559:356–362.

13. Hilfenhaus G, Nguyen DP, Freshman J, et al. Vav3-induced cytoskeletal dynamics contribute to heterotypic properties of endothelial barriers. *J. Cell Biol.* 2018, 217:2813–2830.

14. **Wirka RC, Wagh D, Paik DT, et al. Atheroprotective roles of smooth muscle cell phenotypic modulation and the TCF21 disease gene as revealed by single-cell analysis. *Nat. Med.* 2019, 25:1280–1289.
This study comprehensively characterized the transcriptomic phenotype of smooth muscle cells in both human and murine atherosclerotic lesions using scRNA-seq.

15. van den Brink SC, Sage F, Vértesy Á, et al. Single-cell sequencing reveals dissociation-induced gene expression in tissue subpopulations. *Nat. Methods* 2017, 14:935–936.

16. Pollen AA, Nowakowski TJ, Shuga J, et al. Low-coverage single-cell mRNA sequencing reveals cellular heterogeneity and activated signaling pathways in developing cerebral cortex. *Nat. Biotechnol.* 2014, 32:1053–1058.

17. Grün D, van Oudenaarden A. Design and Analysis of Single-Cell Sequencing Experiments. *Cell* 2015, 163:799–810.

18. Tian L, Dong X, Freytag S, et al. Benchmarking single cell RNA-sequencing analysis pipelines using mixture control experiments. *Nat. Methods* 2019, 16:479–487.

19. *Korsunsky I, Millard N, Fan J, et al. Fast, sensitive and accurate integration of single-cell data with Harmony. *Nat. Methods* 2019, 16:1289–1296.
This study introduces an useful method for batch effect removal in scRNA-seq analysis. This method is efficient and accurate, and is widely used.

20. Lun ATL, Riesenfeld S, Andrews T, et al. EmptyDrops: distinguishing cells from empty droplets in droplet-based single-cell RNA sequencing data. *Genome Biol.* 2019, 20:63.

21. **Young MD, Behjati S. SoupX removes ambient RNA contamination from droplet-based single-cell RNA sequencing data. *Gigascience* 2020, 9.
This study introduces an useful method for ambient RNA removal in scRNA-seq analysis, which is widely used in droplet based scRNA-seq studies.

22. McGinnis CS, Murrow LM, Gartner ZJ. DoubletFinder: Doublet Detection in Single-Cell RNA Sequencing Data Using Artificial Nearest Neighbors. *Cell Syst.* 2019, 8:329–337.e4.

23. Becht E, McInnes L, Healy J, et al. Dimensionality reduction for visualizing single-cell data using UMAP. *Nat. Biotechnol.* 2018, 37:38–44.

24. Xu C, Su Z. Identification of cell types from single-cell transcriptomes using a novel clustering method. *Bioinformatics* 2015, 31:1974–1980.

25. *Ma F, Pellegrini M. ACTINN: automated identification of cell types in single cell RNA sequencing. *Bioinformatics* 2020, 36:533–538.
This study introduces a supervised method to annotate cell types in scRNA-seq analysis. It is fast and efficient, and requires no marker genes but identifies cell types automatically.

26. Saelens W, Cannoodt R, Todorov H, Saeys . A comparison of single-cell trajectory inference methods. *Nat. Biotechnol.* 2019, 37:547–554.

27. Wolf FA, Hamey FK, Plass M, et al. PAGA: graph abstraction reconciles clustering with trajectory inference through a topology preserving map of single cells. *Genome Biol.* 2019, 20:59.

28. Street K, Risso D, Fletcher RB, et al. Slingshot: cell lineage and pseudotime inference for single-cell transcriptomics. *BMC Genomics* 2018, 19:477.

29. Trapnell C, Cacchiarelli D, Grimsby J, et al. The dynamics and regulators of cell fate decisions are revealed by pseudotemporal ordering of single cells. *Nat. Biotechnol.* 2014, 32:381–386.

30. La Manno G, Soldatov R, Zeisel A, et al. RNA velocity of single cells. *Nature* 2018, 560:494–498.

31. **Bergen V, Lange M, Peidli S, et al. Generalizing RNA velocity to transient cell states through dynamical modeling. *Nat. Biotechnol.* 2020, 38:1408–1414.
This study generalizes RNA velocity analysis for scRNA-seq datasets. It provides a convenient method that makes RNA velocity analysis straightforward for the users

32. Rodriques SG, Stickels RR, Goeva A, et al. Slide-seq: A scalable technology for measuring genome-wide expression at high spatial resolution. *Science* 2019, 363:1463–1467.

33. *Ma F, Hughes TK, Teles RMB, et al. Single cell and spatial transcriptomics defines the cellular architecture of the antimicrobial response network in human leprosy granulomas. *BioRxiv* 2020, doi:10.1101/2020.12.01.406819.
This study uses spatial-seq to characterize granulomas in human leprosy skin, which provides new methodology on spatial-seq analysis and interpretation.

34. Chen H, Lareau C, Andreani T, Vinyard ME, et al. Assessment of computational methods for the analysis of single-cell ATAC-seq data. *Genome Biol.* 2019, 20:241.

35. Karemaker ID, Vermeulen M. Single-Cell DNA Methylation Profiling: Technologies and Biological Applications. *Trends Biotechnol.* 2018, 36:952–965.

36. Stoeckius M, Hafemeister C, Stephenson W, et al. Simultaneous epitope and transcriptome measurement in single cells. *Nat. Methods* 2017, 14:865–868.

Chapter 3. Transcriptional evaluation of the ductus arteriosus at the single-cell level uncovers a requirement for vimentin for complete closure

ABSTRACT

Objective:

Failure to close the ductus arteriosus immediately post-birth, patent ductus arteriosus (PDA), accounts for up to 10% of all congenital heart defects. Despite significant advances in PDA management options, including pharmacological treatment targeting the prostaglandin pathway, a proportion of patients fail to respond and must undergo surgical intervention. Thus, further refinement of the cellular and molecular mechanisms that govern vascular remodeling of this vessel is required.

Approach and results:

As anticipated, single-cell RNA sequencing on the ductus arteriosus in mouse embryos at E18.5, P0.5, and P5, revealed broad transcriptional alterations in the endothelial, smooth muscle, and fibroblast cell compartments. Making use of these data sets, vimentin emerged as an interesting candidate for further investigation. Subsequent studies demonstrated that, in fact, mice with genetic deletion of vimentin fail to complete vascular remodeling of the ductus arteriosus, as per presence of a functional lumen.

Conclusions: Through single-cell RNA-sequencing and by tracking closure of the ductus arteriosus postnatally in mice, we uncovered the unexpected contribution of vimentin in driving complete closure of the ductus arteriosus potentially through regulation of the Notch signaling pathway.

INTRODUCTION

During fetal life, the ductus arteriosus, or ductus Botalli, is the vessel that connects the left pulmonary artery to the descending aorta. This structure is critical during fetal development as it diverts the blood emanating from the right ventricle away from the high-resistance pulmonary circulation and into the systemic circulation. At birth a combination of physical and biochemical changes including: the inflation of the lungs, the resulting changes in hemodynamics and alterations in prostaglandin levels trigger the closure of the ductus arteriosus. This essential physiological event prevents the mixture of non-oxygenated blood (from the pulmonary artery) with oxygenated blood (from the aorta).

Abnormal persistence of this vessel, a condition termed patent ductus arteriosus (PDA), frequently occurs in pre-term infants and it is associated with subsequent mortality (1–3). Clinical management of PDA ranges from surgical ligation to pharmacotherapy with cyclooxygenase inhibitors (1–3). Unfortunately, a percentage of patients with PDA fail to respond to these inhibitors. Consequently, a more refined understanding of the processes involved in closure of the ductus arteriosus could offer novel targets for intervention and improved therapies.

At the cellular level, the postnatal closure of the ductus arteriosus is thought to involve the contribution of smooth muscle cells, endothelial cells, and fibroblasts leading to the eventual transformation of this embryonic vessel into a ligament (1–3). Initially, a rapid and robust constriction of smooth muscle cells restricts blood flow. Subsequently, changes in endothelial and smooth muscle cells promote complete closure of the lumen, a process that in humans takes one to three weeks. While much it is known about the initial stage, less is understood about the molecular drivers associated with the later steps. Physiologically, it is understood that the initial constriction of the ductus arteriosus relies on increased arterial pO2, decreased blood pressure in the DA lumen, reduction in circulating prostaglandin E2 (PGE2) and PGE2 receptor levels. These events trigger rapid smooth muscle cell contraction through changes in intracellular calcium levels and a drastic reduction in PGE2 signaling upon dissociation of the placenta which

is the main source of PGE2. Nonetheless, complete closure of the lumen requires the participation of the endothelium through relatively unknown mechanisms.

Here we sought to characterize the transcriptional changes involved in the closure of the ductus arteriosus by performing single cell RNAseq prior to, during and shortly after closure using the mouse as a model system. Our second goal was to identify novel regulators of developmentally programmed vascular remodeling.

RESULTS

Changes in Vimentin expression during the closure of the ductus arteriosus

Single-cell RNAseq (scRNA-seq) transcriptomics on the ductus arteriosus (DA) and aorta were conducted at developmental stages prior to constriction, at peak constriction, and at post-vessel occlusion (E18.5, P0.5, and P5; **Figure 1A; Supplementary Figure1A, B**). Each DA were carefully dissected and enzymatically digested to generate 3 independent scRNA-seq libraries, without FACS-sorting (**Figure 1A**). Using dimensionality reduction by uniform manifold approximation and projection (UMAP), we identified 5 distinct cell types and assigned cellular identities based on canonical lineage markers (endothelial cells, vascular smooth muscle cells, fibroblasts, sympathetic nerve cells, and leukocytes) (**Figure 1B-D, Supplementary Figure 1C**).

Evaluation of the top 10 genes expressed at all time points, revealed two long non-coding RNAs (*Malat1* and *Tpt1*); four extracellular matrix transcripts (*Sparc, Col1a2, Eln, and Mgp*) and three cytoskeletal proteins (*Vim, Tmsb4x and Actb*) (**Figure 1D**). The 10th gene, not surprisingly, was eukaryotic translation elongation factor 1 alpha (*Eef1a1*) involved in modulation of cytoskeleton, and that also exhibits chaperone-like activity, controls proliferation and cell death. Interestingly, these three transcripts exhibit a time-specific pattern of upregulation being prior to, during, or after constriction. Our particular interest when analyzing the data was to identify transcripts that sharply increased at P0.5, the time of DA closure and that returned to steady-state or lower by P5, a

profile clearly followed by the intermediate filament Vimentin (*Vim*). Importantly, vimentin was highly expressed by vascular smooth muscle cells (vSMCs), fibroblasts, and endothelial cells (EC) (**Figure 1E**). Furthermore, its expression pattern fulfilled our criteria by exhibiting a bell-shaped curve with a peak at P0.5, particularly in vSMC and ECs a time of active DA remodeling. Closer evaluation of the top 30 genes in DA from EC (**Figure 1F**) and vSMC (**Figure 1G**) reveals in closer detail the peak of expression in relation to other highly abundant transcripts. The scRNAseq dataset presented was further mined to answer questions related to specific processes and transcripts during the closure of the ductus arteriosus.

The potential contribution of vimentin in the closure of the ductus arteriosus has not been previously explored. It is pertinent as intermediate filaments are well known to provide mechanical strain and resilience (4). Interestingly, vimentin's expression was unique amongst other intermediate filaments in the ductus arteriosus. Other members of the family, such as desmin and keratins were also expressed, but at lower levels and with patterns restricted to specific cell types; desmin in smooch muscle and keratins in endothelial cells (**Figure 1H**). Furthermore, neither desmin nor keratins showed an expression pattern that peaked at P0.5 and decrease thereafter.

To clarify whether the increased expression of *Vim* at P0.5 was specific to the DA instead of a general developmental pattern that extended to other vessels, we took advantage of scRNA-seq generated from aorta of the same mice (minus ducti) (**Figure 1I**). Expression levels of *Vim* in the aortae were then used to normalize *Vim* transcripts of the DA to further assess levels per cell type and independent of global developmental patterns. These findings further confirmed sharp increases at P0.5 specifically in ducti endothelial cells, smooth muscle cells, and fibroblasts indicating that across these cell types, *Vim* expression increases during the constriction of the DA at P0.5 (**Figure 1J**).

To directly test the potential contribution of vimentin in the closure of the DA, we took advantage of an established vimentin knock-out mouse model (*Vim-/-*). Genomic deletion of vimentin was initially characterized by Colucci-Guyon in 1994 (5). *Vim-/-* mice are viable and fertile. Evaluation of vimentin in the aortic endothelium confirmed the lack of this type III intermediate filament in the knock-out mice, but a contrasting robust expression was noted in wild-type controls (**Figure 2A**). Transverse sections of adult dorsal aorta also showed high levels of vimentin in wild-type smooth muscle cells of the tunica media and its absence in null mice (**Figure 2B**). Interestingly, *en face* evaluation of the aorta of *Vim-/-* mice revealed the retention of an ostium in the area associated with the connection to the ductus arteriosus (**Figure 2C**).

The dynamics of DA closure were then tracked in wild-type and *Vim*-/- mice at time points ranging from P1 to 72 weeks of age (**Figure 2D**). Both groups showed striking and similar changes in the width of the DA with marked constrictions of the tunica media. To rigorously quantify the progress of closure, we evaluated 28 control mice and 31 Vim-/- mice from P1 to 1 year of age (Figure 2E). The data showed differences only in adult mice, indicating a lack of complete remodeling in mice deleted for Vim. Macroscopic evaluation rendered the wild-type and *Vim* -/- mice nearly indistinguishable, except for the clear presence of blood cells in the DA of *Vim*-/- mice at both early and late stages. Using the presence of blood in the DA as a read-out for patency, we found that all adult *Vim*-/- mice evaluated showed incomplete closure (**Figure 2F).** This was further confirmed by cross-sections of *Vim*-/- DA from mice at 52w of age (**Figure 2G**) and was consistent with the openings noted in the lateral aspects of the aorta of *Vim*-/- where these ducti connect (**Figure 2C**). Additional histological evaluations of ducti from control and *Vim*-/- mice revealed clear retention of the patency and absence of full cellular remodeling of both the tunica intima and media (**Figure 2H**). Combined these findings support the conclusion that vimentin is required for complete remodeling of the ductus arteriosus and obliteration of the vascular lumen. We were

naturally intrigued about potential underlying mechanisms and evaluation of the literature revealed links between vimentin and Notch (6,7).

It is well-accepted that signaling between endothelial cells and vascular smooth muscle cells through the Notch pathway contributes to arterial remodeling. Additionally, it has been demonstrated that the absence of the Notch receptor Jagged1 in endothelial cells, results in patent ductus arteriosus (8). Interestingly, vimentin plays an important role in Notch transactivation by endothelial cells (6). Specifically, depletion of vimentin reduces Jagged1-Notch signaling due to alterations in cellular stiffness which likely impair the pulling force required in Jagged1-Notch interactions that precede ADAM cleavage. Therefore, we explored expression patterns of Notch signaling in the ductus arteriosus. Interestingly, we found that Jag1 and Notch1 expression in endothelial and vascular smooth muscle cells increased at P0.5, coincident with Vimentin upregulation during DA remodeling **(Figure 2I**). Therefore, the concurrent expression of vimentin and Notch1/Jag1 suggests PDA may emerge in *Vim*-/- mice because of ineffective signaling between Jag1 (in endothelial cells) and Notch1/3 (in smooth muscle cells).

DISCUSSION

Resolution of individual transcriptional changes at the cellular level offers an unprecedented opportunity to seek answers to questions that require complex developmental events. In the case of the remodeling of the ductus arteriosus, scRNAseq revealed a large number of transcriptional alterations in the endothelial, smooth muscle and fibroblast compartments which will likely offer opportunities for exploration by multiple laboratories.

Seeking transcripts that sharply increase in the aorta shortly after birth, we identified vimentin, an intermediate filament protein highly expressed in both endothelial and smooth muscle cells. Interestingly, while viable and fertile (5), we found that mice with genomic deletion of vimentin

exhibit incomplete closure of the ductus arteriosus due to failure in the last stages of vascular remodeling. In fact, our data show that *Vim*-/- mice at 1 year of age, still exhibit an open lumen with visible circulating blood. We also found alterations in the remodeling of the tunica media, retention of smooth muscle cell markers in the layers proximal to the endothelium and a lack of complete transition of smooth muscle cells towards a fibroblastic phenotype.

Intermediate filaments cooperate with other elements of the cytoskeleton to provide structural support and mechanical integration between the cell surface , organelles and the nucleus (4,9,10). However, intermediate filaments distinguish themselves from other members of the cytoskeleton by their higher mechanical integrity and resistance to rupture (9,11). This is particularly important for cells that either withstand and/or impose physical forces, such as those occurring during vascular remodeling. While other types of intermediate filaments are expressed by smooth muscle (e.g., desmin) and by endothelial cells (e.g., keratins 8 and 18), the levels of vimentin supersede those in both cell types. Furthermore, in addition to their roles in maintaining mechanical integrity, vimentin undergoes impressive spatial rearrangement in smooth muscle cells during contraction and upon stimulation by several agonists (12,13). Importantly, vimentin has been implicated in the distribution of Ca^{2+}/calmodulin-dependent protein kinase II (CamKII), a kinase critical in regulating smooth muscle cell contraction (14). In endothelial cells, vimentin has been implicated in barrier function and cell adhesion (15), but no studies have explored the potential role of vimentin during vascular remodeling.

The process of complete closure of the DA is known to require smooth muscle cell migration and proliferation, disruption of the internal elastic lamina, alterations in extracellular matrix production, endothelial cell proliferation and monocyte adhesion(2,3,8,16–22). Many of these events require Notch signaling, particularly those associated with smooth muscle cell contraction and endothelial cell proliferation (6,8). Recently, vimentin was shown to contribute to the mechanochemical

transduction pathway that regulates multilayer cross-talk and structural homeostasis through the Notch signaling pathway (6). While additional mechanistic experiments in the context of DA remodeling are required to definitively establish a causal link, the low stiffness due to lack of vimentin is consistent with deficiencies in force generation needed for Notch signaling.

Our findings indicate that the initial stages of DA remodeling are not compromised by the absence of vimentin. Instead, the later stages that promote complete closure of the lumen are the ones impaired. Little is known about the cellular and molecular processes associated with the closure of a vascular lumen. Our findings highlight the exquisite requirement of vimentin for the completion of this process in the ductus arteriosus.

ACKNOWLEDGEMENTS

We would like to thank the Jonsson Comprehensive Center at UCLA for sequencing of scRNAseq libraries and the Mouse Histology and Phenotyping core at Northwestern University. A special thanks to Michelle Steel and Snezana Mirkov for support with animal colonies, assistance with husbandry and mouse experimentation.

SOURCES OF FUNDING

This work was supported by R35HL140014 to M.L. Iruela-Arispe, Howard Hughes Medical Institute Gilliam Fellowship (GT11560) to Gloria Hernandez. Northwestern University Molecular and Translational Cardiovascular Training Program (T32HL134633; SP0040691) to Jocelynda Salvador. R Goldman and K Ridge are supported by NIGMS PO1 GM096971.

CONTRIBUTIONS

JC and GEH performed and designed experiments, wrote and edited the manuscript

FM performed bioinformatic analysis of scRNAseq data

CWA performed experiments

KMR provided the vimentin KO mouse and intellectual input

RG and **MP** provided intellectual discussion.

MLIA conceived the study, designed the experiments, wrote and edited the manuscript

All authors discussed the results and had the opportunity to comment on the manuscript.

MATERIALS AND METHODS

Mice: For scRNA-seq experiments, C57BL/6 mice at the following stages were used: E18.5, P0.5 and P5. Libraries were generated from ducti of pooled littermates (8-9 mice per library, both sexes). The 129/Sv6 vimentin-deficient (*Vim-/-*) mice were a gift from Albee Messing (Madison, WI)

Single-cell isolation: For cell isolation, aorta and ducti were dissected in versine; vessels were minced into small pieces and placed in 1mL of digestion buffer containing DNase1, 1M HEPES, Libase, and HBSS at 37C for 20mins. Once tissue was digested into a single cell suspension, cells were washed, pelleted, and passed through a 40μm filter. The final cell suspension was in 0.04%BSA.

scRNA-seq libraries were generated using 10X Genomics Chromium Single Cell 3' Library & Gel Bead Kit v3. Cells were loaded accordingly following the 10X Genomics protocol with an estimated targeted cell recovery of 6000 cells. Sequencing was performed on NovaSeq6000 (Pair-end, 100 base pairs per read). The digital expression matrix was generated by demultiplexing, barcode processing, and gene unique molecular index counting using the Cellranger count pipeline (version 4.0.0, 10X Genomics). Multiple samples were merged using the Cellranger aggr pipeline. To identify different cell types and find signature genes for each cell type, the R package Seurat (version 3.1.2) was used to analyze the digital expression matrix.

Specifically, cells that express <100 genes or <500 transcripts were filtered out. The data were normalized using the NormalizeData function with a scale factor of 10,000. The genes were then scaled and centered using the ScaleData function. Principal component analysis (PCA), Uniform Manifold Approximation and Projection (UMAP) were used to reduce the dimensionality of the data. Cell clusters were identified using the FindClusters function. The cluster marker genes were found using the FindAllMarkers function. Cell types were annotated based on the cluster marker genes. Heatmaps, violin plots and gene expression plots were generated by DoHeatmap, VlnPlot, FeaturePlot functions, respectively. Data will be deposited on GEO and an accession number will be included upon acceptance of the manuscript.

Immunofluorescence: For whole-mount aorta staining, mice were euthanized and perfused with 2% paraformaldehyde (PFA). The aortae were dissected from the backbone, cleaned, filleted open, and pinned down on silicone-coated plates with the endothelium facing up and left in 2% PFA overnight. The following day, aortae were washed three times in 1x PBS, blocked for 1hr, and primary antibodies were added in fresh blocking buffer overnight. On the second day the aortae were washed three times in 1x PBS and secondaries were added in fresh blocking buffer and allowed to incubate for 2 hrs followed by three washes. After the washes they were mounted onto slides using ProLong Gold Antifade Mounting Medium (Thermo Fischer Scientific P36930) covered with a coverslip and sealed with nail polish. The following primary antibodies and concentrations were used: Anti-Vimentin (Encor Biotech, # CPCA-Vim, 1:1000), anti-VE-cadherin goat polyclonal (discontinued- Santa Cruz Biotechnology #sc-6458, 1:200), anti-ERG (ABCAM #ab92513, 1:200). PECAM antibody was graciously provided by Dr. Bill Muller (Northwestern). The following secondary antibodies were used: Donkey anti-Rabbit Alexa Fluor™ 568 (Invitrogen A10042) used at 1:400; FITC-Donkey anti-Chicken (Thermo Fisher SA1-72000) used at 1:400; Donkey Anti-Goat Alexa Fluor® 647 (Abcam ab150135) used at 1:400; Alexa Fluor® 488 AffiniPure Goat Anti-Armenian Hamster (Jackson ImmunoResearch Laboratories127-545-160)

used at 1:400; and all preparations were stained with DAPI (Thermo Fisher D1306) 1:500. Images were taken on a A1R HD25 confocal microscope (Nikon) using 20x, 40x and 60x objectives.

For histological sections: ducti arteriosus were dissected, fixed in 2% PFA overnight, washed 3 times in PBS and embedded first in Histogel under a dissecting microscope and later in paraffin. Blocks were sectioned at 5μM and stained with H&E by Northwestern Mouse Histology and Phenotyping Laboratory. Other sections were processed with the following primary antibodies: Anti-vimentin (Encor Biotech, # CPCA-Vim), Anti-Smooth Muscle alpha actin– Cy3 (C6198), Anti-smooth muscle Myosin heavy chain 11 (Abcam ab224804), Anti-Calponin 1 (Abcam ab46794), Anti-SM22 alpha (Abcam ab14106). The following secondary antibodies were used: Alexa-Fluor Donkey anti-Rabbit 568, FITC-Donkey anti-Chicken, and all preparations were also stained with DAPI (Thermo Fisher D1306).

Measurements of the ducti at several ages were done on an Echo Revolve microscope equipped with a micrometer for X and Y measurements. The ducti still attached to the dorsal aorta were carefully dissected and pinned onto silicone-coated dishes. Measurements were obtained always at the same distance from the aorta for accurate comparisons using 1.25X and 4X objectives.

Statistics: To quantify closure of the DA, a ratio of the outer width of the ductus arteriosus (DA) to the width of the descending aorta (AO) was calculated for each aorta at each time point. Measurements were done on the Echo Revolve using the annotation tool, and statistics were performed on Graphpad Prism. An unpaired Student's t-test was used to compare between Wild-type and Vimentin KO measurements at each developmental time point. A p-value of less than 0.05 was considered statistically significant.

FIGURES

Figure 3.1

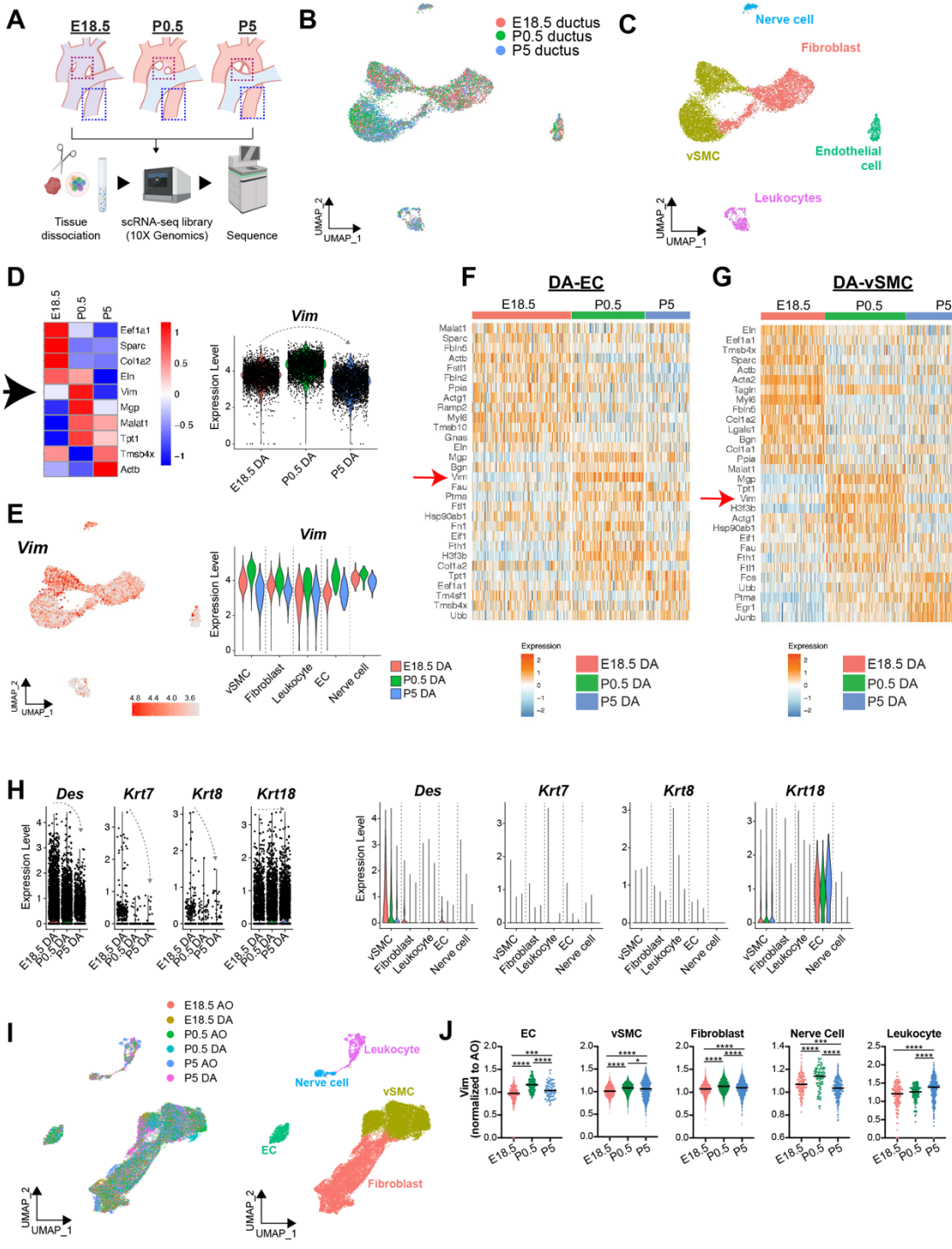

Figure 3.1. Vimentin expression increases in all vascular cell types during the closure of the ductus arteriosus

A. Schematic illustrating the isolation of ductus arteriosus (magenta dotted line) and aortic (blue dotted line) cells for single-cell RNA sequencing. **B**. Uniform manifold approximation and projection (UMAP) plot of cells from three independent libraries: E18.5, P0.5, and P5 ductus arteriosus. 8-9 ductus arteriosus (ductus, DA) were used per library. **C**. UMAP analysis and heat map-style representation of canonical lineage markers (color key represents expression level). **D**. Left: heat map of the top 10 genes in each ductus arteriosus library at the respective time points (E18.5, P0.5 and P5). Arrow identifies vimentin (*Vim*) as the transcript that shows the highest expression at P0.5 with drastic dropped at P5. Right: graph illustrating bell-shape expression pattern of vimentin. **E**. Left: UMAP representation of Vimentin (*Vim*) expression. Right: Vim expression levels in each cell type at the indicated time-points. **F**. Heat map of the top 30 genes in the ductus arteriosus – endothelial compartment (DA-EC). Note clear and sharp upregulation of vimentin at P0.5 (red arrow). **G**. Heat map of the top 30 genes in the ductus arteriosus – vascular smooth muscle cell compartment (DA-vSMC). Note clear and sharp upregulation of vimentin at P0.5 (red arrow). **H**. Violin plots showing overall expression of selected intermediate filaments in the ductus arteriosus at each given time point shown as normalized gene expression per cell. Dotted grey arrows note expression trends through time. Also shown on the right, selected intermediate filament expression in the ductus arteriosus at each time point per cell type. **I**. UMAP plot of cells from 6 libraries: the DA and aorta (AO) at E18.5, P0.5, and P5, isolated from the same mice and cellular identities assigned to each cluster (UMAP on the right). **J**. Vim expression in each cell type at the given time points, normalized to aortic cell *vim* expression.

Figure 3.2.

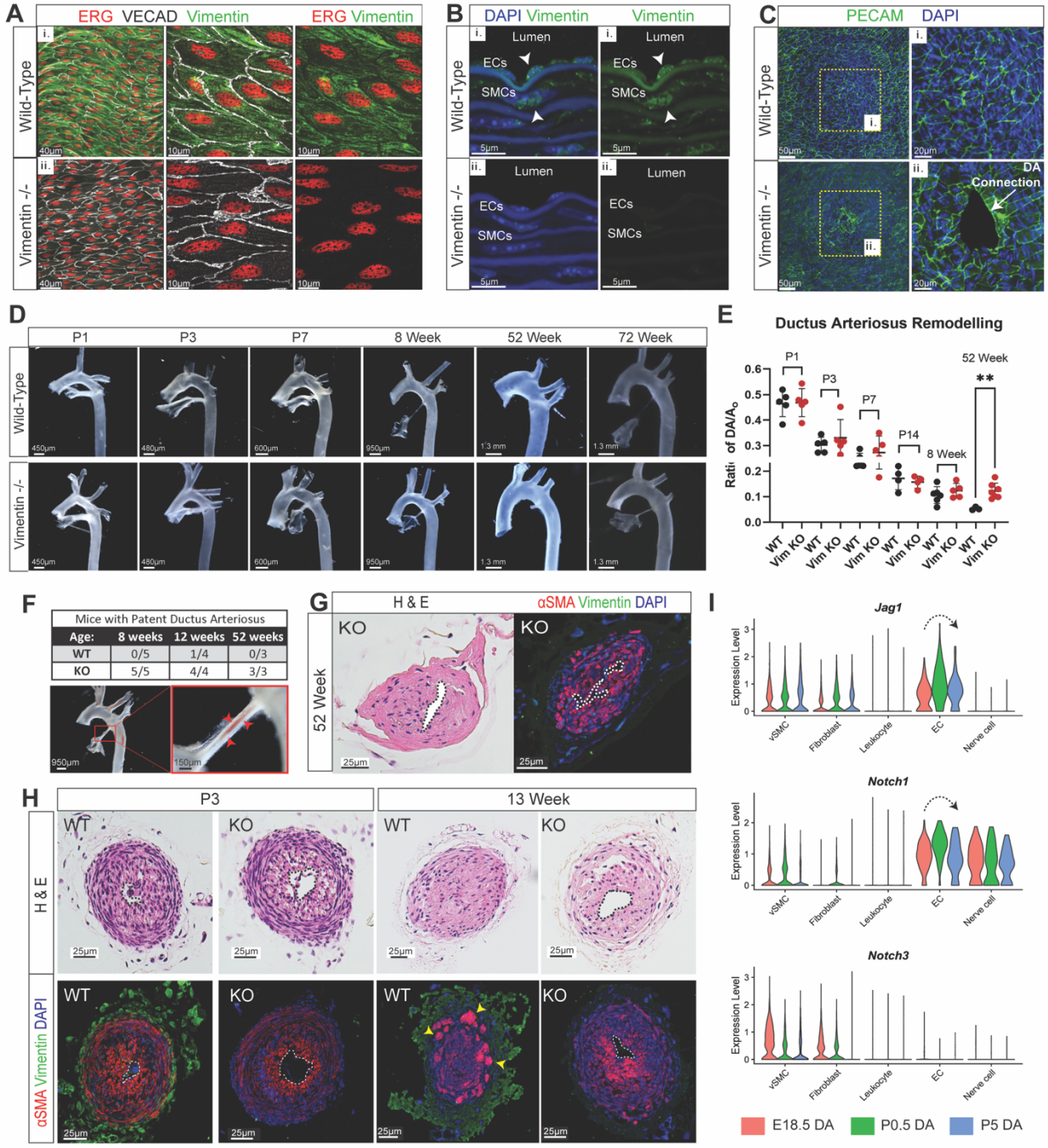

Figure 3.2. Loss of Vimentin leads to patent ductus arteriosus

A. *En face* immunofluorescence preparation of aortae confirm the presence and absence of vimentin in the endothelium of the wild-type (WT) (i) and knock-out (*Vim-/-*) mice (ii), respectively. **B.** Transverse sections of the descending aorta of 8-week old WT and Vim-/- mice demonstrate the abundance of vimentin in endothelial cells (ECs) and smooth muscle cells (SMCs) in the

intimal and medial layers of the aorta, respectively. **C.** *En face* staining of the aortic endothelium in the region of the ductus arteriosus opening along the aorta in 52 week old WT and *Vim-/-* mice. Note, *Vim-/-* reveal patency of the ductus arteriosus (ii). **D**. Light imaging of aortae at different developmental timepoints highlights the closure of the ductus arteriosus and the enlargement of the aorta in Wild-type and *Vim-/-* mice from P1 to 52 weeks of age. **E.** Quantification of the width of the ductus arteriosus (DA) normalized to the width of the descending aorta (AO) from bright field images shown in Figure 2D. (n=6 per group, **p<0.001). **F.** Quantification of proportion of adult mice (8weeks-52weeks) with patent ductus arteriosus. n=3-5 mice per time point. **G.** Transversal sections of the DA from 52 week *Vim-/-* mice stained with H&E and stained for alpha smooth muscle alpha actin (red), vimentin (green) and DAPI (blue). Despite lack of observable differences in outer widths of the vessel in **2D & 2E** the lumen is retained and SMCs still retain smooth muscle cell markers. **H.** Transverse sections of the ductus arteriosus in WT and *Vim-/-* mice at P3 and 13 weeks of age stained for vimentin (green) and the smooth muscle marker, alpha-SMA (red). Note clear retention of lumen at 13 weeks in *Vim-/-* in contrast to controls. Also note alterations in smooth muscle cells in WT mice (yellow arrows) not detected in *Vim-/-* mice. **I.** Violin plots showing overall expression of Jag1, Notch1, and Notch3 in the ductus arteriosus at each given timepoint shown as normalized gene expression per cell. Dotted grey arrows note expression trends through time.

Supplemental Figure 3.1

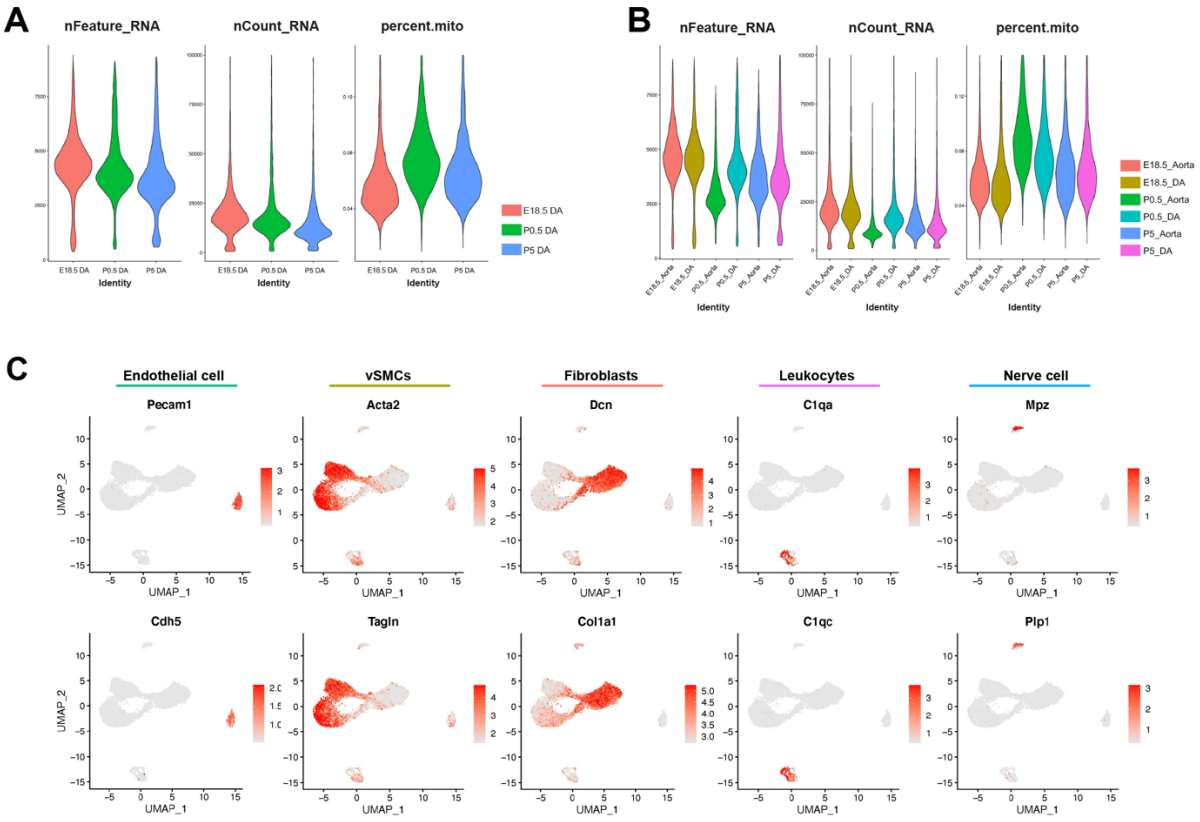

Supplemental figure 3.1 Quality control of scRNA-seq data sets

A. Evaluation of data quality of the three libraries generated (E18.5, P0.5, and P5). The average number of genes detected per cell (nFeature), the total number of molecules detected per cell (nCount), and the perfect of mitochondrial genes per cell (percent.mito) for each library. Cells having more than 3,000 genes, at least 1,000 unique molecular identifiers, and at most 10% mitochondrial gene expression were selected. **B**. Comparison between Aorta and Ductus Arteriosus (DA) libraries at each time point using the same parameters as in panel A. **C**. UMAP analysis and heat-map style representation of canonical lineage markers (color key represents expression level).

REFERENCES

1. Schneider DJ, Moore JW. Patent ductus arteriosus. Circulation. 2006 Oct 24;114(17):1873–1882.

2. Hsu H-W, Lin T-Y, Liu Y-C, Yeh J-L, Hsu J-H. Molecular Mechanisms Underlying Remodeling of Ductus Arteriosus: Looking beyond the Prostaglandin Pathway. Int J Mol Sci. 2021 Mar 22;22(6).

3. Hung Y-C, Yeh J-L, Hsu J-H. Molecular mechanisms for regulating postnatal ductus arteriosus closure. Int J Mol Sci. 2018 Jun 25;19(7).

4. Patteson AE, Vahabikashi A, Pogoda K, Adam SA, Mandal K, Kittisopikul M, et al. Vimentin protects cells against nuclear rupture and DNA damage during migration. J Cell Biol. 2019 Dec 2;218(12):4079–4092.

5. Colucci-Guyon E, Portier MM, Dunia I, Paulin D, Pournin S, Babinet C. Mice lacking vimentin develop and reproduce without an obvious phenotype. Cell. 1994 Nov 18;79(4):679–694.

6. van Engeland NCA, Suarez Rodriguez F, Rivero-Müller A, Ristori T, Duran CL, Stassen OMJA, et al. Vimentin regulates Notch signaling strength and arterial remodeling in response to hemodynamic stress. Sci Rep. 2019 Aug 27;9(1):12415.

7. Antfolk D, Sjöqvist M, Cheng F, Isoniemi K, Duran CL, Rivero-Muller A, et al. Selective regulation of Notch ligands during angiogenesis is mediated by vimentin. Proc Natl Acad Sci USA. 2017 Jun 6;114(23):E4574–E4581.

8. Feng X, Krebs LT, Gridley T. Patent ductus arteriosus in mice with smooth muscle-specific Jag1 deletion. Development. 2010 Dec;137(24):4191–4199.

9. Chang L, Goldman RD. Intermediate filaments mediate cytoskeletal crosstalk. Nat Rev Mol Cell Biol. 2004 Aug;5(8):601–613.

10. Lowery J, Kuczmarski ER, Herrmann H, Goldman RD. Intermediate filaments play a pivotal role in regulating cell architecture and function. J Biol Chem. 2015 Jul 10;290(28):17145–17153.

11. Köster S, Weitz DA, Goldman RD, Aebi U, Herrmann H. Intermediate filament mechanics in vitro and in the cell: from coiled coils to filaments, fibers and networks. Curr Opin Cell Biol. 2015 Feb;32:82–91.

12. Li Q-F, Spinelli AM, Wang R, Anfinogenova Y, Singer HA, Tang DD. Critical role of vimentin phosphorylation at Ser-56 by p21-activated kinase in vimentin cytoskeleton signaling. J Biol Chem. 2006 Nov 10;281(45):34716–34724.

13. Tang DD, Bai Y, Gunst SJ. Silencing of p21-activated kinase attenuates vimentin phosphorylation on Ser-56 and reorientation of the vimentin network during stimulation of smooth muscle cells by 5-hydroxytryptamine. Biochem J. 2005 Jun 15;388(Pt 3):773–783.

14. Marganski WA, Gangopadhyay SS, Je H-D, Gallant C, Morgan KG. Targeting of a novel Ca+2/calmodulin-dependent protein kinase II is essential for extracellular signal-regulated

kinase-mediated signaling in differentiated smooth muscle cells. Circ Res. 2005 Sep 16;97(6):541–549.

15. Dave JM, Bayless KJ. Vimentin as an integral regulator of cell adhesion and endothelial sprouting. Microcirculation. 2014 May;21(4):333–344.

16. Mueller PP, Drynda A, Goltz D, Hoehn R, Hauser H, Peuster M. Common signatures for gene expression in postnatal patients with patent arterial ducts and stented arteries. Cardiol Young. 2009 Aug;19(4):352–359.

17. Hsieh Y-T, Liu NM, Ohmori E, Yokota T, Kajimura I, Akaike T, et al. Transcription profiles of the ductus arteriosus in Brown-Norway rats with irregular elastic fiber formation. Circ J. 2014 Mar 19;78(5):1224–1233.

18. Shelton EL, Ector G, Galindo CL, Hooper CW, Brown N, Wilkerson I, et al. Transcriptional profiling reveals ductus arteriosus-specific genes that regulate vascular tone. Physiol Genomics. 2014 Jul 1;46(13):457–466.

19. Goyal R, Goyal D, Longo LD, Clyman RI. Microarray gene expression analysis in ovine ductus arteriosus during fetal development and birth transition. Pediatr Res. 2016 Jun 3;80(4):610–618.

20. Liu NM, Yokota T, Maekawa S, Lü P, Zheng Y-W, Taniguchi H, et al. Transcription profiles of endothelial cells in the rat ductus arteriosus during a perinatal period. PLoS One. 2013 Sep 27;8(9):e73685.

21. Saito J, Kojima T, Tanifuji S, Kato Y, Oka S, Ichikawa Y, et al. Transcriptome Analysis Reveals Differential Gene Expression between the Closing Ductus Arteriosus and the Patent Ductus Arteriosus in Humans. J Cardiovasc Dev Dis. 2021 Apr 16;8(4).

22. Bökenkamp R, Raz V, Venema A, DeRuiter MC, van Munsteren C, Olive M, et al. Differential temporal and spatial progerin expression during closure of the ductus arteriosus in neonates. PLoS One. 2011 Sep 6;6(9):e23975.

Chapter 4. Aortic intima resident macrophages are essential for the maintenance of the non-thrombogenic intravascular state

ABSTRACT

Leukocytes and endothelial cells frequently cooperate to resolve inflammatory events. In most cases, these interactions are transient in nature and triggered by immunological insults. Here, we report that in areas of oscillatory and disturbed blood flow, aortic endothelial cells permanently and intimately associate with a population of specialized macrophages. These macrophages are recruited at birth from the closing ductus arteriosus and share the luminal surface with the endothelium becoming interwoven in the tunica intima. Anatomical changes that affect hemodynamics, like in patent ductus arteriosus, alter macrophage seeding to coincide with regions of disturbed flow. Aortic resident macrophages expand *in situ* via direct cell renewal and continue to grow in aged aortae. To clarify their biological significance, we used a dual diphtheria toxin induced-depletion system and found that absence of intimal macrophages led to thrombin-mediated endothelial cell contraction, progressive fibrin accumulation and formation of microthrombi that, once dislodged, caused blockade of vessels in several organs. Together the findings revealed that intravascular resident macrophages are essential to regulate thrombin activity and clear fibrin deposits in regions of disturbed blood flow. These results advance our knowledge of how vascular endothelial cells profit from this unique interaction with macrophages to preserve a non-thrombogenic surface, prevent intravascular clotting, and ensure vascular health.

INTRODUCTION

As gatekeeper of the cellular traffic between blood and tissues, the endothelium is well equipped to interact with hematopoietic cells. Endothelial cells enable the well-coordinated process of diapedeses that includes, capture, rolling, and finally transmigration of leukocytes

across the vascular barrier [1–4]. These events rely on complex and sequential molecular interactions whereby these cell types cooperate to mount and resolve inflammatory responses at the level of venules and capillaries [2,3]. In large arteries, interactions of the endothelium with inflammatory cells are mostly known for their association with atherosclerosis, a chronic inflammation of the vascular wall [5,6]. In this pathology, leukocytes occupy the subendothelial layer forming a neointima that progressively expands by the constant influx and local proliferation of inflammatory cells [5,7–9].

Other types of interactions between arterial endothelium and inflammatory cells have been shown, particularly a population of non-classical monocytes (Ly6C^{low}, CCR2^{low}, Cx3cr1^{high}) better referred to as patrolling monocytes that are thought to promote endothelial integrity and vascular health [10–12]. In addition to patrolling monocytes, myeloid cells with a highly dendritic appearance were also described in the luminal aspect of the aorta, especially at sites prone to develop atherosclerosis, like the aortic arch [13,14]. Despite their conspicuous location, the contribution of these myeloid cells to atherosclerosis was proved to be minimal, as their elimination only slightly delayed onset of the disease with no impact on duration or burden [15]. Thus, the mechanisms behind their peculiar distribution, specific seeding time and, more importantly, their function have remained puzzling.

Here we show that the emergence of aortic myeloid cells is not pathologically induced, instead it is developmentally triggered as part of natural hemodynamic changes at birth that result in localized disturbed flow dynamics. Genetic ablation of this aortic myeloid resident population promotes fibrin deposition and microthrombi formation, clarifying their function as critical regulators of hemostasis.

RESULTS

Alterations of hemodynamics associated with birth promote the seeding of myeloid cells in the tunica intima of the aorta

The fetal circulation includes two parallel circuits with equal left and right ventricular pressures. At birth, this balance changes drastically due to multiple concurrent events that include interruption of placental circulation, inflation of the lungs, and shift in pulmonary blood pressure. All these changes result in high left ventricular pressure and closure of the ductus arteriosus, a fetal vessel that connects the pulmonary arteries to the aorta, an event that further magnifies the oscillatory flow in the lower curvature of the aortic arch (**Fig. 4.1a**). These alterations in hemodynamics are quickly sensed by endothelial cells which respond to these flow changes transitioning from elongated to polygonal shape in the lesser curvature of the aortic arch (**Fig. 4.1b, c**). Furthermore, evaluation of mouse embryos and neonates uncovered a burst of inflammatory cells exiting from the constricted ductus arteriosus and that seed the aorta, in tandem with the changes in hemodynamics (**Fig. 4.1d-f**). Interestingly from the onset of birth, this population of CD45+ cells continued to reside in areas of the aorta that experience oscillatory/disturbed flow, including the lesser curvature of the aortic arch and branch openings **(Fig.4.1g-i, Supplementary Fig.4.1a).** Initial characterization indicated that they also express CD11c (**Fig. 4.1h,j**). Curiously, CD11c+ cells were previously spotted in the aortic arch of adult healthy mice [13,14] raising the possibility that they might be the same population. We also found that CD11c+ cells progressively accumulate with age in the absence of pathologies or hypercholesterolemia (**Supplementary Fig. 4.1a-c**). However, they were not found in large veins, like the vena cava (**Supplementary Fig. 4.1d,e**), indicating that an arterial niche, including flow patterns may be required for their accumulation. Intimal immune cells were also absent from the carotids of healthy, adult mice (**Supplementary Fig. 4.1f**) and from the descending young aorta, except for branches (**Supplementary Fig. 4.1g**). We also observed that the distribution of these cells progressively broadened with age. In fact, the descending aorta of 52- and 78-week-old mice revealed ongoing accumulation of intimal immune cells even in areas of laminar flow (**Supplementary Fig. 4.1g-i**). These findings suggested underlying requirements for intimal myeloid cells seeding that although initially associated with oscillatory/disturbed flow, might also be tied to vascular aging.

A definitive link between onset of oscillatory flow and recruitment of CD11c+ cells was established using mouse models of patent ductus arteriosus (PDA). Failure in PDA closure significantly alters cardiovascular hemodynamics[16]. While viable and fertile [17], Vimentin$^{-/-}$ mice exhibit PDA in about 88% of adults, making them an ideal model to study myeloid cell distribution in adult aortae [18]. At 10wks of age, the ductus arteriosus in wild-type littermates becomes a solid fibrous structure that persists as the ligamentum arteriosum (**Fig. 4.1k**). In contrast, Vimentin$^{-/-}$ mice exhibit a viable ductus arteriosus which impacts patterns of disturbed flow distribution and the location of myeloid cells (**Fig. 4.1l**). The lesser curvature of the aortic arch of Vimentin$^{-/-}$ mice showed no intimal myeloid accumulation, instead myeloid cells were noted surrounding the openings of the ductus arteriosus, subclavian artery, and onset of the descending aorta (**Fig. 4.1l**).

The thin nature of the endothelial lining makes it difficult to ascertain the precise topological location of myeloid cells in relation to the endothelium. Thus, we performed 3D surface rendering using CDH5^{creERT2};R26^{tdtomato} reporter mice to label the endothelial monolayer tdTomato. Aortae were stained with CD45 and VE-cadherin in order to generate 3D depiction of the tunica intima. Surprisingly, intimal myeloid cells were neither above nor below the endothelium, but were instead interwoven within the endothelial monolayer with some immune cell processes projecting into and others below the lumen (**Fig. 4.2a**). *En face* scanning electron microscopy of the aortic arch stained with CD45 antibodies confirmed these findings (**Fig. 4.2b**). Additionally, 3D surface rendering using a reporter model that labels the tunica media (SM22^{cre};R26^{tdTomato}) revealed that these aortic immune cells were in fact located in the tunica intima, as per location within the VE-Cadherin stained layer (**Fig. 4.2c**). Finally, exposure of myeloid cells into the vascular lumen was additionally supported by injection of CD45 antibodies *in vivo* (**Fig. 4.2d,e**).

It has been previously reported that during transendothelial cell migration, leukocytes express Pecam-1 in order to adhere to the endothelial cells and therefore, preserve junctional integrity while crossing the endothelial barrier [2–4]. Interestingly, *en face* images showed Pecam-1

protein expression, suggesting that Mac^{AIRs} could bind to the endothelium via homophylic-heterotypic interactions and to prevent barrier disruption (**Fig. 4.2f**). To uncover if the Pecam-1+ regions were lumen facing or beneath the endothelial cells, we injected non-blocking Pecam-1 (390) antibody intravenously. *En face* images revealed Pecam-1+ regions in the cell bodies of inflammatory cells exposed to the lumen (**Fig. 4.2g**). Combined, these experiments revealed that in regions of oscillatory and disturbed flow the constituency of the endothelial layer is enriched by a population of myeloid cells that intimately co-exists with the endothelium in the absence of pathology and without breach of permeability.

scRNA-seq reveals the transcriptional identity of the aortic intimal immune cells

In order to recover cellular identities independent of defined labeling strategies, we turned to single-cell RNA sequencing (scRNA-seq) using specimens that were not FACS-sorted. We previously developed a unique isolation strategy that allows us to collect cells from the tunica intima avoiding prolonged enzymatic digestion or staging cells in suspension [19,20] (**Supplementary Fig. 4.2a**). Using this approach, we made 3 independent scRNA-seq libraries, capitalizing on regions containing an abundant number of intimal immune cells. Thus, we harvested intimal cells from the aortic arch of 8wk old C57BL/6 mice (**"**Young Arch") and from the descending aorta (thoracic and abdominal portions) of 78wk C57BL/6 old mice (**"**Aged Descending A,B"), where each library contained 6-8 aortae (**Supplementary Fig. 4.2b-e**; **Supplementary Table 1**). Comparisons between these groups would allow us to ascertain whether cells in young mice in areas of disturbed flow resemble those in laminar flow in aged mice. Using dimensionality reduction by the t-distributed stochastic neighbor embedding (t-SNE) analysis, we identified 10 distinct cell types and assigned cellular identities (**Supplementary Figure 4.2f; Supplementary Table 2,3**) based on canonical lineage markers (**Supplementary Figures 4.2g and 4.2h**). Within the 10 cell types, we identified two distinct macrophage populations based on *Fcgr1* (CD64) and *Adgre1* (F4/80) expression (**Supplementary Figures**

4.2h), which we suspected to include the intimal immune cells. One of the macrophage populations highly expressed *Lyve1* (lymphatic endothelium hyaluronan receptor-1), *F13a1*, and *Mrc1* (CD206), well-known markers of adventitia macrophages [15,21–24] (**Supplementary Fig. 4.2i,j**), suggesting this macrophage population came from the adventitia. While our isolation method enriches for cells in the tunica intima, few cells from the other aortic layers (tunica adventitia and media) were also captured[19,20] (**Supplementary Fig. 4.2f and 4.2g**). Therefore, we predicted that one of the two macrophage populations identified was from the adventitia. To definitively test this prediction, we performed single cell sequencing from dissected aortic adventitia (**Supplementary Fig. 4.3a-g)** and compared the two distinct myeloid populations identified. For this, we selected the CD14 positive cells from the purified adventitia and aortic libraries (**Supplementary Fig. 4.3c-e)** and were able to discern two clear clusters of macrophages from the aorta: a Lyve1 positive/CD64 group of cells which was also present in the libraries from the adventitia and clearly related to typical adventitial macrophages and a second cluster that showed distinct expression of Mmp12 and Mmp13 (**Supplementary Fig. 4.3f,g)** which was unique to the intima-enriched aortic libraries and absent from the adventitia. Furthermore, we compared the Mmp12/13 aortic macrophage population with macrophages in the Tabula muris atlas[25] (**Supplementary Fig. 4.4a-h**) and resident macrophages characterized in more recent publications[22] (**Supplementary Fig. 4.4i**). From this analysis, it became clear that the aortic population of intimal macrophages was especially distinct from resident macrophage populations present in other organs to date, with salient and clear expression of Mmp12 and Mmp13 as its main, albeit not unique, distinctive feature.

Subsequently, we compared the Mmp12 and Mmp13 macrophage population to a recently identified group of macrophages isolated from whole aortas and referred to as Mac^{AIRs} [15]. Comparisons between the intima Mmp12/13+ population presented here to the pre-hypercholesterolemic aortic Mac^{AIRs} population[15] revealed that they were transcriptionally identical (**Supplementary Table 4**). Interestingly, we also found that the young arch and old thoracic

endothelial-associated macrophage populations were identical (**Supplementary Table 5**), suggesting the endothelial niche is responsible for the underlying tissue-specific imprinting of these macrophages, no matter age or location. This realization prompted two immediate questions: Were these populations progeny of the CD45+ cells exiting the ductus arteriosus? And, more importantly, what was their biological relevance?

Aortic intima resident macrophages (Mac^{AIRs}) are a distinct macrophage population that seeds the aorta at birth

In order to clarify the function of Mac^{AIRs} and delve into their developmental origin, we first performed differential expression analysis to seek as many unique markers as possible. As per direct comparisons with adventitial macrophages and Tabular muris atlas, we found that Mac^{AIRs} expressed significantly higher transcriptional levels of matrix metalloproteinases (*Mmp12, Mmp13*; **Supplementary Fig. 4.2i,j**) and exhibited increased expression of immune cell activation genes (*Il1b*, *Ccl3*, *Ccl4*, *Tnf*, *Cxcl2*, *Cxcl16*; **Supplementary Fig. 4.2i,j; Supplementary Table 6-8**). In addition, Mac^{AIRs} displayed genes involved with wound healing / identification of dying cells (*Axl*, *Tyrobp*, *CD44*, *CD74*; **Supplementary Fig. 4.2i,j; Table S6-8**) and showed higher expression levels of antigen presenting genes, such as major histocompatibility complex class II (MHC class II) encoding genes (*H2-Aa*, *H2-Ab1*, *H2-Eb1*, and *H2-M2*; **Supplementary Fig. 4.2i,j; Supplementary Table 6-8**). In contrast, adventitia *Lyve1*^{hi} macrophages expressed genes associated with M2-like macrophages *(F13a1, Folr2* and *Mrc1 (CD206))*; **Supplementary Fig. 4.2i,j**; **Supplementary Table 7,8**).

To match the expression profile to their presumed progenitors, immunohistochemistry was performed on aortae of P7 and adult mice for targets unique to Mac^{AIRs} (Mmp13, Cxcl16, and CD11c). Intimal CD45+ cells colocalized with Mac^{AIR} markers (**Supplementary Fig. 4.5a,b**) whereas, in the adventitia, no CD45+ cells showed expression of Mac^{AIR} markers (**Supplementary Fig. 4.5c**). We also found that Mac^{AIRs} expressed Cx3cr1 (fractalkine receptor)

transcripts (**Supplementary Fig. 4.5d**) and protein (**Supplementary Fig. 4.5e**). Moreover, using an inducible Cx3cr1 reporter model (Cx3cr1^{creERT2};R26^{tdTomato}), 98% of all intimal CD45+ cells in adult aortae were labeled tdTomato (**Supplementary Fig. 4.5f**), which also colocalized with Cxcl16 protein expression (**Supplementary Fig. 4.5g**); thus, demonstrating the activity of the *Cx3cr1* promoter, which was later used in lineage tracing analysis. Additionally, using this transgene, intimal CD45+ cells in P5 aortae were also labeled by the reporter post- tamoxifen treatment (P1 and P3), further indicating that Mac^{AIRs} seed the aorta immediately post-birth (**Supplementary Fig. 4.5h**). Overall, these findings support the conclusion that the immune cells accumulating and residing in the tunica intima after birth were Mac^{AIRs} progenitors.

To more definitively confirm origin and the macrophage identity of Mac^{AIRs} (versus dendritic cells (DCs)), we assessed recombination labeling using the *Csf1r*^{MerCreMer};*R26*^{tdTomato} macrophage fate-mapping model. In this transgenic model, we found all intimal immune cells (CD45+) to also be labeled by the reporter gene tdTomato (**Supplementary Fig. 4.5i**). Moreover, all intimal immune cells expressed CD68 protein (**Supplementary Fig. 4.5j**). Additionally, Mac^{AIRs} did not express DC master regulator transcription factor *Zbtb46* [26] nor classical DC markers *CD8a, Ccr7* (**Supplementary Fig. 4.5k**), *CD103*, *33D1*, or *Mycl* (data not shown, genes not detected in dataset). Furthermore, Mac^{AIRs} were shown to phagocytose dying (annexin +) endothelial cells *in vivo* (**Supplementary Fig. 4.5l**), providing functional evidence of their macrophage identity. Thus, Mac^{AIRs} are a transcriptionally unique macrophage population that takes residency in the tunica intima of the aorta shortly after birth in regions of oscillatory and disturbed flow.

Mac^{AIRs} are self-maintained throughout adulthood

It is now understood that many tissue-resident macrophages are maintained through self-renewal without contribution from circulating monocytes [27,28]. EdU incorporation assays showed that in a 2h pulse, 5.4% of Mac^{AIRs} were undergoing DNA replication *in situ* in the adult arch (**Supplementary Fig. 4.6a-c**), suggesting that Mac^{AIRs} followed the trend of other resident

macrophages. Long-term replenishment was assessed by lineage tracing with pulse-labeling *Cx3cr1*^{creERT2};*R26*^{tdTomato} mice and evaluation 10- and 20- wks post-labeling (**Supplementary Figures 4.6d,e**). To control for the possible contribution of circulating cells using this model, we also quantified levels of tdTomato positive circulating cells. FACS analyses indicated that after 3wks, CD45+ tdTomato+ peripheral blood was negligible (less than 0.5%; **Supplementary Fig. 4.6f,g**) and thus, negating the possibility that cells from the circulation contributed to reporter positive Mac^{AIRs} after 20-wks post-tamoxifen. In this manner, absence of circulating tdTomato+ cells allowed us to ask whether monocytes participated in the maintenance of Mac^{AIRs}. Although the labeling frequency of Mac^{AIRs} decreased by 10% after 10-wks post-tamoxifen injection, we noted that reporter expression remained constant for an additional 10wks (20wks total) (**Supplementary Fig. 4.6e, h**). This finding supports the conclusion of local self-renewal with negligible contribution from circulating monocytes.

To further confirm these findings, we performed parabiosis experiments using adult GFP+ and wild-type (WT) mice. As follows, both mice shared a chimeric circulation for 5-wks (**Supplementary Fig. 4.6i**). The experiment allowed for all circulating cells to access the aortic regions of interest (i.e. the lesser curvature). The presence of GFP+ intimal immune cells incorporated in the WT mice would infer monocyte contribution and vice versa (**Supplementary Fig. 4.6i**). Additionally, we only used mice with efficient parabiosis, which was confirmed by examining the chimerism of CD45+ peripheral blood cells (**Supplementary Fig. 4.6j**). Evaluation of the lesser aortic curvature in the WT mice revealed no GFP+ intimal immune cells (**Supplementary Fig. 4.6k**), proving further strength to the conclusion that Mac^{AIRs} maintenance was independent of circulating monocytes. This conclusion was further strengthened by clonal analysis of an inducible multicolor fluorescent labeling model (Cx3cr1^{creERT2};R26^{Rainbow}) whereby expression of cre-recombinase in cells expressing Cx3cr1 would randomly recombine given rise to three possible colors (**Supplementary Fig. 4.6l**). Here labeling was done at 8 weeks and clonal

expansion evaluated 9 months later (at 11months). The data strongly argues that Mac^{AIRs} are self-maintained.

Mac^{AIRs} are the progeny of definitive hematopoietic cells that exit the ductus arteriosus at birth and expand through self-renewal

Mac^{AIRs} colonize the aorta as they exit from the ductus arteriosus and migrate to areas of disturbed flow. After this initial wave of migration, Mac^{AIRs} expand in number by local proliferation (**Figure 4.3a**). Nonetheless, lineage tracing was required to fully ascertain adult progeny. Thus, we performed lineage analysis using the inducible *Cx3cr1*^{creERT2};*R26*^{tdTomato} reporter model to label Mac^{AIRs} immediately post-birth and follow their descendants over time (**Figures 4.3b,c**). Using this model, 63% of intimal CD45+ cells were tdTomato positive at P7 after administration of tamoxifen after birth. By 4wks we found 91% of intimal CD45+ cells in aortae retained the tdTomato labeling (**Fig. 4.3d-f**). We interpret the increase from P7 (63%) to 4wks (91%) to indicate that only those inflammatory cells expressing Cx3cr1 were successfully retained in the endothelium. Importantly, at 4wks of age less than 0.5% of peripheral blood cells were tdTomato positive (**Fig. 4.3f**), supporting the absence of contributions from circulating cells. Therefore, these data indicate that the Mac^{AIRs} that enter the aorta postnatally expand via self-renewal and colonize the lesser curvature of the aortic arch with minimal (if any) input from circulating monocytes.

To assess clonal expansion of the Mac^{AIRs} at early time-points, we again used the inducible Cx3cr1^{creERT2};R26^{Rainbow} model to ascertain clonality and tracing (**Fig. 4.3g**). Using this model, pups were treated with tamoxifen immediately post-birth to induce stochastic genetic recombination yielding permanent expression of up to three mutually exclusive fluorescent protein labels: Cerulean, mOrange, and mCherry (**Fig. 4.3g**). At 8wks of age, we observed clones of labeled Mac^{AIRs} in the aortic arch (**Fig. 4.3h**), confirming Mac^{AIRs} self-expand *in situ* after seeding the aorta immediately post-birth. We also examined Mac^{AIRs} levels in chemokine receptor *2*-deficient (*CCR2*-/-) mice, where Ly6C^{hi} (classical) monocyte emigration from the bone marrow is

defective [29]. Compared to control mice, we found no difference in the proportion and number of intimal CD11c+CD45+ (Mac^{AIRs}) cells in the aortae of either young (P7) or adult (8wk) mice (**Fig. 4.3i,j**). This further solidifies the notion that postnatal aortic intimal macrophages self-expand and maintain their population independently of circulating monocytes at steady-state (**Fig. 4.3k**).

Assessment as to whether Mac^{AIRs} were derived from primitive or definitive hematopoiesis lineages was determined through experiments with a defined lineage tracing model (*Flt3*^{cre};*R26*^{mTmG}) that labels cells arising from definitive hematopoietic stem cells as GFP+ [27,30,31] (**Supplementary Fig. 4.6m**). P5 aortae from *Flt3*^{cre};*R26*^{mTmG} mice showed that a large proportion of intimal CD45+ cells were GFP+ relative to circulating $CD11b^{hi}Gr1^{lo}$ monocytes (**Supplementary Fig. 4.6n,o**). The recombination labeling, combined with the observation that these macrophages were not detected until after birth, strongly indicates that these cells were derived from definitive hematopoiesis lineage and not from the yolk sac, as is known to occur for some resident macrophage populations [27,28].

Mac^{AIRs} blunt thrombin activity in areas of oscillatory flow

An inducible diphtheria toxin model (*Cx3cr1*^{creERT2};*CSF1R*-flox-stop-flox-DTR) whereby dual tamoxifen and diphtheria toxin (DTx) injections result in elimination of cells expressing both Cx3cr1 and CSF1R was used to deplete Mac^{AIRs} and clarify their biological relevance (**Fig. 4.4a**). Efficient loss of macrophages was noted 24hrs post-DTx injection (**Fig. 4.4b**) and was associated with altered endothelial morphology and apparent reduction of cell size (**Fig. 4.4c, Supplementary Fig. 4.7a**). To clarify whether this was related to actual endothelial contraction, we evaluated the expression of phospho-myosin light chain 2 (pMLC2). In control mice, Mac^{AIRs} showed high expression of pMLC2 (**Fig. 4.4d, Supplementary Fig. 4.7b**). Upon macrophage depletion, endothelial cells became positive for pMCL2 indicating a highly contractile functional state, likely the reason behind the drastic change in cell size (**Fig. 4.4c-d, Supplementary Fig. 4.7b**). Together, these findings suggested that Mac^{AIRs} prevented a contractile phenotype in the

endothelium which would otherwise manifest in areas of oscillatory/disturb flow through an unclear mechanism.

It is well-known, that exposure of cultured endothelial cells to thrombin, results in rapid Rho activation, phosphorylation of MLC2, stress fiber formation, contraction, and disruption of endothelial junctions [32,33] (**Supplementary Fig. 4.7c**). All of these events are triggered downstream signaling by GPCR protease-activated receptor 1 (PAR1), a receptor highly expressed by aortic endothelial cells (**Supplementary Fig. 4.7d**), and activated upon cleavage by thrombin [32,33]. Interestingly, plasmin and other proteases, including MMP12 and 13 both highly expressed by Mac^{AIRs} (**Figure 4.4e**), can alter this signaling pathway by cleaving PAR receptors that are carboxyl-terminal to the thrombin cleavage site and thus, prevent thrombin-mediated endothelial contraction [34–37]. Consequently, we posit that in absence of Mac^{AIRs}, intact endothelial PAR1 was available to be activated by thrombin leading to endothelial contraction. This assumption implied accumulation of thrombin in areas of oscillatory/disturbed flow. Indeed, staining for thrombin revealed presence of thrombin at the lesser curvature of the aortic arch and branch openings (**Fig. 4.4f).** Additionally, to further confirm the thrombin activity in regions of disturbed flow, we treated control or *Cx3cr1*^{creERT2};*CSF1R*^{flfDTR} mice with Vehicle or Dabigatran (thrombin-specific inhibitor) and assessed endothelial cell contraction (**Fig. 4.4g**). Five days post-treatment, dabigatran-control mice still expressed pMLC2 in Mac^{AIRs}, indicating that macrophage contraction was thrombin-independent (**Fig. 4.4h**). However, depletion of macrophages with concurrent dabigatran treatment prevented endothelial cell contraction, as per pMLC2 expression and cell size quantification (**Fig. 4.4h,i**), demonstrating that endothelial cell contraction was thrombin-dependent, but mitigated when Mac^{AIRs} were present. Thrombin was still present in areas of oscillatory flow after macrophage depletion (**Supplementary Fig. 4.7e**). Together, these findings indicate Mac^{AIRs} prevent endothelial contraction driven by thrombin in regions of oscillatory flow. Importantly, we tested other aspects of clotting in the presence and absence of macrophages, including tail bleed times (**Supplementary Fig. 4.7f**); as well as other mediators /

regulators of the clotting such as nitric oxide and prostacyclin (**Supplementary Fig. 4.7g,h**). None of these were altered by deletion of macrophages.

The next critical question was to sort out the molecular mechanism whereby macrophages impaired thrombin action, and in particular pMLC2, in endothelial cells. It is well accepted that thrombin mediates signals on endothelial cells through protease activated receptors (PAR1, 2 and 4) [32,33], all expressed by aortic endothelial cells, but not by Mac^{AIRs} (**Supplementary Fig. 4.7d**). Interestingly PAR receptors can be cleaved by thrombin, mediating signaling, but also by other proteases like Mmp12 and Mmp13 blunting these signals by cleaving PAR1 upstream the thrombin site[34–37]. Considering the high levels of Mmp12 and 13 expressed by Mac^{AIRs} it was only logical to fill the dots and predict that matrix metalloproteases secreted by Mac^{AIRs} impaired thrombin-mediated contraction in endothelial cells. While testing this hypothesis in mouse aorta was impossible, we evaluated thrombin signaling, as per pMLC2 levels on endothelial cells in the presence and absence of Mmp13 (**Figure 4.4j**). The findings, presented in Figure 4j clearly shows that thrombin activates pMLC2 in the endothelium and that this effect is impaired by co-incubation with Mmp13.

Mac^{AIRs} residency coincides with deposition of fibrin(ogen)

The presence of thrombin in areas of disturbed flow led us to inquire whether fibrinogen, a substrate of thrombin, was also found in these regions. Indeed, *en face* staining for fibrin(ogen) in the arch of 8wk old C57BL/6 mice revealed the buildup of fibrin(ogen) in the lesser curvature (**Fig. 4.5a**). Higher magnification images (**Fig. 4.5b**) and 3D surface rendering (**Fig. 4.5c**) also revealed that fibrin(ogen) decorated the surface of Mac^{AIRs}. To further confirm that fibrin(ogen) is deposited in regions of disturbed flow, we depleted endogenous fibrinogen *in vivo* and then treated those mice with fluorescently tagged fibrinogen to assess binding sites and accumulation (**Fig. 4.5d**). Knock-down of fibrinogen was accomplished by delivery of siRNA targeting hepatic fibrinogen mRNA (siFibrinogen), which was encapsulated in lipid nanoparticles containing an ionizable cationic lipid [38]. At 7d post-treatment circulating fibrinogen was ~90% depleted (**Fig.**

4.5e) and at this time, fibrinogen-a488 (fbg-a488) 3-hours post-injection bound avidly to Mac^{AIRs} and accumulated throughout lesser curvature (**Fig. 4.5f)**. In contrast, Fbg-a488 did not accumulate in the greater curvature (**Supplementary Fig. 4.8a**), confirming the predilection of fibrinogen accumulation in regions of disturbed flow.

We validated concurrent associations of Mac^{AIRs} and fibrin(ogen) in intercostal artery openings (**Fig. 4.5g**). The correlation was also noted in 78wk old descending aortae (**Supplementary Fig. 4.8b**). Moreover, a time course evaluation showed progressive fibrin(ogen) accumulation in the aortic arch of P7, 3wk, and 8wk mice coinciding with the expansion of Mac^{AIRs} with age (**Supplementary Fig. 4.8c**). As fibrinogen is a substrate for macrophages, we predicted that fibrinogen deposits might be required for seeding of Mac^{AIRs} in the regions of disturbed flow in the tunica intima. Thus, we analyzed Mac^{AIR} accumulation in fibrinogen-deficient mice (*Fbg*$^{-/-}$) [39] and in mice expressing a mutant form of fibrinogen that could not be converted to fibrin polymer (*Fbg*^{AEK}) [40]. Our prediction was incorrect as no difference in the abundance or distribution of Mac^{AIRs} was found in either mouse model (**Fig. 4.5h**). These findings reconcile that while overlapping in location, fibrin(ogen) was dispensable for the seeding or anchoring Mac^{AIRs} to the tunica intima.

Mac^{AIRs} are necessary to clear fibrin(ogen) deposits in regions of disturbed flow

The concurrent presence of both thrombin and fibrin(ogen) in areas of disturbed flow implied that Mac^{AIRs} might be involved in preventing fibrin formation; therefore, we explored fibrin(ogen) accumulation in the *Cx3cr1*^{creERT2};*CSF1R*^{flfDTR} model over time (**Fig. 4.6a**). Evaluation of fibrin(ogen) levels at 7- and 14-days post-continued depletion revealed progressive and significant accumulation in the lesser curvature (**Fig. 4.6b-d, Supplementary Fig. 4.8d**). Additionally, fibrin fibrils were clearly visible in the 14-day macrophage-depleted aortae (**Fig. 4.6c**), which were never detected in control mice. The data implies that Mac^{AIRs} promote clearance of fibrin(ogen) and/or prevention of fibrin formation. Further, *en face* aortae SEM images (**Fig**

4.6e, Supplementary Fig. 4.8e) revealed microthrombi and polymerized fibrin decorating the lesser curvature of *Cx3cr1*^{creERT2};*CSF1R*^{flfDTR} mice but not in littermate controls. Microthrombi were also noted by confocal microscopy along with rupture of the endothelial lining (**Fig. 4.6f,g**). As a direct read-out of disseminated microthrombi, we evaluated D-dimer and found markedly elevated levels in macrophage-depleted mice compared to undetectable levels in control mice (**Fig. 4.6h**), further supporting hemostatic imbalance. Histological examination of tissues from Mac^{AIR} depleted mice revealed hemorrhagic foci in multiple tissues, including kidney, liver, and lung (**Fig. 4.6i**). Images of the kidneys from *Cx3cr1*^{creERT2}; *CSF1R*^{flfDTR} mice that had to be euthanized due to health decline exhibited diffused and abundant fibrin(ogen) throughout the tissue (**Fig. 4.6j**), consistent with vascular rupture. Based on the data presented, it is likely that dislodged microthrombi traveling through the circulation were responsible for occluding smaller diameter vessels leading to hemorrhagic foci and organ damage. Additional support to the requirement of Mac^{AIRs} in clearing fibrin(ogen) deposits, also emerged from evaluation of CD11c-/- mice. Absence of CD11c results in a significant reduction in the number of Mac^{AIRs}, indicating that that CD11c was necessary, albeit not fully sufficient for anchorage of Mac^{AIRs} to the intimal niche as could still detect some macrophages (approximately 45% in comparison to controls) in the tunica intima of this mouse. Importantly, this mouse model also exhibited an impressive accumulation of fibrin(ogen) (**Supplementary Fig. 4.8f**). An alternative explanation for fibrin(ogen) accumulation and thrombosis upon Mac^{AIRs} depletion could relate to break of barrier integrity in areas of oscillatory flow; implicating Mac^{AIRs} in the maintenance of endothelial junctional integrity in those areas. We tested this possibility by examining fluorescent microspheres (40nm) deposition in the tunica intima of littermate control and *Cx3cr1*^{creERT2};*CSF1R*^{flfDTR} mice that both received tamoxifen and diphtheria toxin injections (1-day post-Mac^{AIR} depletion) (**Supplementary Fig. 4.8g**). While the positive control (buffered EDTA intracardiac injection for (5min)) resulted in robust deposition of fluorescent beads in between cells, no accumulation fluorescent beads was found in any of the other groups (**Supplementary Fig. 4.8g**). Thus, Mac^{AIRs} do not play a role in maintaining barrier

integrity, instead appear to necessary to clear fibrin(ogen) deposits and mitigate PAR1-thrombin signaling in regions of disturbed flow.

The drastic phenotype observed from depletion of Mac^{AIRs} , a relatively small cell population, prompted the question as to whether the experimental approach might alter a broader group of macrophages. Thus, we evaluated alterations in the macrophage populations of multiple organs by FACs analysis (**Fig. 4.6k**). The findings revealed that while bone marrow and peripheral blood were affected by the dosage of tamoxifen/diphtheria toxin used, none of the other Cx3cr1+Csf1r+ macrophage populations were altered. The implication is that areas of oscillatory/disturbed flow in the arterial tree are sites of fibrin accumulation that absolutely depends on Mac^{AIRs} for clearance with critical consequences. A few last important pieces of evidence to solidify this conclusion were still pending, including how do Mac^{AIRs} degrade fibrin(ogen)?

Macrophages have been known to express plasminogen receptors to degrade fibrin(ogen) extracellularly[41]. Importantly, Mac^{AIRs} expressed plasminogen receptors (**Fig. 4.6l**) and bound to fluorescently conjugated plasminogen when intravenously injected (**Fig. 4.6m**). Thus, in addition to MMP12 and 13, Mac^{AIRs} are capable of generating cell surface-associated plasmin particularly with the aid of endothelial cells, which express high levels of tissue-type plasminogen activator (**Supplementary Fig. 4.8h,i**). We also confirmed that neither endothelial cells nor Mac^{AIRs} expressed plasminogen (**Supplementary Fig. 4.8j**). Taken together, our findings indicate that Mac^{AIRs} are required to clear fibrin(ogen) deposits, prevent fibrin formation and maintain an anti-thrombotic state in areas of disturbed flow.

Additional support to the conclusion that Mac^{AIRs} are responsible for clearing fibrin(ogen) deposits in regions of disturbed flow came from experiments whereby Mac^{AIRs} were allowed to return after a 2 week depletion. Much like resident macrophages in other organs[27,28,42–44], we found that upon removal of Mac^{AIRs} and elimination of depletion pressure (tamoxifen and diphtheria toxin), monocytes seed areas of disturbed flow and reconstitute the Mac^{AIR} population

(**Figure 4.7a-d**). A gradual increase of macrophage number was demonstrated after evaluation of the aorta of mice at 1wk and 2wk post-depletion (**Figure 4.7d**). Importantly, increase of Mac^{AIR} was associated with reduction of the accumulated fibrin(ogen) (**Fig. 4.7c,e**). Moreover, circulating D-dimer levels (**Fig. 4.7f**) and endothelial cell size in the lesser curvature of the aorta (**Fig. 4.7g**) also returned to control levels. Overall, these findings further support the conclusion that Mac^{AIRs} are required clear fibrin(ogen) deposits in regions of oscillatory and disturbed flow.

DISCUSSION

Vascular endothelial and hematopoietic cells are well-known to coordinate inflammatory responses. Here, we have expanded these functions to also include regulation of intravascular hemostasis. Indeed, our findings indicate that while endothelial cells provide a non-thrombogenic surface facilitating blood circulation, in areas of oscillatory or disturbed flow, this function is challenged by the accumulation of fibrinogen and thrombin (aortic arch and branches with rapid flow). In these regions, the presence of a population of intima resident macrophages (Mac^{AIRs}), summoned to areas of disturbed flow from birth, is critical to effectively clear fibrinogen and prevent intravascular clotting.

Macrophage association with the endothelium is not necessarily surprising, and when seen in aortic tissue sections, the assumption is that this heterotypic interaction might be part of an inflammatory or pre-atherosclerotic lesion. However, the unusual feature that captured our attention was the highly reproducible seeding of this macrophage population post-birth and their unique topology in relation to the endothelium. These elements indicated that seeding of these macrophages in the luminal aspect of the aorta was not part of an inflammatory response; instead, the process was a normal developmental program by which Mac^{AIRs} become a constitutive component of the tunica intima in regions of oscillatory and disturbed flow. While the work presented here addressed multiple points related to origin, lineage, and self-renewal, why are these cells attracted to areas of disturbed and oscillatory flow; how and why do they migrate from

the closing ductus arteriosus to those regions are important questions that remain unanswered. A logical assumption is that disturbed flow alters the endothelium creating unique niche conditions that attract monocytes to those sites and promote Mac^{AIRs} differentiation into a stable population capable of self-renewal. While the characterization of the endothelial niche remains unclear, we predict that thrombin is likely a requirement, as per the presence of this enzyme in regions of oscillatory and disturbed flow.

The ability of macrophages to cleave fibrinogen and participate in the remodeling of the provisional matrix formed during wound healing has been established long ago[45]. This being said, the repertoire of proteases is distinct in different macrophage subtypes, some proteases being expressed only upon induction and in situations of wound healing. We found that unlike adventitial and other macrophage populations, Mac^{AIRs} constitutively express MMP12 and MMP13, known to cleave fibrinogen[46–48]. In addition, Mac^{AIRs} also bind to plasminogen and this anchorage enables endothelial tPA to generate plasmin, which also degrades fibrinogen and fibrin. Together, this repertoire of proteases enables intravascular macrophages to efficiently remove fibrinogen deposits and antagonize fibrin accumulation driven by procoagulant pathways and the presence of thrombin in areas of oscillatory/disturbed flow. Furthermore, MMP-12 and -13 also cleave the protease activating receptor-1 (PAR-1) preventing its activation by thrombin[34–37]. Highly expressed by endothelial cells, PAR-1 promotes Rho activation downstream of thrombin, in turn; this leads to endothelial contraction and tension on inter-endothelial junctions, which might rupture in response to this challenge [32,33]. In this manner, Mac^{AIRs} protect the integrity of the tunica intima by seizing PAR-1 cleavage, interrupting thrombin-mediated activation and preventing exposure of the underlying and highly pro-thrombotic matrix. In addition, we found that Mac^{AIRs} identified and phagocytosed endothelial cells undergoing apoptosis (as per expression of annexin) further implying a cell scavenger function of Mac^{AIRs} to promote vascular health.

Supporting the biological role attributed to these macrophages, it is pertinent to remember that while compatible with development and reproduction, plasminogen deficiency results in a

severe thrombotic phenotype in both normal and inflamed tissues of adult animals [39,49,50]. Homozygous plasminogen deficient mice display spontaneous thrombotic lesions in multiple organs and a median survival of 176 days with about 40% of the mice succumbing to death. Additionally, these death phenotypes are effectively reversed by the simultaneous imposition of fibrinogen deficiency [39]. These findings underlie a critical constitutive function of the plasminogen activation system for fibrin surveillance and clearance in non-pathological settings and resonate extremely well with the findings described here.

Given the association of Mac^{AIRs} with areas of disturbed flow, also known to be pro-atherogenic sites, their potential contribution to atherosclerotic lesions is an important question. Specifically, one could predict that Mac^{AIRs} are particularly poised to be the progenitors of foam cells. This question was the focus of an elegant study recently published [15]. The authors found that while Mac^{AIRs} can uptake lipids, elimination of these cells only delays slightly, but does not alter the burden of atherosclerotic lesions, nor does it change the accumulation of foam cells in the lesions. Altogether, the conclusions of that study indicate that while participating in the process, it is the influx of circulating monocytes into the neointima that is the main source of foam cells. In context, these data together with the fact that Mac^{AIRs} embed the tunica intima immediately post-birth, are in agreement with the notion that the presence of these macrophages is not a response to a pathological insult.

The present report adjoints to the long list of studies that have recently identified self-renewing tissue-resident macrophages in multiple organs [21,22,28,51–54], now adding the aortic endothelium to this list. These tissue-resident macrophages were found to seed multiple organs either during embryonic development or shortly thereafter, and are derived from either yolk sac erythroid-myeloid or circulating myeloid progenitors [27,28]. Tissue-resident macrophages from distinct organs are found to have unique transcriptional identities and functions and are programmed by an organ-specific niche. As discussed, we attribute endothelial cells conditioned by disturbed flow the niche for Mac^{AIRs} differentiation. Importantly the well accepted pro-

inflammatory profile initially unique to the endothelium in areas of disturbed flow is also acquired by aging endothelium. By comparing Mac^{AIRs} from different anatomical regions of aortae in young vs old mice and showing that these macrophages are transcriptionally identical, our results provide evidence that changes in the endothelial cell niche are responsible for the underlying tissue-specific imprinting of these macrophages. The relevance of the microenvironment in promoting a niche cannot be overstated. For example, Kuffer cells (resident macrophages in the liver) are embryonically derived and self-maintained throughout adulthood. However, if depleted using diphtheria toxin models, bone marrow derived monocytes are capable of yielding monocyte-derived Kuffer cells that are genetically and functionally comparable to the embryonic-derived cells [42–44]. Along these lines, we find that in the absence of constant pressure to eliminate Mac^{AIRs} using diphtheria toxin, monocytes have the ability to quickly repopulate these same sites and differentiate into Mac^{AIRs}.

The findings presented here shift several paradigms. First, they challenge the concept that associations between endothelium with leukocytes are always transient and triggered by acute inflammatory events. In fact, our results highlight a long-term partnership between endothelial cells and macrophages that is not dependent on immune responses, instead it is triggered by the drastic hemodynamic changes associated with birth. Second, they change the view that a homotypic endothelial layer forms the luminal side of vessels; which now needs to be amended to include macrophages in areas of disturbed flow and aged arteries. Lastly, our findings indicate that intravascular clotting in arteries is constantly antagonized in regions of disturbed flow and "aged" endothelium. While the non-thrombogenic function of vessels was attributed exclusively to the endothelium, the data presented here provides clear evidence that in some regions of the vascular tree this can only be accomplished with aid of macrophages. The relevance of this endothelial-macrophage partnership cannot be overstated as per the devastating intravascular clotting sequelae associated with some conditions including COVID19.

ACKNOWLEDGEMENTS

We are grateful to Gwedalyn Randolph and Jesse Williams for the extensive discussions about intima resident macrophages and for the generous transfer of the Cx3cr1^{creERT};CSF1R^{lslDTR} transgenic mouse. We are also thankful to William Mueller for Pecam1 antibodies. We are thankful to Karen Ridge for the generous transfer of the Vimentin-/- mice. We also would like to thank the Broad Stem Cell Research Center (BSCRC) and Jonsson Comprehensive Center (JCC) at UCLA for sequencing of scRNAseq libraries; the BSCRC flow core at UCLA and the Robert H. Lurie Comprehensive Cancer Center (RHLCCC) flow core at Northwestern University (NU), Feinberg School of Medicine; the Mouse Histology and Phenotyping core at NU; and the Center for Advanced Microscopy at NU.A special thanks to Michelle Steel and Snezana Mirkov for managing animal colonies and for assistance with husbandry and animal experiments. Additionally, thank you to Samuel Buchanan for help with cell size quantifications. We would also like to thank Farida V. Korobova from the Center for Advanced Microscopy at NU for support with the Scanning Electron Microscopy. We thank the members of the Arispe lab and the Feinberg Cardiovascular and Renal Research Institute at Northwestern University for extensive discussions. Illustrations were created with BioRender.com.

SOURCES OF FUNDING

This work was supported by R35HL140014 to M.L. Iruela-Arispe and Howard Hughes Medical Institute Gilliam Fellowship (GT11560) to Gloria Hernandez. DAL is supported by NIH/NICHD training grant T32HD007491.

CONTRIBUTIONS

GEH performed and designed experiments, wrote and edited the manuscript

GM, **NBF, JS** and **DAL** performed experiments and quantification

LJJ, JL, and **CJK** provided siRNA-nanoparticles

PZ performed the parabiosis experiments supervised by **RA**.

RA provided transgenic mice and provided intellectual input and discussion

AEB and **MF** provided key transgenic mice and provided intellectual input to experimental design and analysis.

MP provided intellectual input on experiments using single cell RNAseq data

FM performed bioinformatic analysis of scRNAseq data

MLIA conceived the study, designed the experiments, wrote and edited the manuscript

All authors discussed the results and had the opportunity to comment on the manuscript.

DECLARATION OF INTERESTS

CJK is a director and shareholder of NanoVation Therapeutics Inc., which is commercializing RNA-based therapies. All other authors declare no competing interests.

METHODS

Data and Code Availability

All data generated or analyzed during this study are included in the Article and its Supplementary Information. The scRNA-seq data were deposited in the GEO database, accession number GSE161787.

Mice

All animal procedures were approved and performed in accordance with the UCLA and Northwestern University Institutional Animal Care and Use Committee. All other mouse information can be found in the **Supplementary Table 4.9**. All mouse strains were maintained on a C57BL/6J background, with the exception of CSF1R-merCremer mice, which was maintained on a mix background (FVB:C57BL/6). Mice were genotyped by Transnetxy. Males and females were used in approximately equal numbers for all experiments with the exception of scRNA-seq

experiments. For scRNA-seq experiments, only male C57BL/6 mice were used to minimize sex/strain differences at the transcriptional level for the arch (8wk) and aged descending (78wk) A,B data sets. Unless specified, all adult mice used were 8-10wks of age.

Aorta *en face* harvest

Adult mice were injected intra-peritoneally with 10mg of methacholine to promote smooth muscle cell relaxation to facilitate *en face* imaging. Immediately after injection, adult mice were sacrificed and perfused with 10mLs of 2% paraformaldehyde (PFA) through the left ventricle (for embryos and neonates, 0.5-3mLs of 2% PFA was used). Following perfusion, the aortae were removed and the adventitia carefully dissected under a microscope. Aortae were opened longitudinally, transferred to a 35mm silicon-coated dish filled with 2% PFA and pinned to lay flat, exposing the endothelium. Fixation proceeded for one additional hour at 4^{o}C followed by washes in phosphate buffered saline (PBS).

Aortic *en face* immunostaining

For immunostaining, tissue was washed 3 times with 1X HBSS and then incubated in blocking/permeabilization buffer (0.3% Triton-X, 0.5% Tween-20, 3% Normal Donkey Serum) for 1hr at room temperature. Primary antibody cocktail was prepared in the blocking/permeabilization buffer and incubated overnight at 4^{o}C (endothelial marker ERG, VE-cadherin, or Pecam1 were always used in conjunction with other markers in order to label the endothelium). The following day aortae were washed three times with 1X HBSS and incubated with secondary antibodies with DAPI for 1hr at room temperature. After final set of washes in 1X HBSS, aortas were mounted on glass slides with prolong gold without DAPI (Thermo,# P36930). For list of antibodies and dilutions used, see **Supplementary Table 4.9.** Stained aortae were mounded on glass slides with lumen facing the coverslip. Aortae were imaged using either an LSM880 confocal microscope (ZEISS) or an A1R HD25 confocal microscope (Nikon). Z-stack and tile scan features were used to image

the large, wavy surfaces of the aortae. The resulting tiles were then stitched into a single large image (ZEN 2.0 Black software, ZEISS or NIS-Elements, Nikon), which enabled the visualization of the large aortic arch with high resolution. Imaris software (Imaris 9.5.1 and 9.7.0 Bitplane) was used to visualize images in 3D. For list of software used for analysis, see **Supplementary Table 4.9**. Additionally, Denoise.AI (Nikon) was employed to remove Poisson shot noise in certain images. Images were acquired using either 20x,63x, or 100x objectives.

***In vivo* labeling**

Mice (C57BL/6) of 8wks of age were injected via tail vein with either rat anti-msCD45 antibody or non-blocking Pecam1 (390)-daylight 650 antibody diluted in sterile PBS to label the lumen facing surfaces of Mac^{AIRs}. Mice were sacrificed 15min (for Pecam) and 30mins (for CD45) after injection and aortae were fixed, harvested, and stained with additional, antibodies. For *in vivo* labeling of CD45: additional mouse anti-mouse CD45-biotin / streptavidin-a647, Donkey anti-rat-a488, and Pecam1 (2H8)-a568. For *in vivo* labeling of Pecam1(390)-injected mice: ERG / Donkey anti-Rb-a568, and rt-CD45 / Donkey anti-Rt-a488 (**Supplementary Table 4.9**).

Immunostaining and imaging of sections

Formalin fixed, paraffin embedded specimens from kidneys were sectioned at 4um. Antigen retrieval was performed using 1X citrate buffer and then incubated in blocking/permeabilization buffer for 1hr at room temperature. Sections were then incubated with primary antibodies (**Supplementary Table 4.9**) overnight at 4^{o}C. The following day, samples were incubated with species - specific secondary antibodies for 1 hour at room temperature prior to mounting in Prolong Gold without DAPI. Samples were evaluated using an A1R HD25 confocal microscope (Nikon).

Brightfield imaging of the aortae

E18.5, P1, P3, 1wk, 3wk, and 10wk old aortae were dissected and the adventitia was removed under a dissecting microscope. Aortae were pinned onto a 35mm silicon-coated dish filled with PBS. Aortae were imaged using an ECHO-Revolve (RVL-100-G).

scRNA-seq

Isolation of intima cells was as previously described[20]. In summary, mice were anaesthetized and perfused with 10mLs versene buffer through the left ventricle. The adventitia was removed and aorta dissected and cut open in versene buffer so that it laid like a flat sheet, exposing the endothelium. After versene washes, the aortae were bathed in 1X trypsin and incubated for 2X 5min at 37^{o}C. The endothelium was then gently removed using a microscalpel (EMS#72046-30) and repeat pipetting, now with sc-HBSS (containing 0.04%BSA and 2%FBS to inactivate the trypsin and Actinomycin D at 1ug/ml to block transcription) was applied this helped in removing the cells and obtaining a single cell suspension. The procedures were done under a dissecting microscope. Cells were pelleted and then treated with 1X RBC lysis buffer (eBioscience, #00-4333-57) for 1 minute and then washed twice with 0.04%BSA. Schematics of intimal cell isolation is shown in Figure S2A. To obtain enough cells, 6 (aged descending) or 8 (arch) C57BL/6 mice were used per library.

To isolate adventitia cells into single-cell suspension, mice were anaesthetized and perfused with 10mLs of DMEM. The adventitia was dissected from aortae and dissociated using the Miltenyi adipose tissue dissociation kit (#130-105-808). Following Milteny protocol, the single-cell suspension was additionally treated with 1X RBC lysis buffer (eBioscience, #00-4333-57) and 1U DNase. Final cell suspension was washed multiple times and resuspended in 0.04%BSA. A total of six male C57BL/6 mice (78wk old) were used to generate the library.

scRNA-seq libraries were generated using 10X Genomics Chromium Single Cell 3' Library & Gel Bead Kit v2. Cells were loaded accordingly following the 10X Genomics protocol with an estimated targeted cell recovery of 5000 cells. Sequencing was performed on Illumina HiSeq4000

(Pair-end, 100 base pairs per read, 8wk arch & aged descending A,B). The digital expression matrix was generated by demultiplexing, barcode processing, and gene unique molecular index counting using the Cellranger count pipeline (version 4.0.0, 10X Genomics). Multiple samples were merged using the Cellranger aggr pipeline. To identify different cell types and find signature genes for each cell type, the R package Seurat (version 3.1.2) was used. Cells that expressed <100 genes or <500 transcripts were filtered out. Variable genes were selected using the FindVariableGenes function for further analysis. The data were normalized using the NormalizeData function with a scale factor 10,000. The genes were then scaled and centered using the ScaleData function. Principal component analysis (PCA) and *t*-distributed stochastic neighbor embedding (t-SNE) were used to reduce the dimensionality of the data. The cluster marker genes were found using the FindAllMarkers function. Cell types were annotated based on the cluster marker genes. Heatmaps, violin plots and gene expression plots were generated by DoHeatmap, VlnPlot, FeaturePlot functions, respectively.

Flow Cytometry of peripheral blood

To measure reporter labeling (lineage tracing) and donor chimerism (parabiosis mice) of circulating cells, blood was collected by retro-orbitally bleeding into tubes containing FACS buffer at 4°C. Blood cells were pelleted and treated with 1X RBC lysis buffer. Additionally, cells were stained on ice with CD45-APC-Cy7 (BD, #557659) and then analyzed on a BD Fortessa.

Flow cytometry of organs**:** One-day post-diphtheria toxin injection (Mac^{AIR}-depletion), littermate control and $Cx3cr1^{creERT2}$;$CSF1R^{lslDTR}$ were euthanized and perfused with 10mL of versene to remove blood and then perfused with 10mLs of DMEM. Lung, liver, kidney, and leg bone (femur and tibia) were carefully dissected and washed in PBS. For bone marrow harvest, muscle was removed and bone was cleaned. Bone was then crushed in FACs Buffer using a motor pestle to release bone marrow cells. Bone marrow cells were then pelleted and treated with 1X RBC lysis buffer. For generation of single-cell suspension from lung, liver, and kidney, tissues were digested

using Militenyi's lung dissociation kit (#130-095-927), liver dissociation kit (#130-106-807), and multidissociation kit #2 (#130-110-203), following vendor's protocol. Cells were pelleted and treated with 1X RBC lysis buffer. Additionally, bone marrow, lung, liver, and kidney cells were stained on ice with CD45-APC-Cy7 (BD, #557659), CX3CR1-APC (BioLegend, #149008), CSF1R-BV421 (BioLegend, #135513), and Ter119-PECy7 (eBioscience, #25-5921-82) then analyzed on a BD Fortessa.

Lineage Tracing

Homozygous lox-stop-lox-tdTomato reporter mice were crossed with homozygous Cx3cr1-creERT2 mice. Tamoxifen induction of CRE activity in the resulting F1 compound heterozygotes was initiated by dissolving tamoxifen (Free base, MP Biomedicals, #0215673891) in sunflower seed oil (Sigma #S5007) and administering 0.01mg of tamoxifen via oral gavage to neonates at P1, P3, and P5. The penetration of intimal tdTomato positive CD45 positive cells in the aorta at P7 ranged from 40-62% determined by *en face* confocal imaging (Fig. 3f), thus the analysis in the 4wk adult needed to be normalized to P7 littermates. Therefore, as a baseline control, half of the litter was sacrificed and blood, as well, as the aorta were collected to determine reporter labeling efficiency. At 4wks, the remaining littermates were sacrificed and blood as well as aorta were collected to determine reporter expression.

To induce reporter expression in adult Cx3cr1-creERT2; R26-lox-stop-lox-tdTomato were administered 1mg of tamoxifen intra-peritoneal (IP) three times, every other day. The penetration of tdTomato positive intimal CD45+ cells in the aorta ranged from 97-100%. Aortae and blood were collected at 1wk-post as a baseline control for normalization purposes. The rest of the littermates were sacrificed 10-weeks post-injection to access retention of reporter expression in adulthood.

For clonal tracing, Cx3cr1-creERT2; R26-Rainbow neonates were administered 0.01mg of tamoxifen via oral gavage at P1, P3, and P5 to yield permanent expression of three mutually

exclusive fluorescent protein labels: Cerulean, mOrange, and mCherry. At 8wks, mice were sacrificed and reporter labeling was assessed. Adult Cx3cr1-creERT2; R26-Rainbow were injected with one dose of 0.02mg of tamoxifen and aortae were assessed 9 months later.

***In vivo* macrophage depletion**

To deplete macrophages, adult (8-10w) Cx3cr1-creERT2;CSF1R-flox-stop-flox-DTR mice, were first injected with tamoxifen IP to promote Cre-dependent induction of the diphtheria toxin receptor (DTR). The following day, mice were injected with 200ng of diphtheria toxin (Sigma, #D0564) in sterile 1X PBS to induce apoptosis of DTR-expressing cells. This resulted in cell death of this population as quickly as 24hrs. However, since intimal, aortic myeloid cells are replenished quickly, evaluation of longer time-points required continuous injection with tamoxifen followed by diphtheria toxin every three days until the end of the experiment.

EdU incorporation assay

Mice were injected IP with EdU (5-ethynyl-2-deoxyuridine, Fisher Scientific, #A10044 at 10mM). Two hours post-injection, mice were terminally anesthetized and perfused with 2%PFA via the left ventricle. The aorta was removed and the adventitia dissected away. The aorta was longitudinally cut and pinned so that the endothelium was exposed. Following fixation, EdU was revealed using a647 following manufacture's protocol (Invitrogen #C10640). Additionally, aortae were stained for nuclear endothelial marker ERG, pan-hematopoietic marker CD45, and DAPI before being imaged.

Scanning Election Microscopy

To determine the location of macrophages in relation to the endothelium, mice were anesthetized and perfused with 10mLs of 2% PFA through the left ventricle. Aortae were first immunostained *en face* following the protocol listed above. High- and low-resolution images were then obtained

by confocal microscopy. After imaging, the aortae were washed in 1X HBSS, dehydrated with increasing concentrations of ethanol, and subjected to critical point drying followed by gold/palladium coating using a sputter coater. High- and low-resolution SEM images were also taken in order to utilize landmarks and find macrophages identified with the confocal images. Confocal images and SEM images were then overlaid together using Adobe Photoshop.

To image microclots in macrophage-depleted ($Cx3cr1^{creERT2}$;$CSF1R^{lslDTR}$) and control aortae, mice were perfused with 4% Glutaraldehyde through the left ventricle. Aortae were dissected and treated for an additional 1hr in 4% Glutaraldehyde at room temperature and then washed several times with 1X PBS. Aortae were then incubated in 1% osmium tetroxide for 1hr, dehydrated in a series of ethanol, dried in critical point mounted on pins, and coated with 10nm gold for SEM. Aortae were then imaged using JEOL NeoScope at 10kV or15kV.

Dabigatran treatment

Mice were injected 2X a day (morning and night) intraperitoneal with 300ug of Dabigatran (BIBR 953, Selleck #S2196) per injection for 5 days. Dosage was determined by clotting test. After 5-days of treatment, mice were sacrificed and aortae were analyzed.

***In vivo* siFibrinogen knock-down**

8wk C57BL/6 mice were weighed and then injected with either siFibrinogen or siRNA targeting Luciferase (siLuciferase, control) at 1mg siRNA per kg body weight via tail vein injection. siFibrinogen and siLuciferase were each encapsulated in lipid nanoparticles, composed of an ionizable lipid (DLin-MC3-DMA), phosphatidylcholine, cholesterol, and a poly-ethylene glycol lipid, using methods previously described [55]. To determine knock-down efficiency, we quantified fibrinogen protein levels in plasma 7-days post-injection. In short, we collected peripheral blood in EDTA-coated tubes (BD #365974) and isolated plasma via centrifugation. Plasma was diluted (1:50) and fibrinogen was measured using a Mouse Fibrinogen ELISA kit (Abcam #ab213478).

Intravenous administration of Fibrinogen-a488 or Plasminogen-FITC

Mice were injected intravenously with 400ug of Fibrinogen-a488 (Thermo #F13191), plasminogen-FITC (Abcam #ab92770), or Albumin-FITC (control, Thermo #A23015). Fibrinogen-a488 injected mice were sacrificed 3-hrs post-injection and plasminogen-FITC injected mice were harvested 4-hrs post-injection to assess local accumulation, relative to the Mac^{AIRs}.

D-dimer measurements

Mice were anesthetized and blood was collected via right ventricle puncture with a 25G syringe. For D-dimer measurements, blood was collected in citrate buffer with a final ration of 3.2% citrate (for D-dimer). Blood was centrifuged and citrate plasma was collected and shipped to IDEXX on dry ice for quantification.

Comparison to the Tabula muris atlas and Chakarov et al. 2019

To find similar cell population in other tissues, we compared the MacAIRs to the monocytes/macrophages from the Tabula Muris Atlas. Specifically, the expression values for all the monocytes and macrophages were extracted from the Tabula Muris Atlas and merged with the expression values of the MacAIRs from our dataset. The Seurat pipeline described above was applied to cluster the cells. Since the datasets were generated by different labs, the RunHarmony function from the R package harmony[56] was applied to remove potential batch effects among different tissues. After clustering, the MacAIR marker genes were used to calculate a module score, which was used to identify the cell population from the Tabula Muris Atlas that were similar to the MacAIRs. The module score was calculated based on the average expression of the genes in the list, subtracted by the aggregated expression of randomly chosen control genes.

Monocytes and macrophages obtained in our scRNAseq datasets were also overlapped to the two macrophage populations obtained by Chakarov *et al.* [22]. For this marker genes

extracted from the comparison among the monocytes, adventitia macrophages and MacAIRs in our study were compared to the Lyve1^{lo}MHCII^{hi} and Lyve1^{hi}MHCII^{lo} from the Chakarov study. The Jaccard index between each pair for cell types from the two datasets was calculated and plotted in the heatmap.

Parabiosis

Mice of the similar weight, size, and same sex were housed together for 2 weeks prior to surgery to assess compatibility. Surgeries were done as previously [57]. In short, mice were anesthetized and matching skin incisions were made from the olecranon to the knee joint of each mouse, and the subcutaneous fascia was bluntly dissected to create ≈0.5 cm of free skin. The right olecranon of 1 animal was attached to the left olecranon of the other by a single 3-0 nylon suture and tie. The partners' knee joints were similarly connected. The dorsal and ventral skins were closed approximated by staples, and the animals were warmed with heating pads and monitored until recovery. Parabiotic pairs were housed 1 pair per cage and given acidified water (pH 2.5). After 4 weeks of anastomosis, blood samples from each animal in a parabiont pair were analyzed using flow cytometry. Animal pairs with <30% blood chimerism were excluded from our studies.

Annexin staining in aortae

Adult mice were sacrificed and perfused with 3mLs of 5% Annexin-a488 conjugate (Invitrogen, #A13201) through the left ventricle. After a couple of minutes, the aorta was carefully dissected and transferred to a 35mm silicon-coated dish filled with 20% Annexin-a488. 20% Annexin-a488 was also used to flush the Annexin inside the intact vessel and then incubated at 37^{o}C for 10min. Following incubation, the tissue was fixed in 2%PFA for one additional hour at room temperature followed by multiple washes on PBS. The aortae were then opened and pinned to lay flat,

exposing the endothelium and immunostained as described previously with ERG, CD45, and DAPI (**Supplementary Table 4.9**).

***In vitro* thrombin and MMP13 treatment and thrombin treatment with shear stress**

Human aortic endothelial cells (HAECs) were isolated as described from aortic trimmings of donor hearts at the University of California, Los Angeles (UCLA) [58]. All HAECs were de-identified and exempt from consideration as human subjects research by institutional regulatory boards at UCLA. Additional HAECs were purchased from Lonza (#CC-2535). For thrombin and MMP13 treatment, HAECs were grown on gelatin-coated, tissue culture-treated six-well plates (Falcon, #353046) to confluency in complete MCDB-131 media (VEC Technologies #MCDB131-WOFBS) plus 10% FBS (Omega-Scientific#FB-11). Once confluent, cells were washed with PBS to remove serum, then serum-free MCDB-131 was added to HAECs for overnight starvation. Next day, cells treated with Vehicle, MMP13 (1ug, Abcam #ab227435), or Thrombin (0.625U/mL,Sigma #10602400001) for 5 mins. After treatment, cells were washed in PBS with Na3OV4 and lysates were collected using mRIPA (50mM Tris, 0.1%SDS, 0.5% Na-Deoxycholate, 1%Triton-X, 150mM NaCl, 1mM Na3VO4, Protein inhibitor cocktail). Lysates were denatured in Laemmli buffer with 2-Mercaptoethanol at 95^{o}C for 10 minutes. Proteins were separated by SDS-PAGE gradient (4-20%, Bio-Rad #4561094DC) gel and transferred onto nitrocellulose membranes (Bio-rad #1704271) and incubated overnight at 4^{o}C with primary antibodies. Primary antibodies: anti-phosphorylated MLC2 (3671S), anti-MLC2 (CST #3672S), Par1 (Thermo #PA5-19102), gamma-tubulin (Abcam #ab11321). HRP-conjugated secondary antibodies (1:10,000) were applied in species dependent manner for 1hr at room temperature. Immuno-complex detection was enhanced chemiluminescence SuperSignal™ West Femto Maximum Sensitivity Substrate (ThermoFisher Scientific #34095) using ChemiDoc XRS + Molecular Imager (Bio-Rad Laboratories). Quantification of bands was performed using ImageLab Software (Bio-Rad Laboratories).

For thrombin and shear stress experiments, HAECs were grown on gelatin-coated, glass-bottom, six-well plates (Cellvis, #P06-1.5H-N) to confluency in complete MCDB-131 media plus 10% FBS. Once confluent, cells were washed with PBS to remove serum, then media containing MCDB-131 and 4% dextran (Sigma-Aldrich #31392) was added to confluent HAECs. Vehicle (PBS) or thrombin (Sigma, #10602400001) to a final concentration of 0.625 U/mL was then applied. Monolayers were subjected to unidirectional constant laminar flow for 48hrs at 130rmp horizontal circular orbit (Benchmark, #BT302). Static monolayers used the same dextran-containing media and were cultured alongside flow-treated monolayers. 48hrs-post flow, cells were fixed in 2%PFA for 15 minutes at room temperature, then washed in PBS.

For immunostaining, cells were incubated in blocking/permeabilization buffer (0.3% Triton-X, 0.5% Tween-20, 3% Normal Donkey Serum) for 1hr at room temperature. Primary antibody cocktail was prepared in the blocking/permeabilization buffer and incubated overnight at 4^{o}C. The following day aortae were washed three times with 1X PBS and incubated with secondary antibodies for 1hr at room temperature. All primary cells were cultured in humidified incubator at 37^{o}C and 5% CO_2 and used between passages 4 and 9.

Microspheres permeability

One-day post-diphtheria toxin injection (Mac^{AIR}-depletion), littermate control and Cx3cr1^{creERT2};CSF1R^{lslDTR} mice were injected in the left ventricle with 200uL of 40nm microspheres (1:10, Thermo #F8795). Beads circulated for 5 mins and then mouse was euthanized and perfused with 10mLs of PBS followed by 10mLs of 2%PFA. Aorta harvest and whole-mount staining was performed as described above. For positive control, C57BL/6 mice were injected with 50mM EDTA buffer solution in the left ventricle and allow to circulate for 5mins to challenge endothelial junctions. Then, these positive control mice were injected with microspheres and harvested as described.

Tail Bleeds

One-day post-diphtheria toxin injection (Mac^{AIR}-depletion), littermate control and $Cx3cr1^{creERT2}$;$CSF1R^{lslDTR}$ mice with same age/weight were anesthetize with ketamine/xylazine at a dose of 0.1mL/20g. Using scalpel blade #11, mice's tails were resected exactly 3mm of distal tail. Tails were quickly placed in tail bleeding buffer (10mM Tris-HCL, 2mM CaCl2, warmed to 37C), starting stopwatch. Stopwatch was stopped after blood stream halted.

***Ex vivo* Nitric Oxide (NO) measurements**

5mM stock solution of DAF-FM diacetate (Invitrogen, #D3844) was diluted to 10uM in media without phenol red (EBM, Lonza#CC-3129). One-day post-diphtheria toxin injection (Mac^{AIR}-depletion), littermate control and $Cx3cr1^{creERT2}$;$CSF1R^{lslDTR}$ mice were euthanized and perfused with 10mL of PBS followed by 3mLs of 10uM of DAF-FM diacetate. Aortae were then quickly and gently harvested in 10uM of DAF-FM. Intact aortae were then incubated in DAF-FM for 10mins at 37^{o}C. After 10mins, DAF-FM was replaced with fresh DAF-FM and incubated for an additional 15mins. Aortae were then quickly filet open and mounted with PBS. Confocal imaging occurred immediately after to measure NO production.

Quantification and statistical analysis

Treatments were randomized; investigators were blinded to allocation for outcome assessment. Quantification of intimal immune cells in aortae was done using the spots function in Imaris 9.5.1 or 9.7.0 (Bitplane) on maximum intensity Z-projections. Only cells with clearly distinguishable bodies and nuclei (DAPI, not shown) were quantified.

Cell surface area and elongation factor of endothelial cells in control and macrophage-depleted ($Cx3cr1^{creERT2}$;$CSF1R^{lslDTR}$) aortae was determined in several regions of 44.1 mm^2 within

the lesser curvature of each whole-mount, flat-mounted aortae. Measurements were done in NIS-Elements, using a combination of manual and automated cell shape identification. VE-cadherin or Pecam1 staining was used to define endothelial cell borders. Experiment included littermate controls that received both tamoxifen and DTx injections. Mean fluoresce intensity (MFI) was determined using the surface function in Imaris 9.5.1 or 9.7.0 on maximum intensity Z-projections. Subsequently, the mean for at least three independent samples and standard deviation of the determined. To assess whether two datasets were significantly different, we calculated P values with unpaired, non-parametric student's *t*-test followed by Mann-Whitney test; $P < 0.05$ was considered significant and $P < 0.05$, 0.01, 0.001 and 0.0001 were represented by *,**,***, and ****. Statistical analyses were performed with Prism 8 (GraphPad Software).

Supplementary Table 4.9. Key resources

REAGENT or RESOURCE	**SOURCE**	**IDENTIFIER**
Antibodies (concentration)		
Primary:		
VE-cadherin (1:400)	Santa Cruz	sc-6458; AB_2077955
VE-cadherin (1:100)	R&D	AF1002; AB_2077789
CD45 (1:200)	BD	#550539; AB_2174426
ERG (1:400)	Abcam	ab92513; AB_2630401
CD11c (1:200)	BD	#550283; AB_393578
CXCL16 (1:200)	R&D	AF503; AB_2230043
MMP13 (1:200)	Abcam	ab39012; AB_776416
MMP12 (1:200)	Novus	NBP2-67344
Fibrinogen (1:400)	Abcam	ab118533; AB_10900171
phospho-MLC2 (1:200 IF), (1:500 WB)	CST	#367S; AB_330248
CD45.2-biotin (1:200)	BioLegend	109804; AB_313441
CD45-biotin (1:200)	BD	#554876; AB_395569
CD68-a647 (1:200)	BioLegend	137003; AB_2044001
Thrombin (1:200)	Novus	NBP1-58268; AB_11023777

Pecam1 (2H8) (1:1000)	Laboratory of William Muller	Bogen et al. 1992; AB_2161039
Pecam1 (390) - Dylight 650 (1:100)	Laboratory of William Muller (Millipore)	CBL1337-I; AB_2283583
MLC2 (1:500)	CST	3672S; AB_10692513
Par1 (1:800)	Thermo	PA5-19102; AB_10986472
gamma-tubulin (1:1000)	Abcam	ab11321; AB_297926
CD45-APCCy7 (1:200)	BD	557659; AB_396774
Ter119-FITC (1:400)	BioLegend	116215; AB_493402
Ter119-PEcy7 (1:400)	eBioscience	25-5921-82; AB_469661
Csf1r-BV420 (1:400)	BioLegend	135513; AB_2562667
Cx3cr1-APC (1:400)	BioLegend	149008; AB_2564492
Secondary (1:400):		
Donkey anti-rabbit a488	Fisher	#A21206; AB_2535792
Donkey anti-goat a488	Invitrogen	#A11055; AB_2534102
Donkey anti-sheep a488	Fisher	#A11015; AB_2534082
Donkey anti-rabbit a568	Fisher	A10042; AB_2534017
Donkey anti-goat a568	Fisher	11057; AB_2534104
Donkey anti-rabbit a647	Invitrogen	#31573; AB_2536183
Donkey anti-goat a647	Abcam	ab150135; AB_2687955
Donkey anti-rabbit a405	Abcam	ab175649; AB_2715515
Goat anti-hamster biotin	BioLegend	405501; AB_315019
Dapi	Fisher	#D1306; AB_2629482
Goat anti-hamster a488	Jackson IR	127-545-160; AB_2338997
Goat anti-hamster a647	Jackson IR	127-605-160; AB_2339001

Streptavidin(STA)-a647	BioLegend	#405237
STA-PE	BioLegend	#405203
anti-rabbit HRP	Fisher	45-000-682, AB_772206
anti-goat HRP	Thermo	31433, AB_228390
Experimental Models: Organisms/Strains		
C57BL/6J Mice	Jackson Laboratories	IMSR_JAX:000664
C57BL/6J VE-cadherin Cre-ERT2 Mice	Soresnsen et al. 2009	Tg(Cdh5-cre/ERT2)1Rha ;MGI ID 3848982
C57BL/6J flox-stop-flox-tdTomato Mice	Jackson Laboratories	IMSR_JAX:007909
FVB:C57BL6 CSF1R-merCremer Mice	Jackson Laboratories	IMSR_JAX:019098
C57BL/6J CCR2-/- mice	Jackson Laboratories	IMSR_JAX:004999
C57BL/6J Cx3cr1-creERT2 mice	Jackson Laboratories	IMSR_JAX:020940
C57BL/6J CSF1R-flox-stop-flox-DTR	Jackson Laboratories	IMSR_JAX:024046
C57BL/6J SM22-cre	Jackson Laboratories	IMSR_JAX:004746
C57BL6/J Flt3-cre;R26-flox-Tomato-stop-flox-GFP	Laboratory of Anna Beaudin	Boyer et al. 2011[30]
C57BL6/J Fibrinogen-/- mice	Laboratory of Matthew Flick	Bugge et al. 1996[39]
C57BL6/J Fibrinogen-AEK mice	Laboratory of Matthew Flick	Prasad et al. 2015[40]
C57BL6/J CD11c-/- mice	Laboratory of Matthew Flick	

C57BL6/J R26-Rainbow mice	Laboratory of Reza Ardehali	Rinkevich et al., 2011[59]
Critical commericial assays		
Chromium Single Cell 3' Library & Gel bead Kit v2 and v3	10x Genomics	#PN-120237(v2),# PN-1000075 (v3)
Click-iT Plus EdU Cell Proliferation Kit for Imaging	Invitrogen	C10640
Mouse Fibrinogen ELISA kit	Abcam	ab213478
Experimental Models: Cell lines		
Human Aortic Endothelial Cells	UCLA	Navab, M. *et al*[58]
Software and algorithms		
Imarisx64 9.5.1 & 9.7.0	Bitplane	SCR_007370
Prism	Graphpad	SCR_002798
Seurat v2.3.4 & v3.3.3		SCR_016341
Metascape		SCR_016620
Cell Ranger	10x Genomics	SCR_017344
R for statistical computing		SCR_001905
R studio		SCR_000432
Illustrator	Adobe	SCR_010279
NIS-elements	Nikon	SCR_014329
ZEN-blue	Zeiss	SCR_013672
FlowJo		SCR_008520
Other		
Zeiss LSM880 confocal	Ziess	https://www.zeiss.com/microscopy/us/products/confocal-microscopes/lsm-880-with-airyscan-.html
A1R HD25 confocal	Nikon	https://www.microscope.healthcare.nikon.com/products/confocal-microscopes/a1hd25-a1rhd25

Chromium Controller	10x Genomics	Part# GCG-SR-1;SCR_019326
HiSeq4000	Illumina	https://support.illumina.com/sequencing/sequencing_instruments/hiseq-4000.html
NeoScope Benchtop SEM	JEOL	https://www.jeolusa.com/PRODUCTS/Scanning-Electron-Microscopes-SEM/Benchtop/NeoScope-Benchtop-SEM
Orbital shaker	Benchmark	#BT302
siRNA-fibrinogen-LNP	Laboratory of Christian Kastrup	Strilchuk et al., 2020[55]

FIGURES

Figure4.1

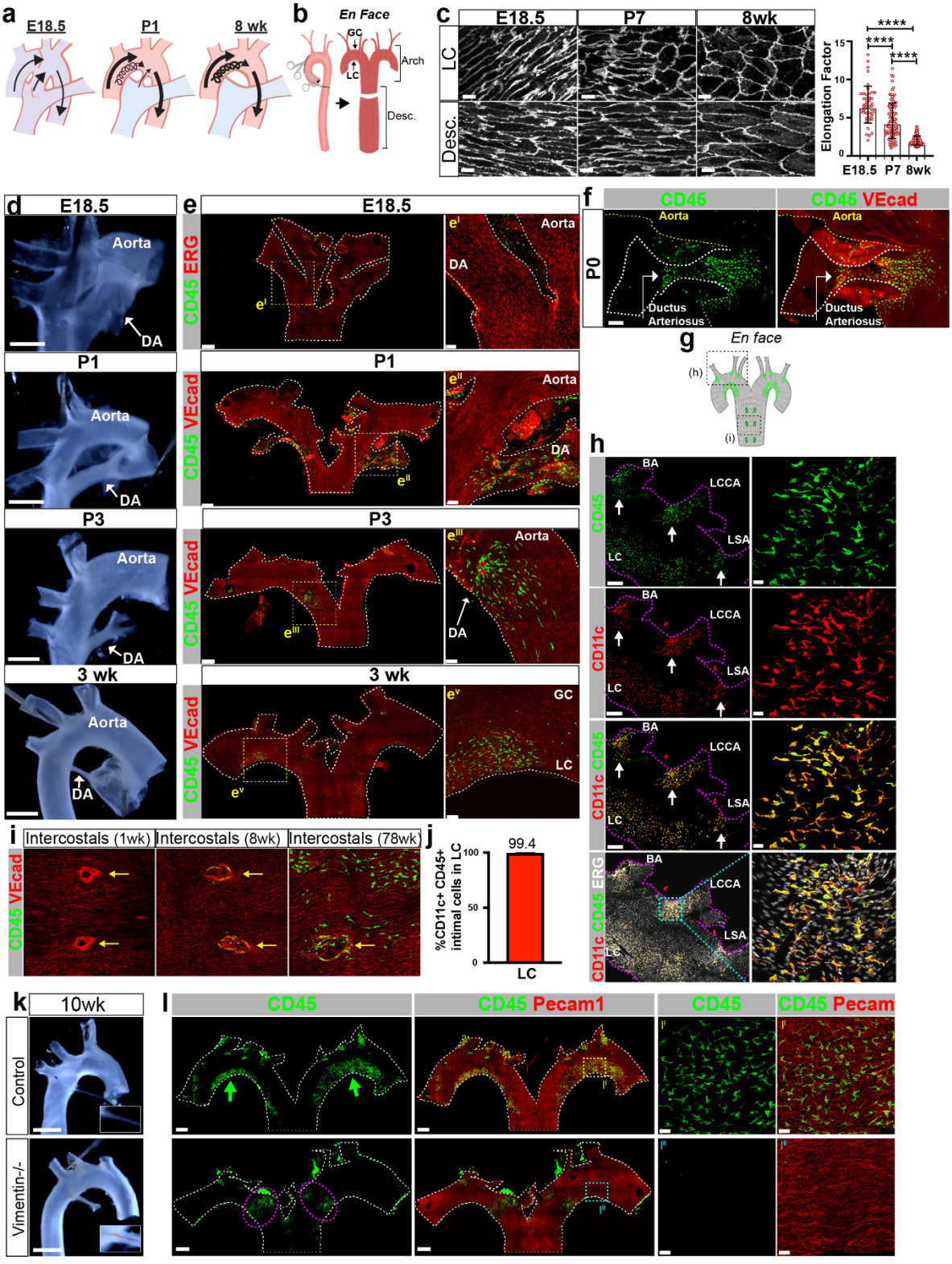

Figure 4.1. Hemodynamic changes associated with birth result in the recruitment of immune cells to the tunica intima

a, Anatomical and hemodynamic changes associated with birth. E18.5 blood from the pulmonary arteries mixes with blood from the aorta through the ductus arteriosus. P1, the ductus arteriosus constricts and this contributes to disturbed flow in the aortic arch. Shortly thereafter and in the adult (8wks), the aorta and the pulmonary artery are no longer connected. Red denotes highly levels of oxygen in the blood; while blue denotes lower oxygen in the blood; purple mixed levels of oxygen. **b,** Schema illustrating the process of aorta dissection for whole mount observation of *en face* imaging. Greater Curvature (GC), Lesser Curvature (LC), Descending aorta (Desc). **c,** Whole mount, *en face* images of the lesser curvature and of the descending aorta from E18.5, P7, and 8wk mice. Endothelial cells, through mechanosensation alter their shape in the lesser curvature from elongated to polygonal, consistent with disturbed and oscillatory flow of that region. The elongation factor in LC was calculated and shown on the adjacent graph (n=3-5, Mann-Whitney t-test, ± SD, **p ≤ 0.01, ***p≤ 0.001, ****p ≤ 0.0001, Scale bar, 10μm). **d,** Bright field images showing remodeling of the ductus arteriosus (DA) at the indicated developmental ages in C57BL/6 mice (Scale bars, E18.5-P3= 500μm and 3wk=1000μm; n=5-10 per time point). **e,** En face images show exit of immune cells from the DA and their migration to areas of disturbed flow at the indicated developmental ages. VE-Cad or ERG is shown in red. Scale bars, 300μm and 70μm (e^{I-V}), n=5-10 per time point. **f,** Lumen of DA *en face* (dotted white lines) at P0 highlighting immune cells and their migration towards the aorta. Scale bar, 50μm, n=5. **g,** Illustration of a dissected aorta highlighting regions of disturbed blood flow where intimal immune cells (green) accumulate in healthy, adult mice. Dotted black boxes indicate branch openings that are shown in the following panels (h,i). **h,** *En face* images of large branch openings in the aortic arch of adult, C57BL/6 mice. Note accumulation of intimal myeloid (CD11c+ in red and CD45+ in green) cells (white arrows) in the anterior aspects of large branch openings. Co-distribution of CD45 and CD11c markers can be seen in most of the cells. ERG is shown in white to identify endothelial nuclei. Brachiocephalic trunk (BA) Left common carotid artery (LCCA), Left subclavian artery (LSA), lesser curvature (LC) of aortic arch. Scale bar, 200μm (left column) and 20μm (right column), n=15. **i,** Time-course (1wk, 8 wk, 78wk) evaluation of intimal CD45+ cells (green) deposition in the opening of intercostal arteries (yellow arrows) of healthy, C57BL/6 mice. Note, no intimal CD45+ cells were found in 1wk old aortae. VE-Cad is shown in red. Additionally, 78wk aortae show intimal CD45+ cells residing in

laminar shear regions of the descending aorta as well. Scale bar, 50μm, n=12 (1wk), n=498 (8wk), n=6 (78wk). **j,** 99.4% of intimal CD45+ cells in the LC of the aortic arch are also labeled by CD11c+ (n=4, ± SD). **k,** Bright field images of 10wk control and Vimentin$^{-/-}$ (Vim$^{-/-}$) aortae. Higher magnification shows the remnant (control) and patent ductus arteriosus (Vim$^{-/-}$). Note blood in the lumen of the DA in the Vim$^{-/-}$. (n=8, Scale bar, 1300μm). **l,** *En face* images of the aortic arch of 10wk old control and Vim$^{-/-}$ mice, highlighting accumulation of immune cells in control (green arrows) and Vim$^{-/-}$ (dotted pink ovals). VE-Cad is shown in red. High magnification of the indicated squares is shown on the right panels (l^{I-II}). Scale bar, 500μm and 40μm (l^{I-II}).

Figure 4.2

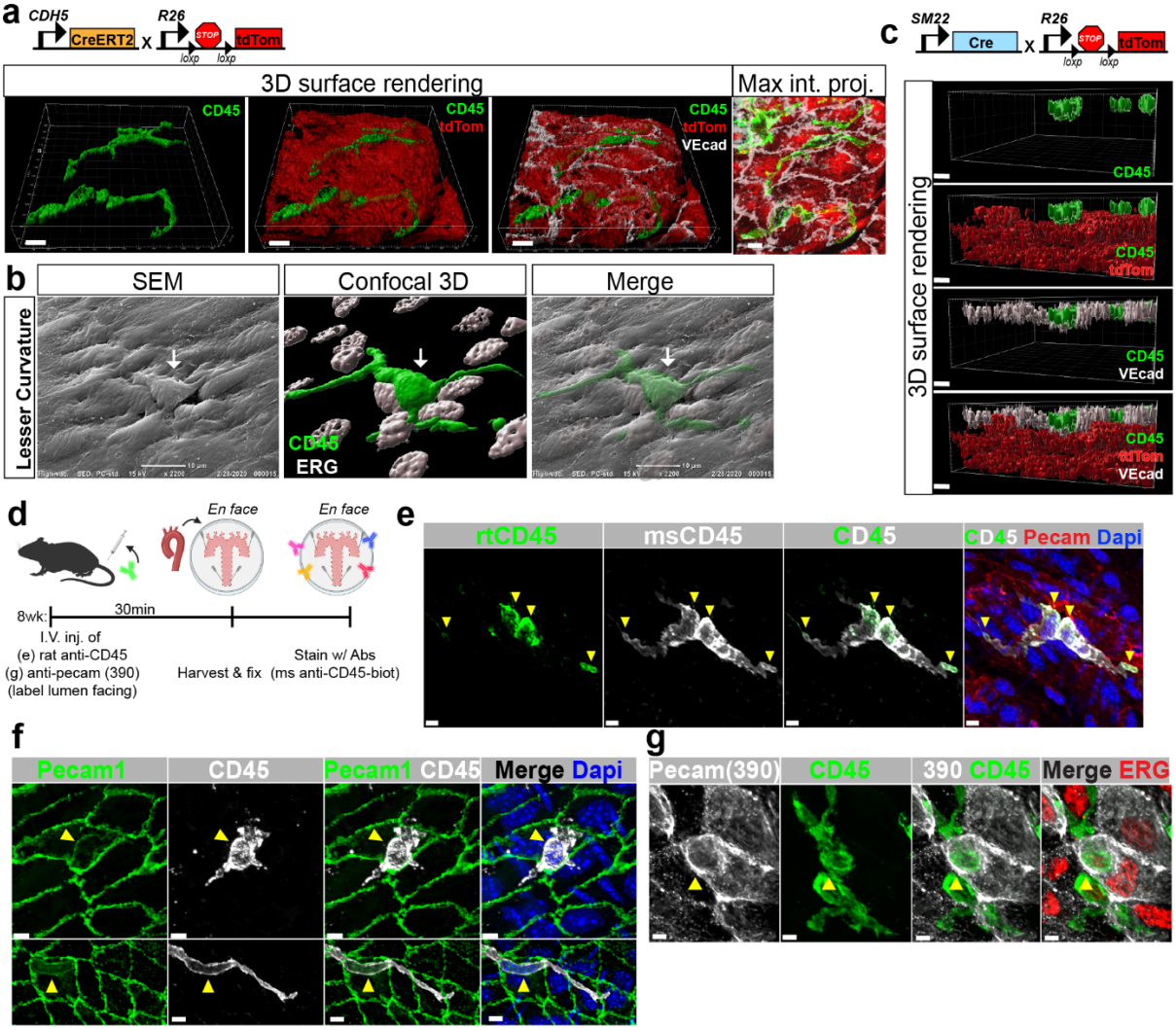

Figure 4.2. Topology of intimal myeloid cells in relation to the endothelium

a, CDH5^{CreERT2};R26^{tdTomato} construct of the mice used for 3D surface rendering of adult aortae to visualize the spatial location of intimal CD45+ cells (green) relative to the endothelium (tdTomato). VE-Cadherin is shown in white. Scale bars, 8μm, n=3. **b,** Confocal and scanning electron microscopy (SEM) images of the same aorta overlaid to determine location of intimal CD45+ cells (green in confocal) in relation to the endothelium. ERG was used to visualize endothelial nuclei in the confocal images. Scale bar, 10μm, n=3. **c,** SM22^{cre};R26^{tdtomato} construct of mice used for 3D rendering. Side view of 3D surface image of adult aortae to visualize spatial location of intimal CD45+ cells (green) relative to the vascular smooth muscle cells (tdTomato). Endothelial cells were visualized with VE-cadherin antibodies (white). Scale bars, 5μm, n=3. **d,** Schema of experimental design related to panel **e** and **g**.Tail vein injection of (e) rat anti-CD45

antibody (detected in green) was followed by euthanasia and fixation of the aorta 30min later. Subsequent permeabilization and staining with an additional, distinct CD45 antibody (detected using far-red – labeled in white). **e,** *En face* images of the experiment described. Yellow arrowheads indicate the portions of immune cells exposed to the lumen. In white is the identification of mouse anti-CD45 biotinalyated antibody labeled with strepaviden-a647 used in immunostaining post-permeabilization. Pecam-1 (in red) and DAPI (blue). Scale bar, 5μm, n=3. **f,** *En face* images of the lesser curvature (LC) staining for Pecam-1 (green). Yellow arrowheads show faint Pecam-1positivity in CD45+ cells residing in the intima. Endothelial cells were detected in green with Pecam1. Scale bar, 5μm, n=6. **g,** C57BL/6 mice were injected intravenously with non-blocking Pecam-1 (390) antibody to further examine exposure of cell bodies to the lumen. Mice were sacrificed and harvested 15mins post-injection. CD45 (in green) was used to identify immune cells and ERG (red) was used to identify endothelial cells. Yellow arrowheads indicate Pecam-1+ regions of the intimal immune cells. Scale bar, 4μm, n=3.

Figure 4.3

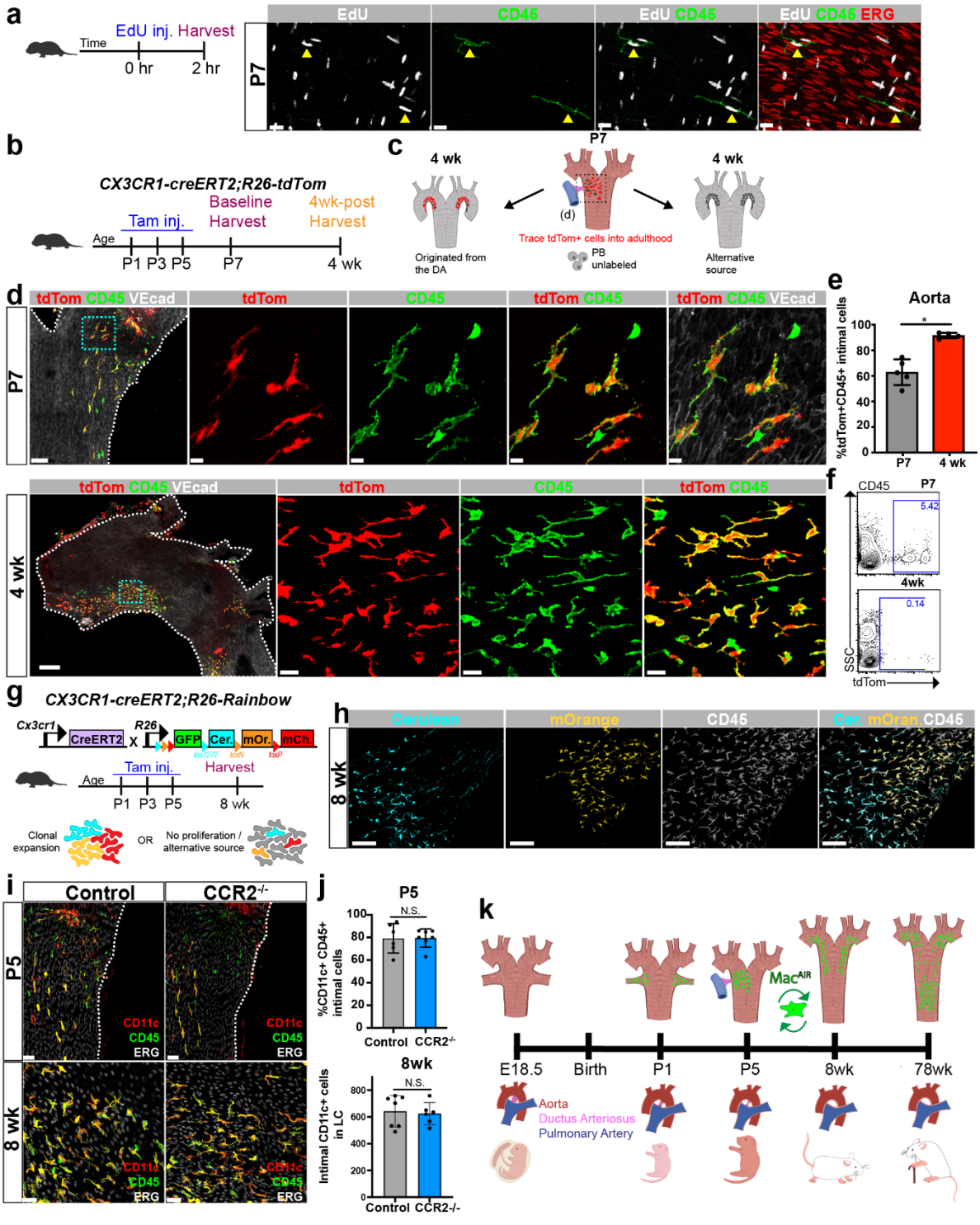
a
Time
EdU inj. Harvest
0 hr
2 hr
P7
EdU
CD45
EdU CD45
EdU CD45 ERG
b
CX3CR1-creERT2;R26-tdTom
Tam inj.
Baseline Harvest
4wk-post Harvest
Age
P1 P3 P5
P7
4 wk
c
4 wk
P7
4 wk
(d)
Trace tdTom+ cells into adulthood
PB unlabeled
Originated from the DA
Alternative source
d
tdTom CD45 VEcad
tdTom
CD45
tdTom CD45
tdTom CD45 VEcad
P7
4 wk
e
Aorta
%tdTom+CD45+ intimal cells
P7
4 wk
f
CD45
P7
5.42
4wk
0.14
SSC
tdTom
g
CX3CR1-creERT2;R26-Rainbow
Cx3cr1
CreERT2
R26
GFP
Cer.
mOr.
mCh.
Tam inj.
Harvest
Age
P1 P3 P5
8 wk
Clonal expansion
OR
No proliferation / alternative source
h
Cerulean
mOrange
CD45
Cer. mOran. CD45
8 wk
i
Control
CCR2-/-
P5
8 wk
CD11c
CD45
ERG
j
P5
N.S.
%CD11c+ CD45+ intimal cells
Control
CCR2-/-
8wk
N.S.
Intimal CD11c+ cells in LC
Control
CCR2-/-
k
MacAIR
E18.5
Birth
P1
P5
8wk
78wk
Aorta
Ductus Arteriosus
Pulmonary Artery

Figure 4.3. Aortic intimal macrophages seed the aorta immediately post-birth and self-renew in areas of oscillatory and disturbed flow

a, Schema of experimental design. Injection of EdU was applied to P7 mice 2hrs prior to euthanasia. Intimal CD45+ cells (in green) proliferate (EdU+ in white) *in situ* (yellow arrowheads). Endothelial cells were visualized with ERG (in red). Note, EdU+ CD45+ cells are negative for ERG. Scale bar, 20μm, n=3. **b,** Lineage Tracing experimental design: $Cx3cr1^{creERT2}$;$R26^{tdTomato}$ neonates were administered tamoxifen at P1, P3, and P5. At P7, aortae were harvested from half of the litter to obtain a baseline control for normalization of reporter expression. At 4wks, aortae were harvested from the remaining littermates to assess retention of reporter expression in Mac^{AIRs}. **c,** Illustration depicting the possible outcomes of the experiment. Note, labeling of circulating blood cells tdTomato is negligible in this model (as per panel g). Peripheral blood (PB). **d,** tdTomato+ intimal immune cells in P7 (top) and 4wk (bottom) aortae of $Cx3cr1^{creERT2}$;$R26^{tdTomato}$ post-neonatal tamoxifen administration. Note, Mac^{AIRs} in the lesser curvature of 4wk $Cx3cr1^{creERT2}$;$R26^{tdTomato}$ aortae retained reporter expression (tdTomato+) when labeled postnatally, as per comparison between P7 (baseline) and 4wks (lineage traced). Immune cells were visualized with CD45 (green), VE-Cad was used to visualize endothelial cells (white). Scale bar, 80μm and 10μm, n=5 (P7); 300μm and 20μm, n=4 (4wk). **e,** Percentage of intimal tdTomato+ CD45+ cells in $Cx3cr1^{creERT2}$;$R26^{tdTomato}$ aortae at P7 and 4wk when labeled with tamoxifen post-natally (n=4-5, Mann-Whitney T-test, ± SD, *$p \leq 0.05$). **f,** Representative FACS plots of tdTomato labeling in circulating blood cells at P7 and 4wks (n=3-4). **g,** Clonal tracing model, experimental design, and possible outcomes. $Cx3cr1^{creERT2}$;$R26^{Rainbow}$ neonates were administered tamoxifen at P1, P3, and P5. At 8wks, aortae were harvested to evaluate clonal expansion and labeling of Mac^{AIRs}. **h,** Clones of Mac^{AIRs} labeled with different fluorescent proteins at 8wk (initial tamoxifen injection at P1, P3 and P5). CD45+ cells were detected in white. Scale bar, 100μm; n=5. **i,** *En face* images comparing intimal CD11c+CD45+ cells from control and $CCR2^{-/-}$ mice at P5 (top row, former

ductus arteriosus region) and 8wk (bottom row, lesser curvature of aortic arch). CD11c (in red), CD45 (in green) and ERG (in white). Scale bar, 100μm and 50μm; n=3-7. **j,** Comparison of intimal CD11c+CD45+ cells in control and $CCR2^{-/-}$ P5 aortae (n=6-7, Mann-Whitney T-test, ± SD, *p ≤ 0.05) or in the lesser curvature of the aortic arch in 8wk aortae (n=3-4, Mann-Whitney T-test, ± SD, *p ≤ 0.05). **k,** Schematic summary of findings (from Figures 1-3). Intima-resident macrophages (Mac^{AIR}) enter the aorta via the ductus arteriosus immediately post-birth, expand through self-renewal and populate the lesser curvature of the aortic arch. Eventually with age, macrophages also accumulate in the descending aorta.

Figure 4.4

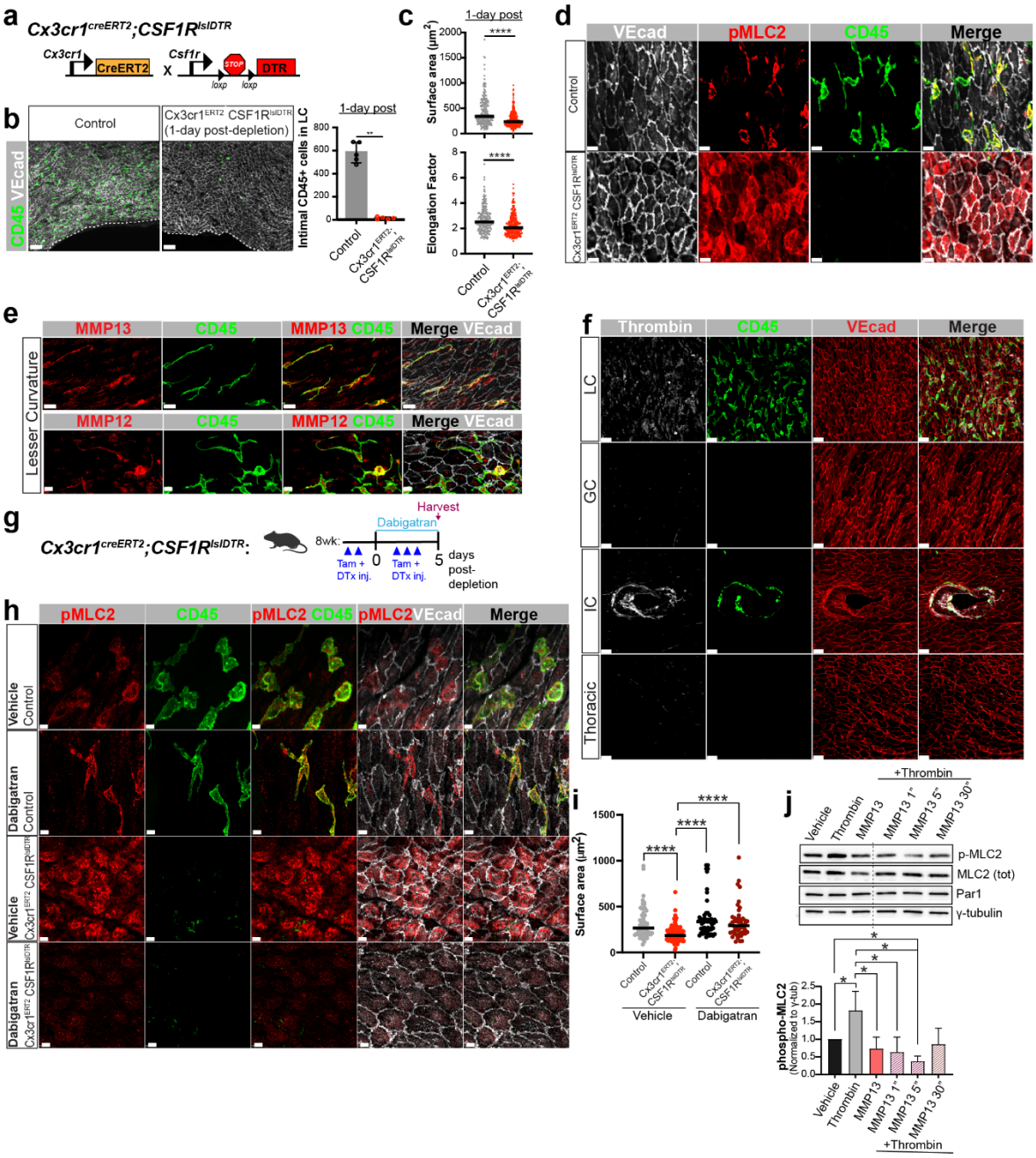

Figure 4.4. MacAIRs are essential to prevent thrombin-mediated endothelial cell contraction in regions of oscillatory and disturbed flow

a, Schema of constructs used to deplete the Mac^{AIR} population. Inducible macrophage depletion model (Cx3cr1^{creERT2};CSF1R^{lslDTR}) requires treatment of both tamoxifen and diphtheria toxin to induce apoptosis on double positive cells. Diphtheria toxin receptor (DTR). **b,** *En face* images and total number of intimal CD45+ cells in the lesser curvature (LC) of the aortic arch from littermates controls and Cx3cr1^{creERT2}; CSF1R^{lslDTR} mice that were exposed to post-

tamoxifen and diphtheria toxin for 24hrs. Both control and experimental mice were injected with tamoxifen and diphtheria toxin. CD45+ (green) cells in the aorta are nearly completely depleted by this approach. Scale bar, 50μm; n=5, Mann-Whitney *T*-test, ± SD, **p ≤ 0.01. **c,** Surface area and elongation factor measurements of endothelial cells in the lesser curvature of Cx3cr1^{creERT2};CSF1R^{lslDTR} and littermate controls post-Mac^{AIR} depletion in aortae. VE-cadherin staining was used to identify cell borders (n= 3-4, Mann-Whitney T-test, ± SD, ****p ≤ 0.0001). **d,** Phosphorylated-myosin light chain 2 (pMLC2) staining (red) in the lesser curvature of the aortic arch 1-day post-tamoxifen and diphtheria toxin injection in control and Cx3cr1^{creERT2};CSF1R^{lslDTR} mice. CD45 (green) and VE-Cadherin (in white). Scale bar, 10μm, n=5. **e**, *En face* images co-staining for MMP12 or MMP13 (red), CD45 (green), and VE-Cadherin (white). Note co-localization of MMP12 and 13 with CD45+ cells. Scale bar, 20μm and 10μm, n=3. **f,** Concentration of thrombin in areas of oscillatory and disturb flow in 8wk old C57BL/6 aortae (lesser curvature (LC), greater curvature (GC), intercostal artery (IC), Scale bar, 20μm, n=3). **g-i** Effects of Dabigatran on Cx3cr1^{creERT2};CSF1R^{lslDTR} and control aortae. **g,** Experimental design. 8wk old Cx3cr1^{creERT2};CSF1R^{lslDTR} and littermate controls were injected with tamoxifen (Tam) and diphtheria toxin (DTx) to induce depletion of Mac^{AIRs}. Additionally, mice were treated with vehicle or Dabigatran for 5 days. Note, constant injection of tamoxifen and diphtheria toxin is needed to keep macrophages from re-populating the lesser curvature. **h,** Representative *en face* images of the lesser curvature 5-days post-experimental manipulation as indicated. Immunocytochemistry included pMCL2 (red), CD45 (green) and (VE-Cadherin in white). Note the impressive loss of pMLC2 in dabigatron-treated Cx3cr1^{creERT2};CSF1R^{lslDTR} Mac^{AIR} depleted mice. Scale bar, 7μm, n=4-10. **i,** Surface area measurements of endothelial cells in the lesser curvature of Cx3cr1^{creERT2};CSF1R^{lslDTR} and littermate control 5-days post-dabigatran treatment (n=4-10, Mann-Whitney T-test, ± SD, ****p ≤ 0.0001). **j**, Western blot analysis of human aortic endothelial cells (HAECs) treated with Thrombin, MMP13, or pre-treated with MMP13 for 1min, 5min, and 30min and then additionally stimulated with Thrombin for 5 mins (n=4, Mann-Whitney T-test, ± SD, *p ≤ 0.05).

Figure 4.5

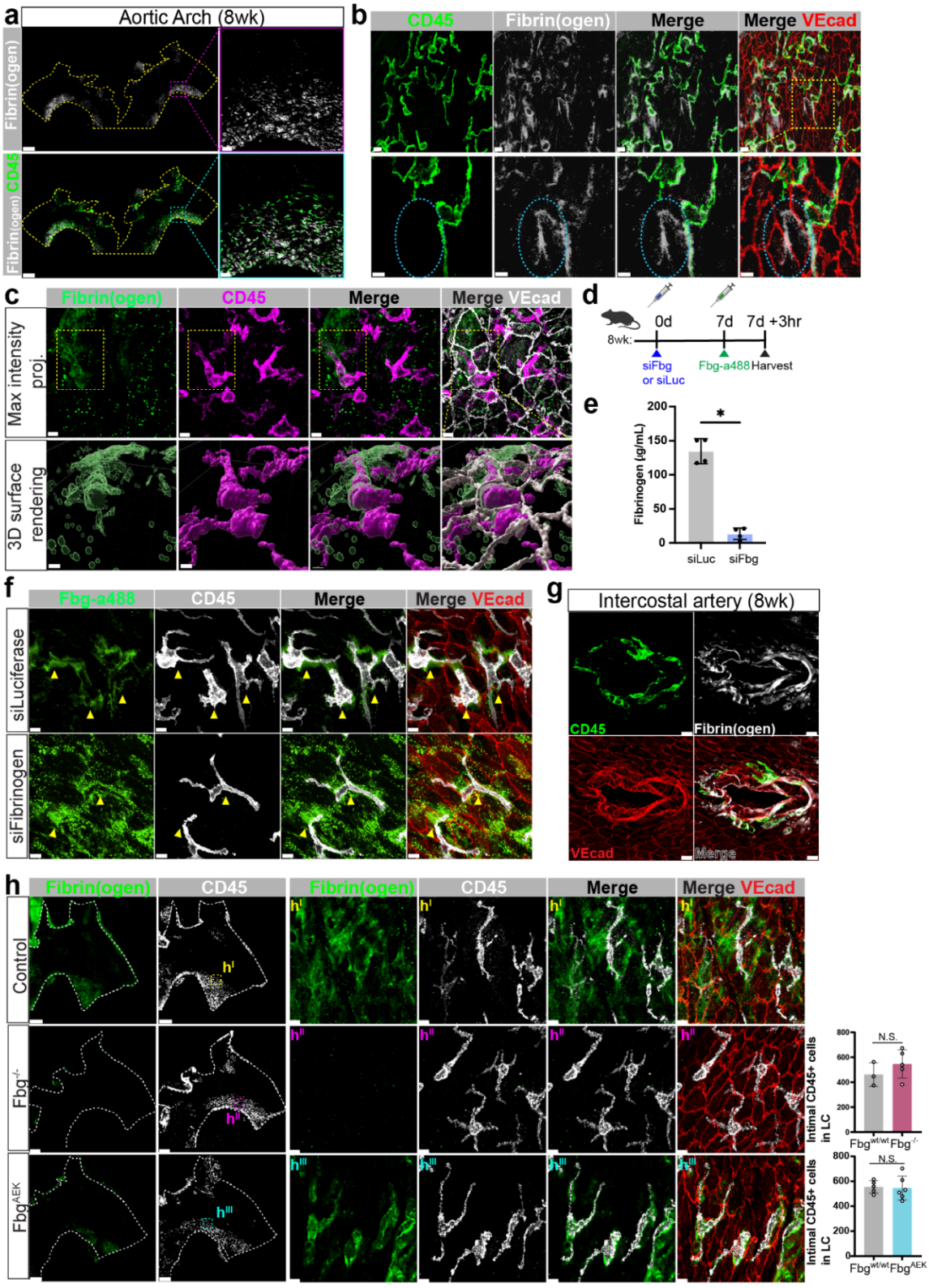
a
Aortic Arch (8wk)
Fibrin(ogen)
Fibrin(ogen) CD45
b
CD45
Fibrin(ogen)
Merge
Merge VEcad
c
Fibrin(ogen)
CD45
Merge
Merge VEcad
Max intensity proj.
3D surface rendering
d
8wk:
0d
7d
7d +3hr
siFbg or siLuc
Fbg-a488
Harvest
e
Fibrinogen (µg/mL)
200
150
100
50
0
*
siLuc
siFbg
f
Fbg-a488
CD45
Merge
Merge VEcad
siLuciferase
siFibrinogen
g
Intercostal artery (8wk)
CD45
Fibrin(ogen)
VEcad
Merge
h
Fibrin(ogen)
CD45
Fibrin(ogen)
CD45
Merge
Merge VEcad
Control
Fbg-/-
FbgAEK
hI
hII
hIII
Intimal CD45+ cells in LC
800
600
400
200
0
N.S.
Fbgwt/wt
Fbg-/-
FbgAEK

Figure 4.5. Fibrin(ogen) is deposited and binds to MacAIRs in regions that experience oscillatory and disturbed flow

a, Whole mount, *en face* images of fibrin(ogen) (white) and CD45+ cells (green) in the aortic arch of 8wk old C57BL/6 mice. Scale bar, 500μm and 50μm, n=20. **b,** Fibrin(ogen) (white) was overlaid with CD45 staining (green) in adult aortic arch. Higher magnification (lower panel) of blue dotted insert highlights fibrin(ogen) staining in an area that resembles the cellular process of a Mac^{AIR} (blue dotted eclipse). Scale bar,10μM and 5μM. **c,** *En face* images of fibrin(ogen) location in the aortic arch displayed using max intensity projections (top row) and 3D surface rendering (bottom row). Scale bar, 7μm and 4μm, n=16. **d,** Experimental design. 8wk old C57BL/6 mice were injected via tail vein with either siFibrinogen or siLuciferase (control). 7-days later, mice were tail vein injected with fibrinogen conjugated to a488 (fbg-a488). After 3 hours post-fbg-a488 injection, aortae were harvested for analysis. **e,** Plasma levels of Fibrinogen 7-days post-mRNA injection, measured by ELISA (n=4, Mann-Whitney T-test, ± SD, *p ≤ 0.05). **f,** Distribution of intravenously injected fbg-a488 in relation to Mac^{AIRs}. CD45 (white). Yellow arrowheads indicate surface bound fbg-a488 to Mac^{AIRs} (n=4, Scale bar, 4μm). **g,** Adult (8wk) intercostal artery exhibiting fibrin(ogen) deposition (white) and intimal CD45+ cells accumulation (green). VE-Cadherin identifies endothelial cells in red. (Scale bar, 70μm, n=15). **h,** *En face* images of the aortic arch comparing fibrin(ogen) accumulation (green) and immune cell (CD45, white) deposition in Control (h^{I}), fibrinogen-/- ($Fbg^{-/-}$, h^{II}), and $fibrinogen^{AEK}$ (Fbg^{AEK}, h^{III}). VE-Cadherin identifies endothelial cells in red. Scale bar, 300μm and 8μm, n=3-4. Adjacent graph represents the quantifications of Mac^{AIRs} in the lesser curvature of the aortic arch in $Fbg^{-/-}$ and Fbg^{AEK} mice compared to colony controls (n=3-4, Mann-Whitney T-test, ± SD, *p ≤ 0.05).

Figure 4.6.

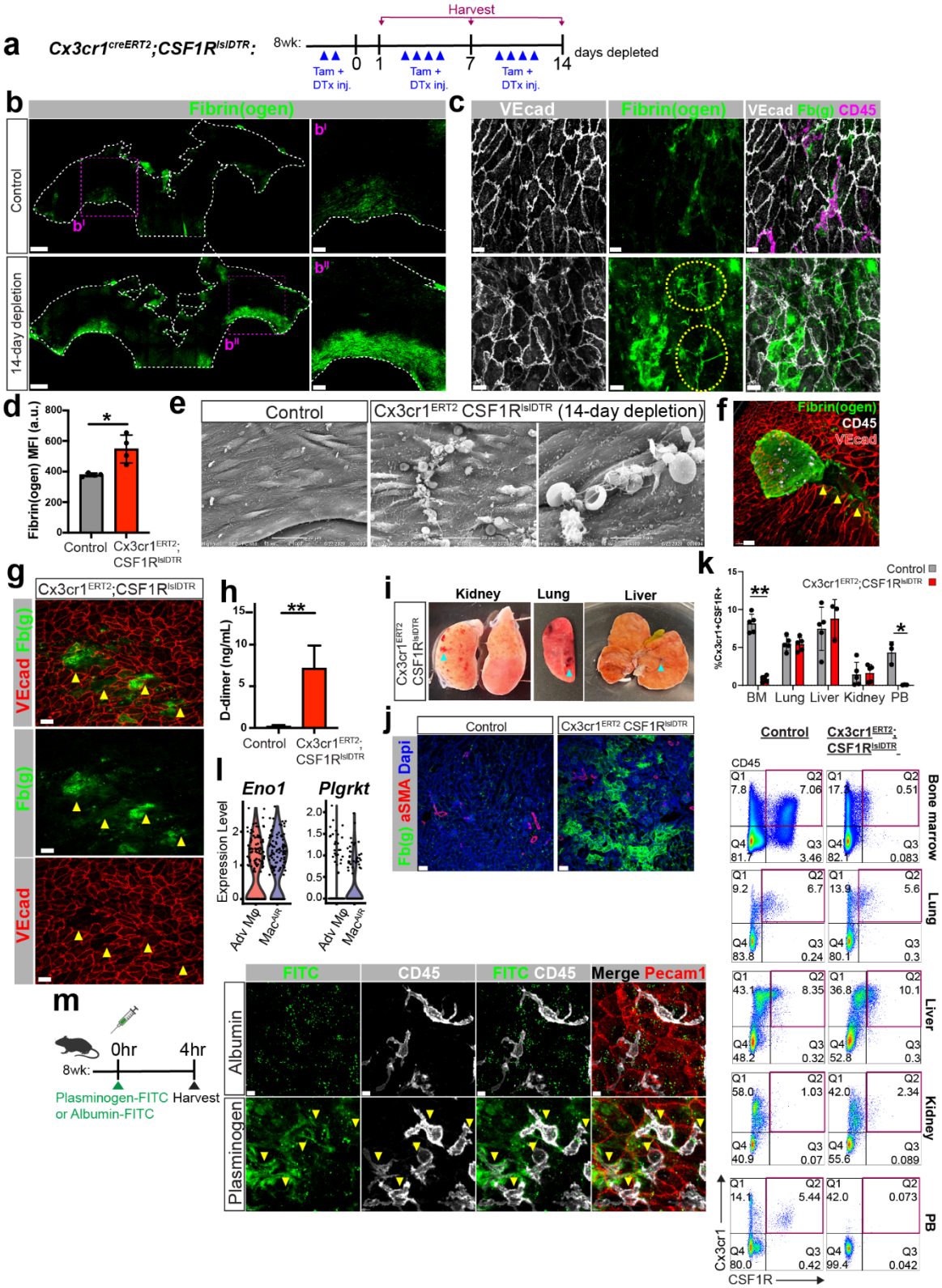
a
Cx3cr1creERT2;CSF1RlsIDTR:
8wk:
Harvest
0
1
7
14
days depleted
Tam + DTx inj.
Tam + DTx inj.
Tam + DTx inj.
b
Fibrin(ogen)
Control
14-day depletion
c
VEcad
Fibrin(ogen)
VEcad Fb(g) CD45
d
Fibrin(ogen) MFI (a.u.)
Control
Cx3cr1ERT2; CSF1RlsIDTR
e
Control
Cx3cr1ERT2 CSF1RlsIDTR (14-day depletion)
f
Fibrin(ogen)
CD45
VEcad
g
Cx3cr1ERT2;CSF1RlsIDTR
VEcad Fb(g)
Fb(g)
VEcad
h
D-dimer (ng/mL)
Control
Cx3cr1ERT2; CSF1RlsIDTR
i
Kidney
Lung
Liver
Cx3cr1ERT2 CSF1RlsIDTR
j
Control
Cx3cr1ERT2 CSF1RlsIDTR
Fb(g) aSMA Dapi
k
Control
Cx3cr1ERT2;CSF1RlsIDTR
%Cx3cr1+CSF1R+
BM
Lung
Liver
Kidney
PB
Control
Cx3cr1ERT2; CSF1RlsIDTR
CD45
Bone marrow
Lung
Liver
Kidney
PB
Cx3cr1
CSF1R
l
Eno1
Plgrkt
Expression Level
Adv Mφ
Mac4IR
m
8wk:
0hr
4hr
Plasminogen-FITC or Albumin-FITC
Harvest
FITC
CD45
FITC CD45
Merge Pecam1
Albumin
Plasminogen

Figure 4.6. MacAIRs are necessary to clear fibrin deposits in regions of oscillatory and disturbed blood flow.

a, Experimental design schematic for long-term Mac^{AIR} depletion. $Cx3cr1^{creERT2}$;$CSF1R^{lslDTR}$ mice and littermate controls were injected every other day, alternating tamoxifen (Tam) and diphtheria toxin (DTx) for 14-days. **b,** Increased accumulation of fibrin(ogen) (green) in the lesser curvature of aortae 14-days post-continued Mac^{AIR} depletion in $Cx3cr1^{creERT2}$;$CSF1R^{lslDTR}$ mice compared to littermate control (Scale bar, 500μm (B) and 150μm (b^{I-II})). **c,** Fibrin fibrils (green) observed in aortae 14-days of continued Mac^{AIR} depletion (yellow dotted ovals). VE-Cadherin identifies endothelial cells in white and CD45 is shown in pink (Scale bar, 10μm, n=4-11). **d,** Mean Fluorescence Intensity of Fibrin(ogen) in the lesser curvature of the aortic arch in $Cx3cr1^{creERT2}$;$CSF1R^{lslDTR}$ 14-days post-macrophage depletion compared to littermate controls (n=4, Mann-Whitney *T*-test, ± SEM, *p ≤ 0.05). **e,** *En face* scanning electron microscopy images showing microthrombi and fibrin accumulating in the lesser curvature of the aortic arch in $Cx3cr1^{creERT2}$;$CSF1R^{lslDTR}$ mice 14-days post-continued Mac^{AIR} depletion. Scale bar, 20μm and 5μm. **f,** Microthrombi (green) and intima rupture (yellow arrowheads) of a $Cx3cr1^{creERT2}$;$CSF1R^{lslDTR}$ mouse that had to be euthanized due to declined health 7-days post-continued macrophage depletion. Scale bar, 20μm. **g,** Intima rupture in the aortae of $Cx3cr1^{creERT2}$;$CSF1R^{lslDTR}$ 14-days post-continued Mac^{AIR}-depletion. Yellow arrowheads indicate ruptured areas that also showed high concentration of fibrin(ogen) deposits. VE-Cadherin identifies endothelial cells in red. Scale bar, 20μm. **h,** D-dimer plasma levels in $Cx3cr1^{creERT2}$;$CSF1R^{DTR}$ and littermate control mice 14-days post-macrophage depletion (n=6-13, Mann-Whitney *T*-test, ± SEM, **p ≤ 0.01). **i-j,** Kidneys, lung, and liver from sick $Cx3cr1^{creERT2}$;$CSF1R^{DTR}$ mouse 7- or 14-days of macrophage depletion. **i** Note multiple hemorrhagic foci (blue arrow head). **j,** Fibrin(ogen) immunohistochemistry on kidney sections of control and $Cx3cr1^{creERT2}$;$CSF1R^{DTR}$ mice. Scale bar, 50μm. **k,** Flow cytometry analysis evaluating the percentage of Cx3cr1+Csf1r+CD45+ cells in bone marrow (BM), lung, liver, kidney, and peripheral blood (PB) in control and $Cx3cr1^{creERT2}$;$CSF1R^{DTR}$ mice one day post-diphtheria toxin injection (n=5, Mann-Whitney *T*-test, ± SEM, *p ≤ 0.05, **p ≤ 0.01). Representative flow cytometry plots are below graph. **l,** Transcript levels of plasminogen receptors (Eno1 and Plgrkt) in adventitial macrophages and Mac^{AIRs} from scRNA-seq data sets in Supplemental Fig. 2. **m,** Experimental design of FITC-conjugated albumin or plasminogen intravenous injection (on the left). Aortae were harvested 4hrs post-injection. On the right: visualization of the experimental outcome in the *en face* aortae. Distribution of intravenously injected FITC-conjugated albumin (control, upper panels) or plasminogen (lower panels) in

relation to Mac^{AIRs} (yellow arrow heads) identified by CD45 (white). Endothelial cells were identified by Pecam1 (red). Scale bar, 5μm; n=3.

Figure 4.7

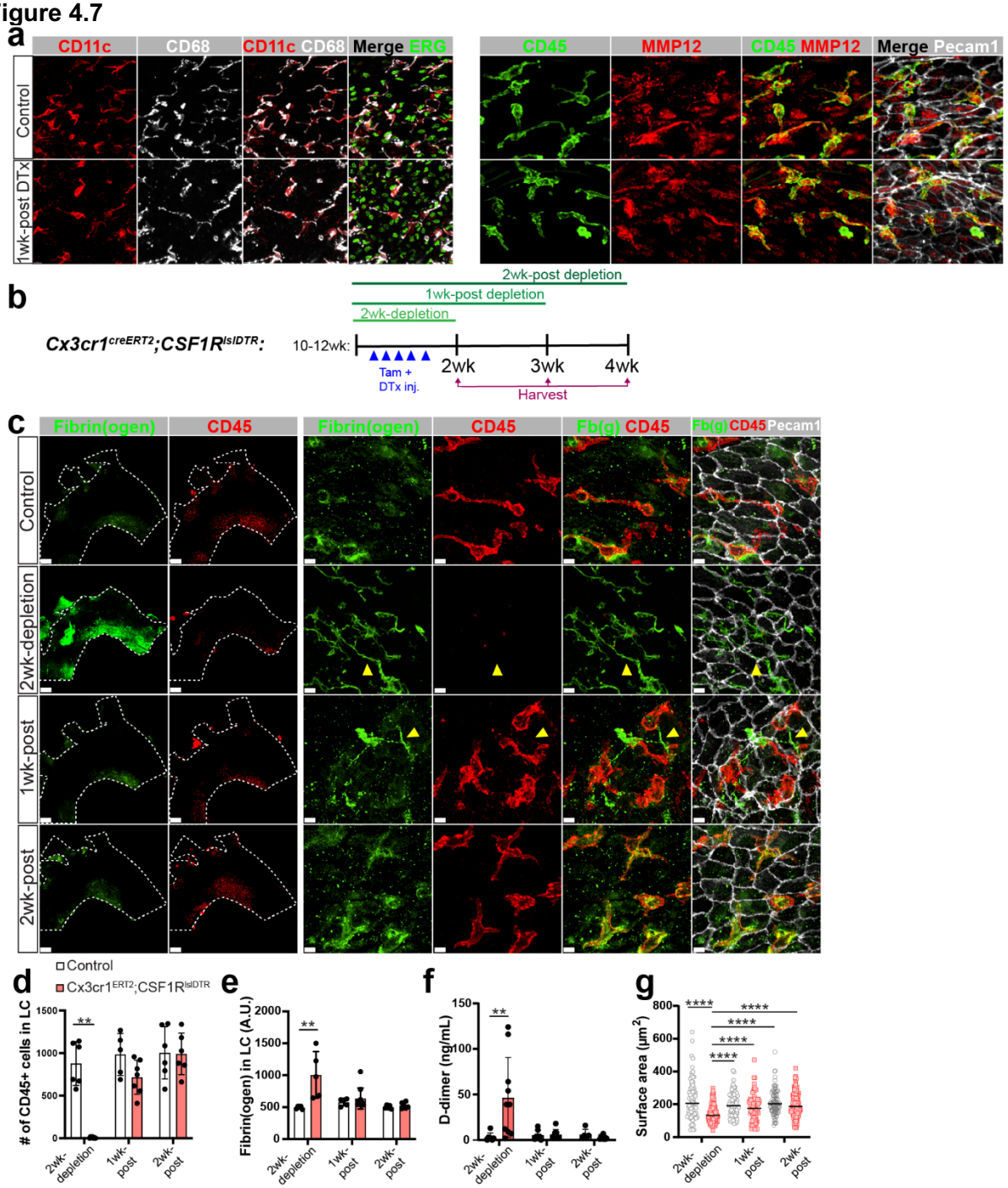

Figure 4.7. Rescue of the phenotype (fibrin accumulation) upon return of MacAIRs

a, *En face* images of littermate control and Cx3cr1^{creERT2};CSF1R^{DTR} mice 1-wk after single-diphtheria (DTx) injection. Stopping tamoxifen and DTx injections ceases the pressure of cell ablation and allows for the repopulation of intimal immune cells. Aortae were stained for Mac^{AIR} markers to validate the monocyte-derived population that repopulates the arch after resident population is depleted have the Mac^{AIR} identity (CD11c+MMP12+CD68+CD45+)(n=3; Scale bar,

15μm (left panel) & 10μm (right panel)). **b,** Schematic of macrophage rescue experiments. Littermate control and Cx3cr1^{creERT2};CSF1R^{DTR} mice were both injected with tamoxifen (tam) and diphtheria toxin (DTx) for 2 weeks of continued macrophage-depletion. After 2weeks, administration of tam and DTx stopped, allowing for Mac^{AIRs} to repopulate the aorta. Aortae *en face* were evaluated at 2wk-depletion (base-line) and after ceasing tam/DTx treatment: 1wk-post depletion (1wk-post), and 2wk post depletion (2wk-post). **c**, *En face* images evaluating fibrin(ogen) (green) and Mac^{AIR} (red) accumulation of littermate control and Cx3cr1^{creERT2};CSF1R^{DTR} aortae at the given time-points. Fibrin fibrils are noted by yellow arrow heads. Endothelial cells are identified with VE-Cadherin (white). Scale bar, 300μm, 7μm. **d**, Total number of intimal CD45+ cells in the lesser curvature (LC) of the aortic arch in littermate controls and Cx3cr1^{creERT2}; CSF1R^{lslDTR} mice at 2wk-depletion, 1wk-post depletion, and 2wk-post depletion (n=5-7, Mann-Whitney *T*-test, ± SD, **p ≤ 0.01). **e**, Mean Fluorescence Intensity of Fibrin(ogen) in the lesser curvature of the aortic arch (n= 5-10, Mann-Whitney *T*-test, ± SEM, **p ≤ 0.01). **f**, D-dimer plasma levels (n=5-10, Mann-Whitney *T*-test, ± SEM, **p ≤ 0.01). **g**, Surface area measurements of endothelial cells in the lesser curvature of Cx3cr1^{creERT2};CSF1R^{lslDTR} and littermate control. (n= 3-4, Mann-Whitney T-test, ± SD, ****p ≤ 0.0001).

SUPPLEMENTAL FIGURES

Supplemental Figure 4.1

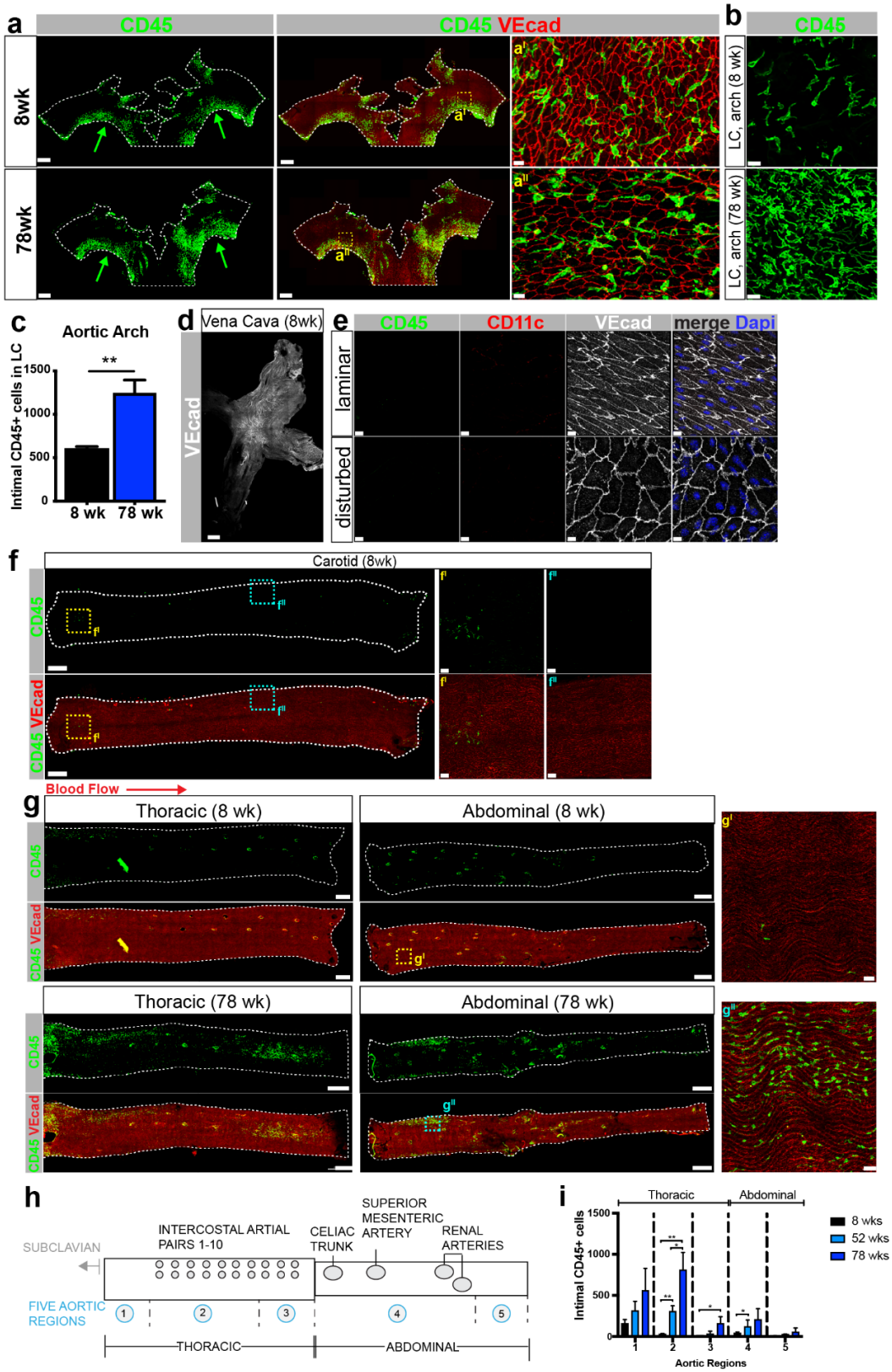

Supplemental Figure 4.1. Intimal immune cell distribution in the aorta and vena cava of young and aged mice

a, Accumulation of intimal immune cells, as per CD45 positivity (green arrows) in adult (n=498 mice evaluated) and old 78wk (n=6 mice evaluated) aortic arch of C57BL/6 mice. Endothelial cells are stained with VE-Cadherin (red). Scale bars, 500μm & 15μm (a^{I-II}). **b,** High magnification of *en face* distribution of CD45+ (green) cells in the lesser curvature (LC) of adult and aged aortae. Scale bar, 20μm. **c,** Quantification of intimal CD45+ cells in LC of 8wk and 78wk old mice. (n=3, Mann-Whitney *T*-test, ± SD, **p ≤ 0.01). **d, e** *En face* images of the vena cava of 8wk old mice. **d,** Low magnification of vena cava (Ve-Cadherin in white). Scale bar, 500μm. **e,** No intimal CD11c+(red) CD45+(green) cells were found in the vena cava, even in regions that experienced disturbed blood flow (Scale bar, 10μm, n=3). **f,** Few intimal CD45+ cells (green) accumulate in carotid arteries (8wk), endothelial cells are visualized by VE-Cadherin in red (Scale bar, 300μm, 50μm (f^{I-II}), n=8). Note high magnification inserts on the right showing opening of carotid branches (disturbed flow) where a few CD45+ cells can be detected. **g,** Whole mount, *en face* scans of the descending aortae (thoracic and abdominal regions) of 8wk and 78wk old C57BL/6 mice. Except for branches, few intimal CD45+ cells (green) were detected in 8wk old descending aortae, (g^{I}) whereas 78wk old mice display a large number of intimal CD45+ cells (g^{II}) throughout the descending aortae. Scale bar, 500μm (8wk thoracic), 700μm (8wk abdominal), 1000μm (78 wk thoracic and abdominal), and 50μm (g^{I-II}), n= 5 (8wk) and 6 (78wk). **h,** Topographic map to help guide the quantification of the number of immune cells based on anatomical location. Descending aorta divided into 5 sub-regions, as indicated and then quantified in "**i**". **i**, Progressive increase in the number of intimal CD45+ cells per aortic region with age in 8wk, 52wk, and 78wk old mice (n=3, *T*-test, ± SD, *p ≤ 0.05, **p ≤ 0.01).

Supplemental Figure 4.2.

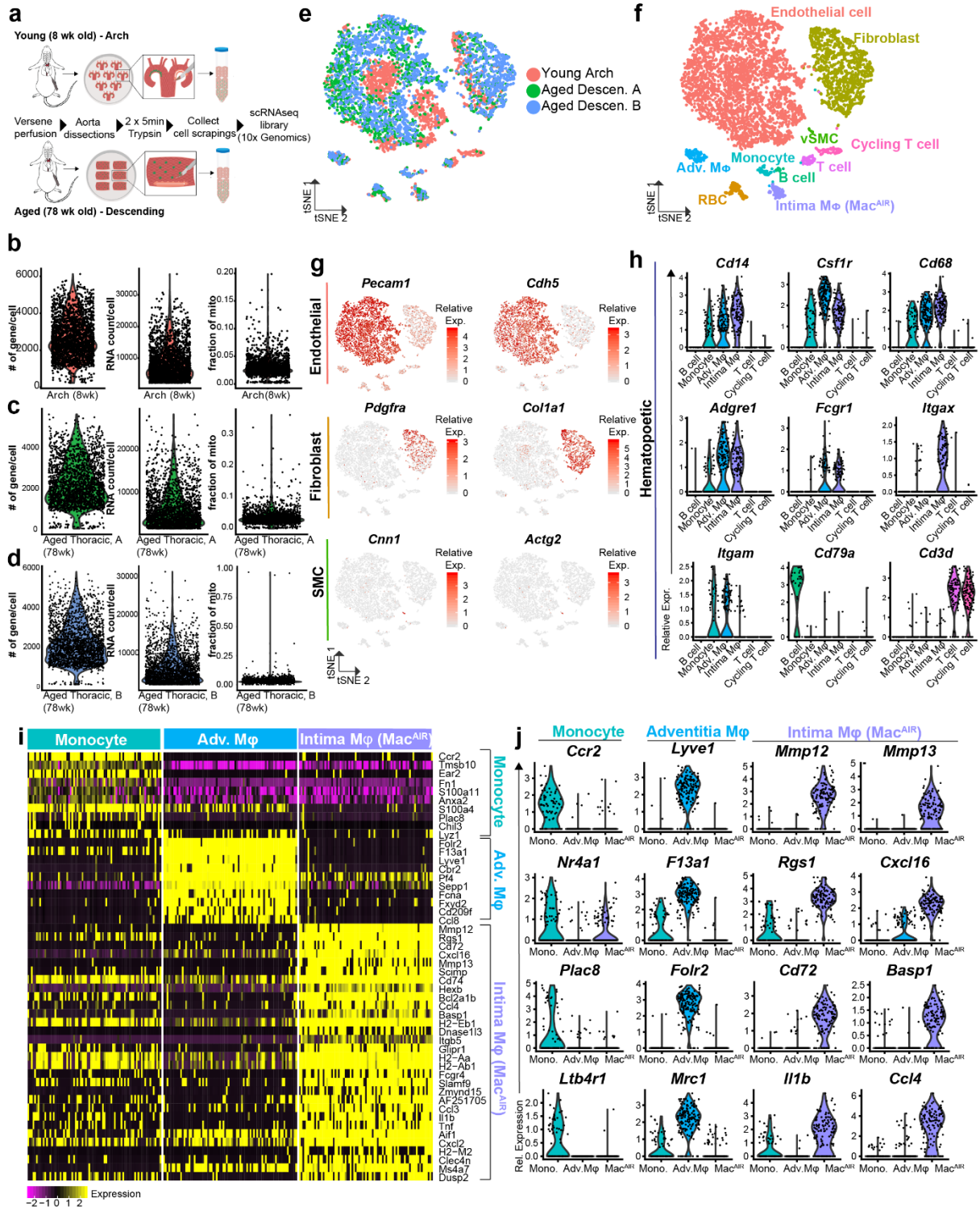

Supplemental Figure 4.2. scRNA-seq uncovers the macrophage identity and unique transcriptional signature of the intimal immune cell population

a, Schematic to illustrate the process for isolation of intimal, aortic cells for single-cell RNA sequencing. **b-d,** Violin plots representing the Quality Control (QC) metrics for each scRNAseq library: Arch and Aged Thoracic A and B. Note, Aged Thoracic A & B represent two independent libraries, not technical replicates, each composed of cells isolated from 6-8 aortae. Shown are: the number of genes per cell (nGene), the absolute number of observed transcripts per cell (nUMI, Unique Molecular Identifier), and the fraction of transcripts arising from the mitochondria genome (fration of mito). **b,** Aortic arch library (red); **c,** Aged thoracic library A (green); **d,** Aged thoracic library B (blue). **e,** tSNE plot of cells from three independent libraries: aortic arch in red (8 wk) and aged descending (descen.) A (in green) and B (in red) (78wk). 6-8 aortas were used per library. **f,** Ten distinct cell types were identified, and cellular identities were assigned to each cluster. **g,** tSNE analysis and heat map-style representation of non-hematopoietic vascular lineage markers (color key indicates expression level). **h,** Violin plots showing expression levels of the most prominent hematopoietic lineage markers shown as normalized gene expression per cell**. i,** Top differentially expressed genes expressed by monocytes, adventitia macrophages (Adv. Mϕ), aortic intima-resident macrophages (Mac^{AIR}). **j,** Violin plots showing expression levels of selected genes that distinguished monocytes (left column), Adv. Mϕ (center left column), and Mac^{AIR} (right columns).

Supplemental Figure 4.3

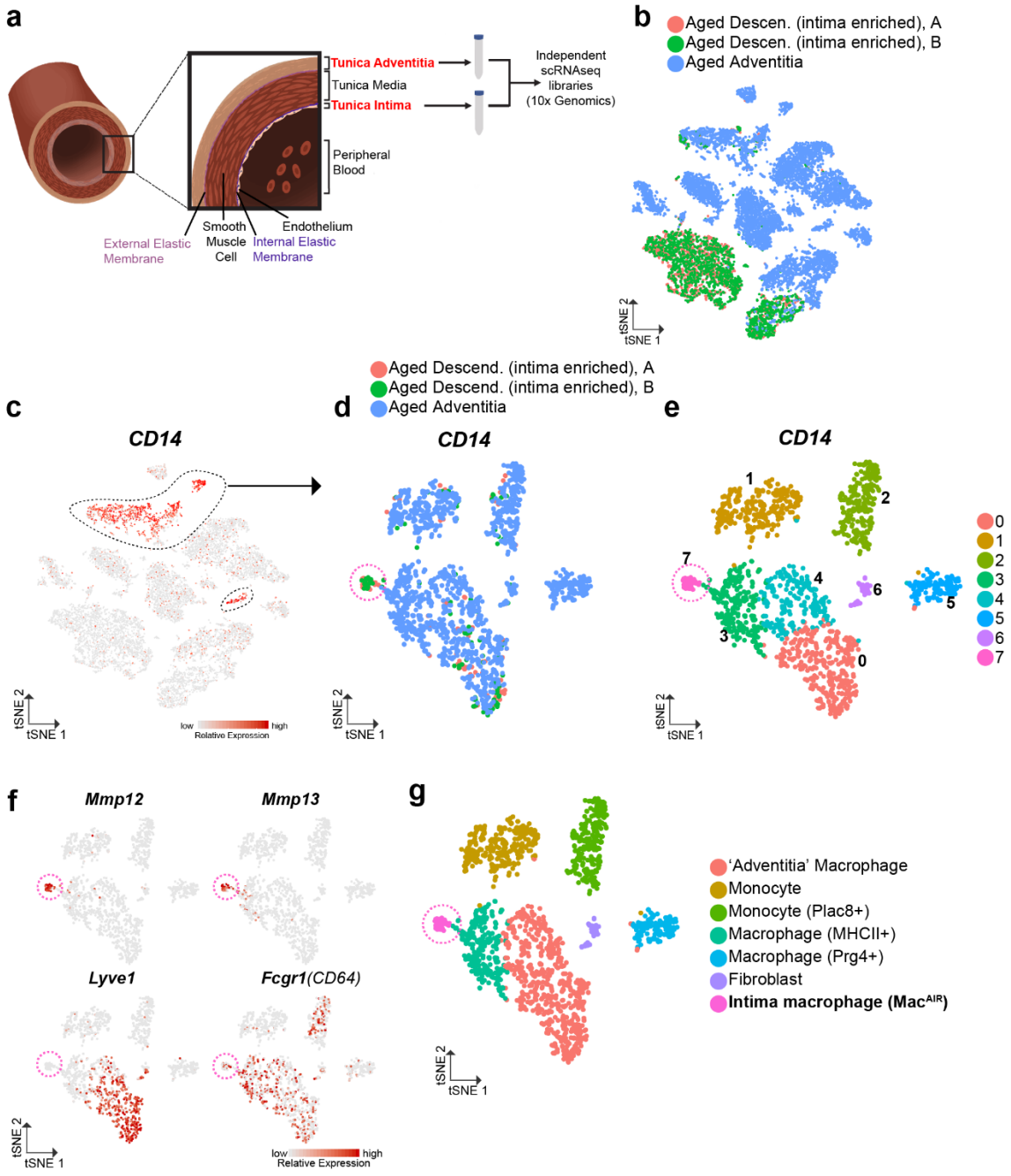

Supplemental Figure 4.3. scRNAseq on dissected adventitia

a, Illustration displaying the different aortic layers and highlighting the tissue that was dissected and used to generate independent scRNAseq libraries for comparison: tunica adventitia vs tunica intima, (red text). **b**, tSNE projections of cells from three independent libraries: aged adventitia (78 wk) and aged thoracic A and B (78wk). **c,** Expression of *CD14* to identify myeloid cells in aged thoracic and aged adventitia data sets. **d**, tSNE plot displaying only the *CD14*

expressing cells from c. Pink dotted circle highlights a cluster of cells that are exclusively found in intimal-enriched libraries (Aged Thoracic A and B). **e**, tSNE plot identifying unique cell clusters presented in d. Note, cluster 7 (pink dotted cluster) is a distinct population. **f**, Expression of *Lyve1* was used to identify adventitia macrophages and *Fcgr1* was used to identify macrophages. Note, Cluster 7 expresses *Fcgr1* and also highly expresses *Mmp12* and *Mmp13* but it does not express *Lyve1*. **g**, Cellular identities assigned to each cluster identified based on transcriptional expression patterns.

Supplemental Figure 4.4

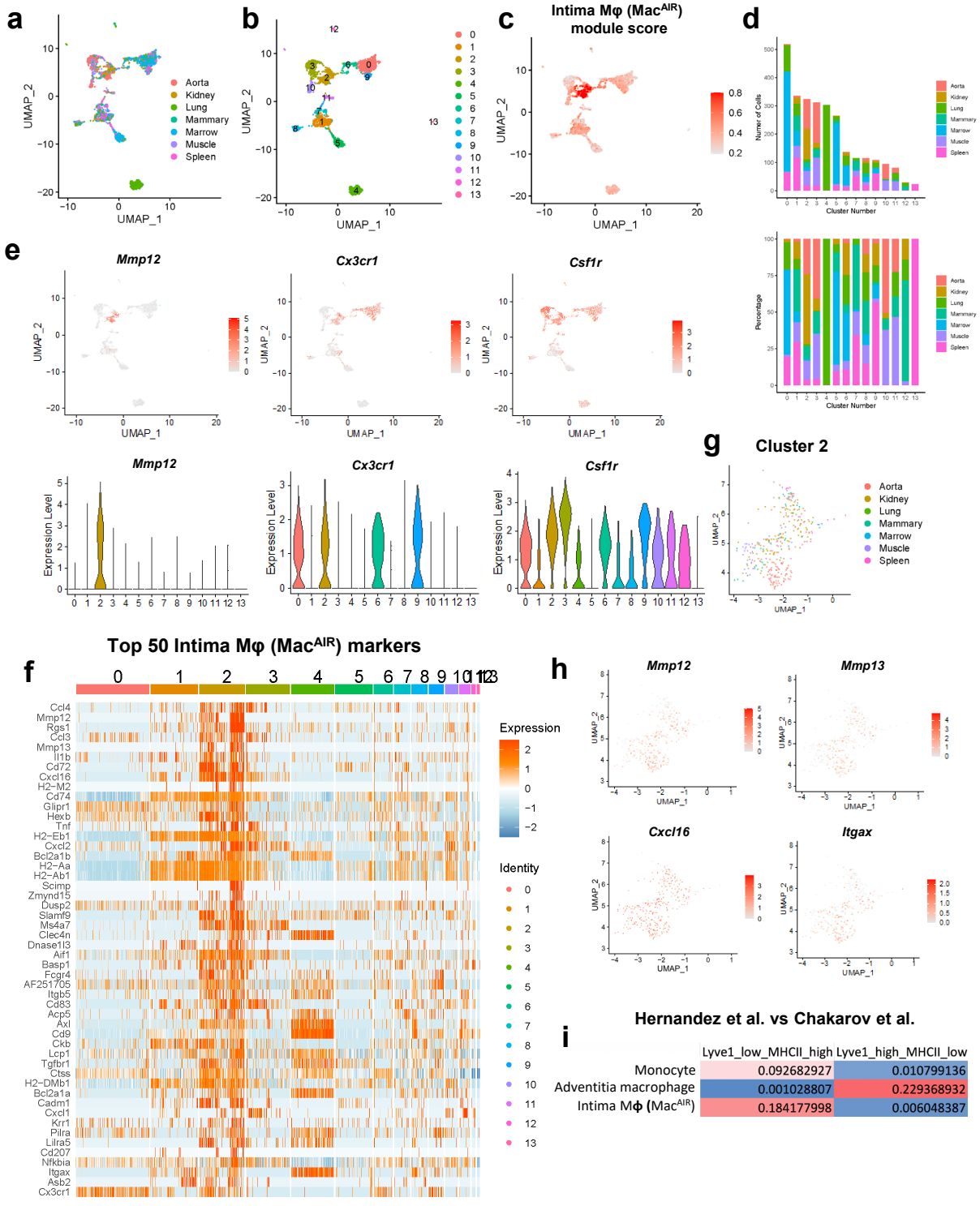

	Lyve1_low_MHCII_high	Lyve1_high_MHCII_low
Monocyte	0.092682927	0.010799136
Adventitia macrophage	0.001028807	0.229368932
Intima Mϕ (MacAIR)	0.184177998	0.006048387

Supplemental Figure 4.4. MacAIR comparison to other published macrophage data sets

a, Uniform manifold approximation and projection (UMAP) plot of monocytes and macrophages extracted from the Tabula muris atlas and merged with the aortic intima-macrophage (Mac^{AIR}) data set ("Aorta") from this work. **b**, UMAP plot identifying distinct cell clusters based on transcriptional signatures. **c**, Mac^{AIR} marker genes were used to calculate a module score, which was used to identify cells from the Tabula muris atlas that were similar to Mac^{AIR}. The Mac^{AIR} module score was applied and represented by heat map-style UMAP plot. **d**, Number (top graph) and percentage (bottom graph) of cells from each tissue that are in each cluster. **e**, UMAP heat map-style representation of MMP12 (Mac^{AIR} marker), Cx3cr1, and Csf1r (top row) with violin plot representation of each given gene below. **f**, Heat map comparing the top 50 MacAIR markers to all the clusters found in b. **g**, UMAP plotting only cluster 2 and showing tissue origin. **h**, UMAP heat map-style representation of top Mac^{AIR} markers: Mmp12, Mmp13, Cxcl16, Itgax (CD11c). **i**, Differential genes from the comparison among monocytes, adventitia macrophages, and Mac^{AIR} (our data – this study) were overlapped with genes extracted from the comparison between the $Lyve^{low}MHCII^{high}$ and $Lyve^{high}MHCII^{low}$ macrophages from the Chakarov et al. dataset. The jaccard index between each pair for cell types from the two datasets were calculated and plotted in the heatmap.

Supplemental Figure 4.5

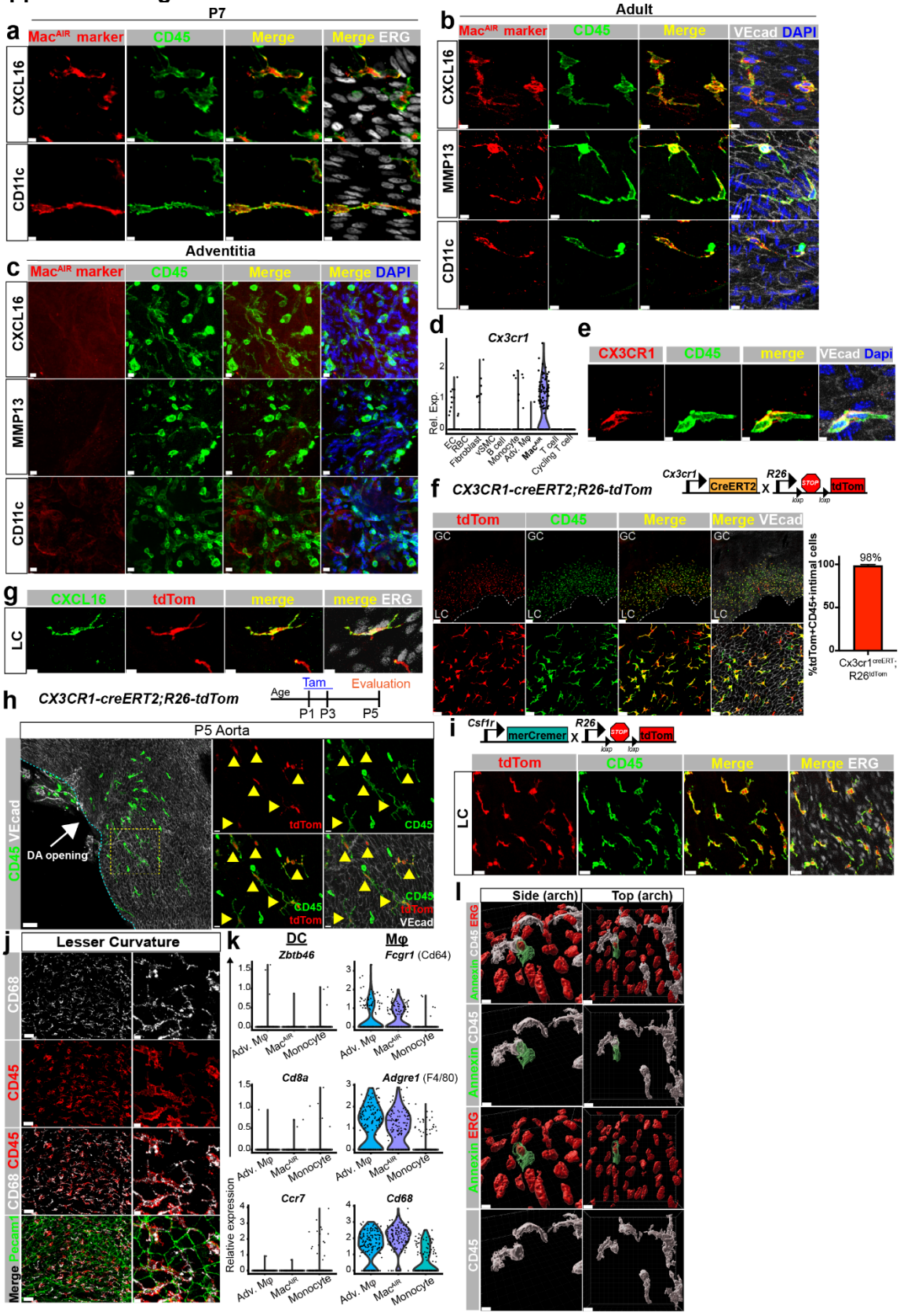

Supplemental Figure 4.5. Validation of MacAIR markers identified by scRNAseq

a, b, Validation of unique Mac^{AIR} genes using immunofluorescent staining in P7 (a) and adult (b) aortae. Mac^{AIR} markers in red (CXCL16 MMP13 and CD11c, as indicated in the figure) and CD45 in green. Scale bar, 5μm and 10μm, n=3-5. **c,** Evaluation of the same markers evaluated in panels **a** and **b,** but now in the adventitia. Note that no CD45+ cells in adult adventitia also expressed the Mac^{AIR} markers CXCL16, MMP13, and CD11c. Scale bar, 10μm; n=3 per marker. **d-e,** Mac^{AIRs} express Cx3cr1 at both the (**d**) transcript level and (**e**) protein level (in red) (Scale bar, 5μm, n=3). **f,** Inducible Cx3cr1-reporter model ($Cx3cr1^{creERT2}$;$R26^{tdTomato}$). *En face* images showing tdTomato reporter expression in intimal immune cells of the aortic arch after one-day post-tamoxifen injection in $Cx3cr1^{creERT2}$;$R26^{tdTomato}$ mice (Scale bar, 100μm and 30μm). One-day post-tamoxifen injection, 98% of intimal CD45+ cells found in the lesser curvature (LC) of the aortic arch in adult $Cx3cr1^{creERT2}$;$R26^{tdTomato}$ mice were tdTomato+; represented on adjacent graph (n=3, ± SD, GC, greater curvature). **g,** Intimal tdTomato+ cells colocalize with Mac^{AIR} marker Cxcl16, post-tamoxifen injection in $Cx3cr1^{creERT2}$;$R26^{tdTomato}$ aortae. Scale bar, 10μm, n=3. **h,** Intimal CD45+ cells found in P5 $Cx3cr1^{creERT2}$;$R26^{tdTomato}$ aortae were also labeled tdTomato+ (yellow arrowheads) after tamoxifen treatment at P1 and P3 (Scale bar, 50μm and 10μm, n=3). VE-Cadherin staining in white. (DA, Ductus arteriosus). **i,** $Csf1r^{merCremer}$;$R26^{tdTomato}$ macrophage fate-mapping model. Intimal CD45+ cells in the lesser curvature (LC) of the aortic arch labeled by tdTomato reporter. Adult mice received a single injection of tamoxifen. ERG staining in white. Scale bar, 20μm. **j,** *En face* images of the aortic arch co-staining for CD68 (while), CD45 (red) and VE-Cadherin (green). Different magnifications used to emphasize colocalization of immunofluorescence (Scale bar, 30μm and 7μm, n=3). **k,** Expression of known classical dendritic cell (DC) markers (*Zbtb46*, *Cd8a*, *Ccr7*) and macrophage (Mφ) markers (*Fcgr1*, *Adgre1*, *Cd68*) in adventitia macrophages (Adv. Mφ), intima-resident macrophages (Mac^{AIRs}), and monocytes from scRNA-seq data in Figure S2. **l,** 3D surface rendering of an intimal CD45+ cell (white) phagocytosing an annexin+ (green) endothelial cell (ERG+, red) in the lesser curvature of the aortic arch. Scale bar, 10μm.

Supplemental Figure 4.6

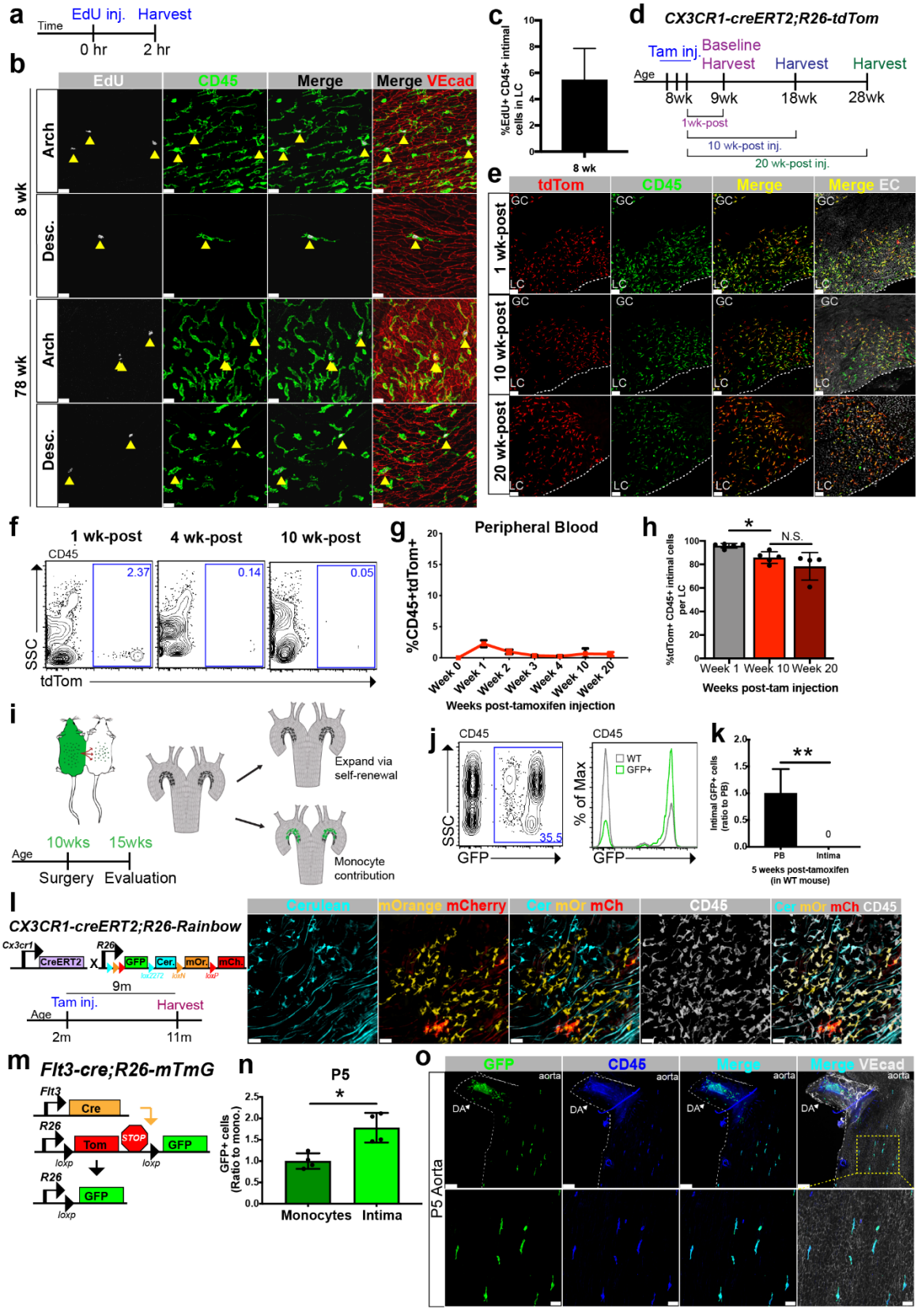

Supplemental Figure 4.6. Aortic intimal macrophages are a self-replicating cell population of the tunica intima residing in areas of disturbed flow.

a, Timeline of 5-Ethynyl-2′-deoxyuridine (EdU) incorporation assay. 8wk and 78wk old mice were injected with EdU and harvested 2-hrs later. **b,** EdU+(white) and CD45+ cells(green) co-expressing cells (yellow arrowheads) were easily detected in the aortae of 8wk and 78wk old mice (arch and descending=Desc.) upon short pulse (2hrs) with EdU. Scale bar, 20μm, n=3-8. **c,** Percentage of intimal EdU+ CD45+ cells found in the lesser curvature (LC) of the aortic arch in 8wk old C57BL/6 mice (n=3, ± SD). **d,** Experimental design for lineage tracing experiments. 8wk old $Cx3cr1^{creERT2}$;$R26^{tdTomato}$ mice were pulse-labeled by tamoxifen (Tam) injection (inj.). Mice were harvested at 1wk-post tamoxifen to assess baseline level of the reporter. Mice were also harvested after 10- and 20-wks post-tamoxifen to determine retention of reporter labeling in intimal immune cells. **e,** *En face* images demonstrated that the large majority of the intimal CD45+ cells (green) in the lesser curvature (LC) were also tdTomato+ at 1-, 10-, and 20-wks post-tamoxifen. Endothelial cell (EC) marker VE-cadherin (1- and 10-wk) and ERG (20-wk) were used (Scale bar, 80μm; n=4-5). GC= greater curvature. **f,** Representative fluorescence activated cell sorting (FACS) plot showing the frequency of tdTomato+ CD45+ cells found in the peripheral blood of $Cx3cr1^{creERT2}$;$R26^{tdTomato}$ mice weeks after tamoxifen injection. **g,** Percentage of peripheral blood cells positive for tdTomato during the time course of the study after injection of tamoxifen measured by flow cytometry (n= 3-5, ±SD). **h,** Percentage of intimal tdTomato+CD45+ cells found the aortic arch (LC) of $Cx3cr1^{creERT2}$;$R26^{tdTomato}$ mice at 1-, 10-, and 20-wks post-tamoxifen injection (n=4-5, Mann-Whitney *t*-test, ± SD, *p ≤ 0.05). **i,** Experimental design and timeline indicating the possible outcomes of the parabiosis experiment. GFP+ and wild-type (WT) mice were surgically paired together to share chimeric circulation for 5wks then aortae were analyzed. **j,** Representative FACS plot and histogram showing blood chimerism after parabiosis. **k,** Quantification of intimal GFP+ CD45+ cells found in the LC (lesser curvature) of the WT mice (n=2, Mann-Whitney *T*-test, ± SD, **p ≤ 0.01). PB= peripheral blood; WT= wild-type mice. **l,** Clonal tracing model, experimental design, and possible outcomes. 2month old $Cx3cr1^{creERT2}$;$R26^{Rainbow}$ were administered a single dosage of tamoxifen. At 11months (9 months later), aortae were harvested to evaluate clonal expansion (as per Rainbow transgenes) and retention of labeling of Mac^{AIRs} overtime. Images revealed clones of Mac^{AIRs} labeled with different fluorescent proteins and CD45 (white) 9months after tamoxifen labeling. Scale bar, 30μm; n=4. Cerulean (Cer), mOrange (mOr), mCherry (mCh). **m,** Lineage tracing model ($Flt3^{cre}$;$R26^{mTmG}$) that labels cells derived from definitive hematopoiesis. Flt3-driven cre recombinase (cre) expression leads to an irreversible switch from Tomato (tom)

to GFP expression in Flt3-expressing cells. As this is an irreversible switch, progeny will also be labeled GFP. **n,** GFP expression in CD45+ cells of P5 $Flt3^{cre}$;$R26^{mTmG}$ aortae relative to circulating monocytes (n= 4, Mann-Whitney *t*-test, ± SD, *p ≤ 0.05). **o,** *En face* images of P5 $Flt3^{cre}$;$R26^{mTmG}$ aortae showing GFP expression (green) of intimal CD45+ (blue) cells that exit from the ductus arteriosus (DA).

Supplemental Figure 4.7

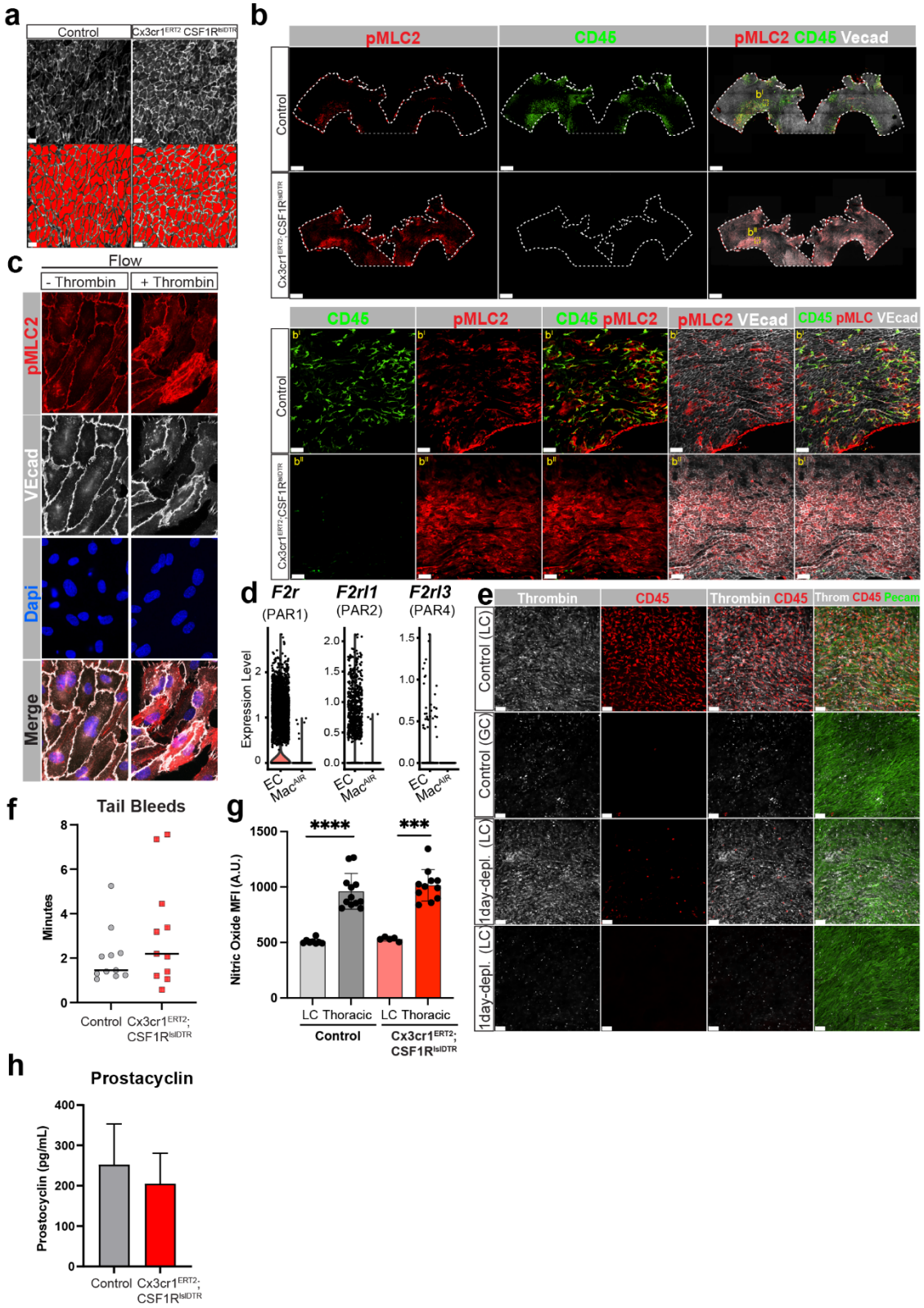

Supplemental Figure 4.7. Thrombin distribution and signaling in areas of disturbed flow

a, VE-cadherin staining (white) of control and macrophage-depleted (Cx3cr1^{creERT2};CSF1R^{lslDTR}) aortae (upper panel). Changes in cell area and cell number can be visualized and quantified by filling in red the area limited by VE-Cadherin staining. Note changes in shape and in cell number upon deletion of Mac^{AIRs} . Scale bar, 15μm. **b**, Low (upper panels) and high (lower panels) magnifications of control and Cx3cr1^{creERT2};CSF1R$^{lsl DTR}$ aortae staining for phosphorylation of myosin light chain 2 (pMLC2) (in red) and CD45 (green) one day post-diphtheria toxin injection. Scale bar, 500μm (upper panels), 50μm (lower panels); n=5. **c,** Effect of thrombin on human aortic endothelial cells (HAECs) pMLC2 (red) cultured in the presence of flow. VE-cadherin (white) provides information on cell shape. Dapi (blue) shows nuclei. **d,** *F2r* (PAR1), *F2rl1* (PAR2), and *F2rl3* (PAR4) expression in endothelial cells (EC) and in Mac^{AIRs} from the arch scRNAseq data sets (Figure S2). **e,** En face images of the lesser curvature (LC) and greater curvature (GC) staining for thrombin (white) in control and Cx3cr1^{creERT2};CSF1R$^{lsl DTR}$ aortae one-day post-diphtheria toxin injection (Scale bar, 50μm). **f**, Time of hemostatic plug formation was measured following transverse amputation of the tip of the tail (3mm) to assess hemostasis function in control and Cx3cr1^{creERT2};CSF1R$^{lsl DTR}$ mice one-day post-diphtheria toxin injection (n=11). **g**, *Ex vivo* mean fluorescent intensity (MFI) measurements of nitric oxide in the lesser curvature (LC) and thoracic aorta from control and Cx3cr1^{creERT2};CSF1R$^{lsl DTR}$ mice one-day post-diphtheria toxin injection (n=3; Mann-Whitney *T*-test, ± SD, ****p ≤ 0.0001). DAF-FM Diacetate (4-Amino-5-Methylamino-2',7'-Difluorofluorescein Diacetate) was used to detect and quantify nitric oxide. **h**, Plasma levels of prostacyclin in control and Cx3cr1^{creERT2};CSF1R$^{lsl DTR}$ mice one-day post-diphtheria toxin injection, measured by ELISA. No statistically significant changes noted (n=3-4, Mann-Whitney *t*-test, ± SD).

Supplemental Figure 4.8

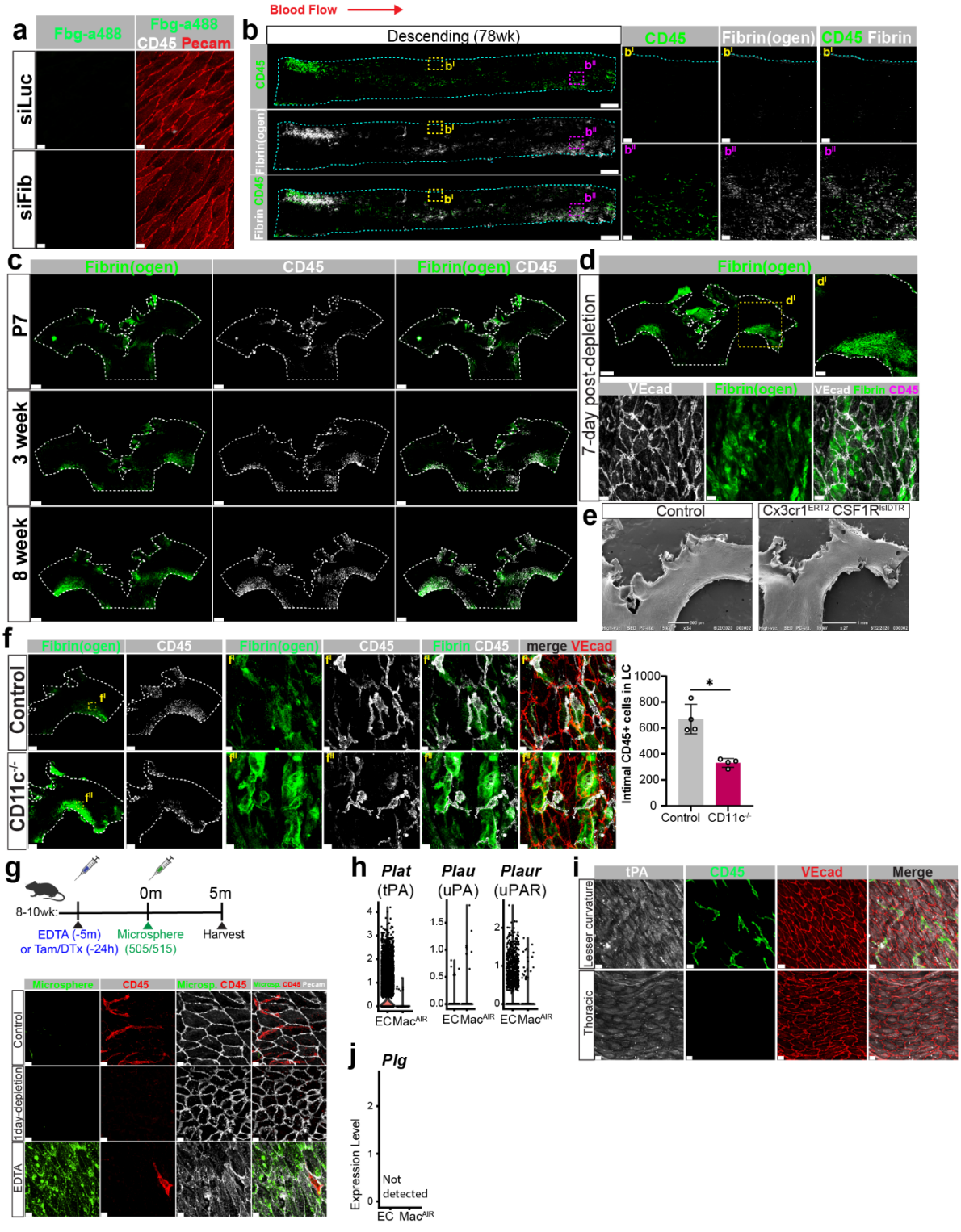

Supplemental Figure 4.8. MacAIRs are necessary to prevent fibrin accumulation in areas of turbulent flow.

a, *En face* images of the greater curvature of the aortic arch in mice that were treated with either siFibrinogen or siLuciferase (control) for 7 days and then additionally, treated with fibrinogen conjugated to a488 (Fbg-a488) intravenously for 3 hrs. No fibrinogen binds to the greater curvature (unlike in Fig 5f). Scale bar, 7μm. **b,** Aged descending aortae (78wk old) exhibit fibrin(ogen) deposition (white) in regions where intimal immune cells (CD45 in green) are concurrently found. Higher magnifications shown in b^{I} and b^{II}, right panels. Scale bars, 1000μm and 100μm ($b^{I\text{-}II}$), n=3. **c,** Time-course analysis shows progressive accumulation of fibrin(ogen) (in green) and intimal immune cells (CD45+ in white) in the aortic arch of C57BL/6 mice in P7, 3wk, and 8wk old mice. Scale bar, 300μm, n=3-20. **d,** Fibrin(ogen) accumulation (green) in $Cx3cr1^{creERT2}$;$CSF1R^{lsl DTR}$ mice after 7-days of continued macrophage depletion. Scale bar, 500μm, 150μm (d^{I}), and 8μm (bottom row). **e,** *En face* scanning electron microscopy images of aortae from control and $Cx3cr1^{creERT2}$;$CSF1R^{lsl DTR}$ mice after 14-days of continued macrophage depletion. **f,** *En face* images of the aortic arch comparing fibrin(ogen) accumulation (green) and immune cell (white) deposition in Control and $CD11c^{-/-}$ mice (Scale bar, 300μm and 8μm, n=4). Higher magnifications are shown (**f^{I} and f^{II}** panel series) on the right. Adjacent graph represents the total number of intimal CD45+ cells in the lesser curvature of control and $CD11c^{-/-}$ mice. (n=4, Mann-Whitney T-test, ± SD, *$p \leq 0.05$). **g**, Schema of littermate control (negative control) and $Cx3cr1^{creERT2}$;$CSF1R^{lsl DTR}$ mice that both received Tam/diphtheria toxin injections (24hr prior) and C57BL/6 EDTA treated mice (positive control). Treatment of anesthetized mice with EDTA was done 5min prior to injection of 40nm fluorescent microspheres. After 5min post-microsphere injection, mice were sacrificed and evaluated. High magnificent images of the three treatments shown in the panel below. Endothelial cells shown in white with VE-Cadherin staining, immune cells shown in red (CD45) and distribution of fluorescent microspheres are also shown. Scale bar, 7μm. **h,** *Plat* (tissue-type plasminogen activator, tPA)*, Plau* (Plasminogen activator, urokinase)*, and Plaur* (Plasminogen activator, urokinase receptor) expression in endothelial cells (EC) and Mac^{AIRs} from the arch and the aged descending A & B scRNAseq data sets in Supplementary Fig. 2. **i,** Immunostaining for tPA (white) in the lesser curvature of the aortic arch and in the thoracic aorta in relation to the location of CD45 cells (in green). Endothelial cells are visualized in red. Scale bar, 10μm. **j,** Expression of plasminogen (Plg) is undetected in endothelial cells and Mac^{AIRs} in scRNA-seq.

REFERENCES

1. Diacovo, T. G., Roth, S. J., Buccola, J. M., Bainton, D. F. & Springer, T. A. Neutrophil rolling, arrest, and transmigration across activated, surface-adherent platelets via sequential action of P-selectin and the beta 2-integrin CD11b/CD18. *Blood* **88,** 146–157 (1996).

2. Ley, K., Laudanna, C., Cybulsky, M. I. & Nourshargh, S. Getting to the site of inflammation: the leukocyte adhesion cascade updated. *Nat. Rev. Immunol.* **7,** 678–689 (2007).

3. Liew, P. X. & Kubes, P. The neutrophil's role during health and disease. *Physiol. Rev.* **99,** 1223–1248 (2019).

4. Mamdouh, Z., Chen, X., Pierini, L. M., Maxfield, F. R. & Muller, W. A. Targeted recycling of PECAM from endothelial surface-connected compartments during diapedesis. *Nature* **421,** 748–753 (2003).

5. Gisterå, A. & Hansson, G. K. The immunology of atherosclerosis. *Nat. Rev. Nephrol.* **13,** 368–380 (2017).

6. Quintar, A. *et al.* Endothelial protective monocyte patrolling in large arteries intensified by western diet and atherosclerosis. *Circ. Res.* **120,** 1789–1799 (2017).

7. Libby, P., Nahrendorf, M. & Swirski, F. K. Leukocytes link local and systemic inflammation in ischemic cardiovascular disease: an expanded "cardiovascular continuum". *J. Am. Coll. Cardiol.* **67,** 1091–1103 (2016).

8. Robbins, C. S. *et al.* Local proliferation dominates lesional macrophage accumulation in atherosclerosis. *Nat. Med.* **19,** 1166–1172 (2013).

9. Ross, R. Rous-Whipple Award Lecture. Atherosclerosis: a defense mechanism gone awry. *Am. J. Pathol.* **143,** 987–1002 (1993).

10. Auffray, C. *et al.* Monitoring of blood vessels and tissues by a population of monocytes with patrolling behavior. *Science* **317,** 666–670 (2007).

11. Carlin, L. M. *et al.* Nr4a1-dependent Ly6C(low) monocytes monitor endothelial cells and orchestrate their disposal. *Cell* **153,** 362–375 (2013).

12. Hanna, R. N. *et al.* Patrolling monocytes control tumor metastasis to the lung. *Science* **350,** 985–990 (2015).

13. Choi, J.-H. *et al.* Identification of antigen-presenting dendritic cells in mouse aorta and cardiac valves. *J. Exp. Med.* **206,** 497–505 (2009).

14. Jongstra-Bilen, J. *et al.* Low-grade chronic inflammation in regions of the normal mouse arterial intima predisposed to atherosclerosis. *J. Exp. Med.* **203,** 2073–2083 (2006).

15. Williams, J. W. *et al.* Limited proliferation capacity of aortic intima resident macrophages requires monocyte recruitment for atherosclerotic plaque progression. *Nat. Immunol.* **21,** 1194–1204 (2020).

16. Broadhouse, K. M. *et al.* Assessment of PDA shunt and systemic blood flow in newborns using cardiac MRI. *NMR Biomed.* **26,** 1135–1141 (2013).

17. Colucci-Guyon, E. *et al.* Mice lacking vimentin develop and reproduce without an obvious phenotype. *Cell* **79,** 679–694 (1994).

18. Salvador, J., Hernandez, G.E., Ma, F., Abrahamson C.,

& Iruela-Arispe, M.L. Absence of the intermediate filament results in patent ductus arteriosus (2021).

19. Ma, F., Hernandez, G. E., Romay, M. & Iruela-Arispe, M. L. Single-cell RNA sequencing to study vascular diversity and function. *Curr Opin Hematol* (2021). doi:10.1097/MOH.0000000000000651

20. McDonald, A. I. *et al.* Endothelial Regeneration of Large Vessels Is a Biphasic Process Driven by Local Cells with Distinct Proliferative Capacities. *Cell Stem Cell* **23,** 210–225.e6 (2018).

21. Ensan, S. *et al.* Self-renewing resident arterial macrophages arise from embryonic CX3CR1(+) precursors and circulating monocytes immediately after birth. *Nat. Immunol.* **17,** 159–168 (2016).

22. Chakarov, S. *et al.* Two distinct interstitial macrophage populations coexist across tissues in specific subtissular niches. *Science* **363,** (2019).

23. Lim, H. Y. *et al.* Hyaluronan Receptor LYVE-1-Expressing Macrophages Maintain Arterial Tone through Hyaluronan-Mediated Regulation of Smooth Muscle Cell Collagen. *Immunity* **49,** 326–341.e7 (2018).

24. Hernandez, G. E. & Iruela-Arispe, M. L. The many flavors of monocyte/macrophage--endothelial cell interactions. *Curr Opin Hematol* **27,** 181–189 (2020).

25. Tabula Muris Consortium *et al.* Single-cell transcriptomics of 20 mouse organs creates a Tabula Muris. *Nature* **562,** 367–372 (2018).

26. Satpathy, A. T. *et al.* Zbtb46 expression distinguishes classical dendritic cells and their committed progenitors from other immune lineages. *J. Exp. Med.* **209,** 1135–1152 (2012).

27. Epelman, S., Lavine, K. J. & Randolph, G. J. Origin and functions of tissue macrophages. *Immunity* **41,** 21–35 (2014).

28. Ginhoux, F. & Guilliams, M. Tissue-Resident Macrophage Ontogeny and Homeostasis. *Immunity* **44,** 439–449 (2016).

29. Serbina, N. V. & Pamer, E. G. Monocyte emigration from bone marrow during bacterial infection requires signals mediated by chemokine receptor CCR2. *Nat. Immunol.* **7,** 311–317 (2006).

30. Boyer, S. W., Schroeder, A. V., Smith-Berdan, S. & Forsberg, E. C. All hematopoietic cells develop from hematopoietic stem cells through Flk2/Flt3-positive progenitor cells. *Cell Stem Cell* **9,** 64–73 (2011).

31. Epelman, S. *et al.* Embryonic and adult-derived resident cardiac macrophages are maintained through distinct mechanisms at steady state and during inflammation. *Immunity* **40,** 91–104 (2014).

32. Mehta, D. & Malik, A. B. Signaling mechanisms regulating endothelial permeability. *Physiol. Rev.* **86,** 279–367 (2006).

33. Rigor, R. R., Shen, Q., Pivetti, C. D., Wu, M. H. & Yuan, S. Y. Myosin light chain kinase signaling in endothelial barrier dysfunction. *Med Res Rev* **33,** 911–933 (2013).

34. Austin, K. M., Covic, L. & Kuliopulos, A. Matrix metalloproteases and PAR1 activation. *Blood* **121,** 431–439 (2013).

35. Hou, H.-H. *et al.* MMP-12 activates protease-activated receptor-1, upregulates placenta growth factor, and leads to pulmonary emphysema. *Am. J. Physiol. Lung Cell Mol. Physiol.* **315,** L432–L442 (2018).

36. Jaffré, F., Friedman, A. E., Hu, Z., Mackman, N. & Blaxall, B. C. β-adrenergic receptor stimulation transactivates protease-activated receptor 1 via matrix metalloproteinase 13 in cardiac cells. *Circulation* **125,** 2993–3003 (2012).

37. Willis Fox, O. & Preston, R. J. S. Molecular basis of protease-activated receptor 1 signaling diversity. *J. Thromb. Haemost.* **18,** 6–16 (2020).

38. Kulkarni, J. A., Witzigmann, D., Chen, S., Cullis, P. R. & van der Meel, R. Lipid Nanoparticle Technology for Clinical Translation of siRNA Therapeutics. *Acc. Chem. Res.* **52,** 2435–2444 (2019).

39. Bugge, T. H. *et al.* Loss of fibrinogen rescues mice from the pleiotropic effects of plasminogen deficiency. *Cell* **87,** 709–719 (1996).

40. Prasad, J. M. *et al.* Mice expressing a mutant form of fibrinogen that cannot support fibrin formation exhibit compromised antimicrobial host defense. *Blood* **126,** 2047–2058 (2015).

41. Motley, M. P. *et al.* A CCR2 macrophage endocytic pathway mediates extravascular fibrin clearance in vivo. *Blood* **127,** 1085–1096 (2016).

42. Bonnardel, J. *et al.* Stellate cells, hepatocytes, and endothelial cells imprint the kupffer cell identity on monocytes colonizing the liver macrophage niche. *Immunity* **51,** 638–654.e9 (2019).

43. Sakai, M. *et al.* Liver-Derived Signals Sequentially Reprogram Myeloid Enhancers to Initiate and Maintain Kupffer Cell Identity. *Immunity* **51,** 655–670.e8 (2019).

44. Scott, C. L. *et al.* Bone marrow-derived monocytes give rise to self-renewing and fully differentiated Kupffer cells. *Nat. Commun.* **7,** 10321 (2016).

45. Colvin, R. B. & Dvorak, H. F. Fibrinogen/fibrin on the surface of macrophages: detection, distribution, binding requirements, and possible role in macrophage adherence phenomena. *J. Exp. Med.* **142,** 1377–1390 (1975).

46. Hiller, O., Lichte, A., Oberpichler, A., Kocourek, A. & Tschesche, H. Matrix metalloproteinases collagenase-2, macrophage elastase, collagenase-3, and membrane type 1-matrix metalloproteinase impair clotting by degradation of fibrinogen and factor XII. *J. Biol. Chem.* **275,** 33008–33013 (2000).

47. Motterle, A. *et al.* Influence of matrix metalloproteinase-12 on fibrinogen level. *Atherosclerosis* **220,** 351–354 (2012).

48. Tardif, G., Reboul, P., Pelletier, J.-P. & Martel-Pelletier, J. Ten years in the life of an enzyme: the story of the human MMP-13 (collagenase-3). *Mod Rheumatol* **14,** 197–204 (2004).

49. Bugge, T. H., Flick, M. J., Daugherty, C. C. & Degen, J. L. Plasminogen deficiency causes severe thrombosis but is compatible with development and reproduction. *Genes Dev.* **9,** 794–807 (1995).

50. Goguen, J. D., Bugge, T. & Degen, J. L. Role of the pleiotropic effects of plasminogen deficiency in infection experiments with plasminogen-deficient mice. *Methods* **21,** 179–183 (2000).

51. Gomez Perdiguero, E. *et al.* Tissue-resident macrophages originate from yolk-sac-derived erythro-myeloid progenitors. *Nature* **518,** 547–551 (2015).

52. Hoeffel, G. *et al.* C-Myb(+) erythro-myeloid progenitor-derived fetal monocytes give rise to adult tissue-resident macrophages. *Immunity* **42,** 665–678 (2015).

53. Schulz, C. *et al.* A lineage of myeloid cells independent of Myb and hematopoietic stem cells. *Science* **336,** 86–90 (2012).

54. Yona, S. *et al.* Fate mapping reveals origins and dynamics of monocytes and tissue macrophages under homeostasis. *Immunity* **38,** 79–91 (2013).

55. Strilchuk, A. W. *et al.* Sustained depletion of FXIII-A by inducing acquired FXIII-B deficiency. *Blood* **136,** 2946–2954 (2020).

56. Korsunsky, I. *et al.* Fast, sensitive and accurate integration of single-cell data with Harmony. *Nat. Methods* **16,** 1289–1296 (2019).

57. Ali, S. R. *et al.* Developmental heterogeneity of cardiac fibroblasts does not predict pathological proliferation and activation. *Circ. Res.* **115,** 625–635 (2014).

58. Navab, M. *et al.* Monocyte migration into the subendothelial space of a coculture of adult human aortic endothelial and smooth muscle cells. *J. Clin. Invest.* **82,** 1853–1863 (1988).

59. Rinkevich, Y., Lindau, P., Ueno, H., Longaker, M. T. & Weissman, I. L. Germ-layer and lineage-restricted stem/progenitors regenerate the mouse digit tip. *Nature* **476,** 409–413 (2011).

Chapter 5. Aortic intima-resident macrophages are anchored to the endothelium through multiple receptor/ligand pairs that are affected upon SARS-CoV-2 infection

ABSTRACT

Endothelial cells provide a non-thrombogenic surface facilitating blood circulation. However, in areas of disturbed and oscillatory blood flow, like the lesser curvature of the aortic arch and branch openings, this function is challenged by the accumulation of fibrinogen and thrombin. Therefore, intima-resident macrophages (Mac^{AIRs}) are summoned to these areas of disturbed flow from birth and are critical to effectively clear fibrin(ogen) and prevent intravascular clotting. Here, we show that disturbed flow creates a unique endothelial niche that requires multiple receptor-ligand pairs, including Icam-1, Vcam-1, CD11c, and Pecam-1, to allow for the adhesion and intimate association of the Mac^{AIRs} to the endothelium. Additionally, we found that Mac^{AIRs} can become detached during SARS-CoV-2 infection in rhesus macaques, leading to the accumulation of fibrin(ogen), fibrin fibers, microthrombi, and endothelial rupture.

INTRODUCTION

Endothelial cells provide a non-thrombogenic blood-tissue interface facilitating blood circulation. However, this function is challenged by the accumulation of fibrinogen and thrombin in areas of disturbed and oscillatory blood flow, like the lesser curvature of the aortic arch and branch openings. Recently, an intima-resident macrophage population (Mac^{AIRs}) was identified in regions of disturbed blood flow in healthy aortae (Hernandez et al. 2021). This distinct macrophage population seeds the aorta immediately post-birth due to hemodynamic changes and is self-maintained throughout adulthood, populating regions of disturbed flow, like the lesser curvature of the aortic arch. This unique macrophage population is intimately interwoven within the endothelium, but without hindering the barrier integrity (Hernandez et al. 2021). Mac^{AIRs} are essential to clear fibrin(ogen) deposits, prevent fibrin formation, and maintain an anti-thrombotic

state in areas of disturbed flow. Additionally, these macrophages are responsible for preventing thrombin-mediated activation of protease-activated receptors (PAR) receptors on the endothelium, preserving the integrity of endothelial junctions. The anatomical location of these macrophages in relation to the endothelial cells is peculiar and raises multiple questions, but more importantly: how these intimal macrophages anchor and co-exist with the endothelium. Moreover, what happens to these macrophages during pathology, and could they play a role in systemic conditions that are associated with coagulopathy and intravascular thrombosis?

Here, we show using several *in vivo* models that disturb flow creates a unique endothelial niche that requires multiple receptor-ligand pairs to allow for the adhesion of Mac^{AIRs} in these regions. Icam1-/- mice treated with Vcam-1 neutralizing antibody as well as CD11c-/- mice showed a robust reduction of Mac^{AIRs}; however, insufficient to fully deplete Mac^{AIRs} from the endothelium, indicating more factors are involved. We also found that Mac^{AIRs} express Pecam-1, supporting the possibility that Mac^{AIRs} could bind to the endothelium via homophylic-heterotypic interactions. Overall, these findings indicate that Mac^{AIRs} bind to the endothelium through many receptor-ligand pairs to guarantee their retention and topology to the vascular wall, and their physiological need to ensure the homeostasis of the endothelium in regions of disturbed blood flow. Additionally, we found that infection of SARS-CoV-2 in rhesus macaques lead to the detachment of the intimal myeloid population in the aorta, resulting in the accumulation of fibrin(ogen), fibrin fibers, microthrombi, and endothelial rupture.

RESULTS

Mechanical forces are responsible for an endothelial niche that seeds intimal macrophages

The conspicuous distribution of Mac^{AIRs} in areas of disturbed flow suggested that alterations unique to those regions might be responsible for their anchorage. In fact, disturbed flow significantly alters endothelial cell expression, including upregulation of Icam-1 and Vcam-1 (Chiu

and Chien, 2011; Nakashima et al., 1998). Interestingly, high levels of Icam-1 and Vcam-1 can be detected immediately post-birth in the lesser curvature correlating with changes in hemodynamics and the accumulation of Mac^{AIRs} (**Figures 5.1A, Supplemental Fig. 5.1A, B**). We additionally performed scRNA-seq on E18.5 and P5 aortae and compare their transcriptome to endothelial cells isolated from the aortic arch of 8wk old mice **(Figures 5.1B-D, Supplemental Fig. 5.1C-E**). *Icam1* and *Vcam1* transcripts were increased in the endothelium after birth (**Figure 5.1D**). *Cx3cl1* (fractalkine) expression, the ligand to *Cx3cr1*, was also increased post-birth (**Figure 5.1D**), further indicating that hemodynamic changes after the closure of the ductus arteriosus create a unique endothelial-permissive environment for interactions with inflammatory cells in regions of turbulent flow. To mechanistically determine whether Icam-1 or Vcam-1 were necessary for the anchorage of Mac^{AIRs}, we evaluated $Icam1^{-/-}$ mice and mice exposed to Vcam-1 neutralizing antibodies (nAbs) for 3-days (as genomic Vcam-1 deletion is embryonically lethal). Both $Icam\text{-}1^{-/-}$ mice and wild-type mice treated with Vcam-1 nAbs showed a significant decrease in total number of Mac^{AIRs} (**Figure 5.1E**). Additionally, $Icam\text{-}1^{-/-}$ mice treated with Vcam-1 nAb showed a robust reduction; however, insufficient to fully deplete the Mac^{AIRs} from the endothelium, indicating that more factors might be involved.

We previously determined that Mac^{AIRs} expressed high levels of CD11c (Hernandez et al. 2021), whose known ligands include Icam-1, Icam-2, Icam-4, and fibrin(ogen). Therefore, using CD11c-deficient mice ($CD11c^{-/-}$), we tested the hypothesis that CD11c might be required to support Mac^{AIRs} accumulation/anchorage to the endothelium, within the aorta, in regions of turbulent flow. Indeed, $CD11c^{-/-}$ mice showed a significant reduction in the number of Mac^{AIRs} (**Figure 5.1F**) indicating that CD11c was necessary, albeit not fully sufficient, for the retention of Mac^{AIRs} to the intimal niche. An additional candidate for the anchorage of Mac^{AIRs} was Pecam-1, as scRNA-seq analysis indicated transcript expression (**Figure 5.1G**), which we validated with immunocytochemistry previously (Hernandez et al. 2021), supporting the possibility that Mac^{AIRs} could bind to the endothelium via homophylic-heterotypic interactions. Overall, these findings

indicate that disturbed flow creates a unique endothelial niche that requires multiple receptor-ligand pairs to allow for the adhesion of Mac^{AIRs} in these regions (**Figure 5.1H**).

Mac$^{AIR's}$ role in the pathogenesis of SARS-CoV-2

As Mac^{AIRs} play an essential role in clearing fibrin(ogen) deposits and maintaining a non-thrombogenic intravascular surface in regions of disturbed flow (Hernandez et al. 2021), we were interested in understanding how these cells function in disease settings. A few systemic viral conditions, including COVID-19 have been associated with coagulopathy and intravascular thrombosis (Aid et al., 2020; Teuwen et al., 2020). Rhesus macaques, unlike mice, can be infected with SARS-CoV-2. Additionally, we found rhesus macaques have an abundant intimal CD68+ myeloid population whose dendritic-like morphology resembled that of Mac^{AIRs} found in mice. Furthermore, we noted nominal fibrin(ogen) deposition as well as fibrin(ogen) associated with the intimal CD68+ myeloid population (**Figure 5.2A**) Thus, we explored whether Mac^{AIRs} could partake in the pathogenesis of SARS-CoV-2 infection in rhesus macaques challenged with SARS-CoV-2 for either 3 or 9 days (**Figure 5.2B**). The aortae of uninfected controls showed nominal fibrin(ogen) deposition and intimal myeloid cells accumulation (**Figures 5.2B and 5.2C**). In contrast, SARS-CoV-2 rhesus macaques, displayed abundant accumulation of fibrin networks decorating the lesser curvature of the arch (**Figures 5.2B and 5.2C**) with rounded and sporadic immune cells (**Figures 5.2B and 5.2C**). Of note, no fibrin(ogen) or intimal immune cells were found in the greater curvature of the aortic arch in either control or SARS-CoV-2 challenged macaques (**Figure 5.2D**). Interestingly, our scRNAseq does not detect Ace2 in Mac^{AIRs} or the aortic arch endothelial cells (data not show). Finally, rhesus macaques infected with SARS-CoV-2 for 9-days, showed massive fibrin fibers, microthrombi, and endothelial rupture (**Figure 5.2E**). Taken together, our findings indicate that Mac^{AIRs} are required to clear fibrin(ogen) deposits, prevent fibrin formation, and maintain an anti-thrombotic state in areas of turbulent flow.

DISCUSSION

Our findings indicate that endothelial cells, conditioned by disturbed flow, provide a conducive niche for differentiation of Mac^{AIRs}. We also found that the interactions between endothelial cells and Mac^{AIRs} requires Icam-1,Vcam-1, CD11c, and Pecam-1. Importantly, while not initially expressed by endothelium in laminar flow regions, Icam-1 is known to be increased with age, providing a possible critical molecular mechanism for the presence of Mac^{AIRs} in the descending aorta of older mice. The data presented here underscores the need for multiple receptor-ligand pairs for adequate adhesion and intimate association of Mac^{AIRs} to the endothelium.

Since the Ace2 receptor, site of entry for SARS-CoV-2, is not expressed by Mac^{AIRs} nor it is found on endothelial cells in the aortic arch, we speculate that the detachment of the intimal myeloid cells in the Rhesus Macaque aortae is an indirect consequence of the SARS-CoV-2 infection. A possible explanation is that the sequestration of the Ace2 receptor by viral proteins that stimulate the kallikrein-bradykinin renin-angiotensin pathways, lead to an increase in the levels of bradykinin and cleaved high-molecular-weight-kininogen (HKa). Combined these two molecules promote increases in vascular permeability and deleterious effects on the immune system (Garvin et al. 2020). In turn, Hka has been shown to impair the interactions of leukocytes with endothelial cells (Khan et al. 2006), as well as displace fibrinogen from macrophages due to its high affinity for CD11c. Consequently, Hka exerts an anti-adhesive effect on endothelial-monocyte/macrophage interactions (Gustafson et al. 1989). Therefore, it is likely that high circulating levels of HKa could challenge endothelial cell- Mac^{AIRs} interactions, leading to the displacement of intimal macrophages and thereby resulting in fibrin(ogen) accumulation and microthrombi formation.

Alternatively, a recent study showed that intimal myeloid cells in mouse aortae undergo reverse transendothelial migration with systemic stimulation of Toll-like-receptors (TLRs) (Roufaiel et al 2016). In that paper, the authors argue that the reverse transendothelial migration

of the intimal myeloid cells induces clearance of viral and bacterial infections without a local inflammatory response or the requirement for adaptive immunity. Specifically, they look at *Chlamydia muridarum*, since macrophages transport *Chlamydia pneumonia* from the lungs to regional lymph nodes and circulating monocytes disseminate infection to other tissues. Through this mechanism, the authors speculate that monocytes could provide a potential alternative route for intimal infection. Unfortunately, the long-term consequences of constant viral or bacterial infections was never assessed, nor has the impact of chronic reverse transendothelial migration of intimal myeloid cells on fibrin(ogen) accumulation and microthrombi formation evaluated. One could speculate that during SARS-CoV-2 infection, monocytes disseminate infection to the arterial wall by promoting reverse transendothelial migration of the intimal-resident myeloid population to clear the infection. In turn, the process results in displacement of intimal myeloid cells and fibrin accumulation in regions of disturbed flow in SARS-CoV-2 infected aortae.

Rhesus macaques infected with SARS-CoV-2 for 9-days showed depletion of intimal myeloid cells, massive fibrin fibers, microthrombi, and endothelial rupture. The relevance of this endothelial-macrophage partnership cannot be overstated as per the devastating intravascular clotting sequelae associated with COVID19. The question as to how this newly found system is functioning in situations of vascular coagulopathies of unknown cause (non-associated with platelets or coagulation factor levels) is an open important avenue to now be followed. These future studies could lead to potential therapies that address the vascular system dysfunction and may have important role in treating SARS-CoV-2 infection and its long-lasting effects.

ACKNOWLEDGEMENTS

We are also thankful to William Mueller for Pecam1 antibodies. A special thanks to Michelle Steel and Snezana Mirkov for managing animal colonies and for assistance with husbandry and animal experiments. We thank the members of the Arispe lab and the Feinberg Cardiovascular and Renal

Research Institute at Northwestern University for extensive discussions. Illustrations were created with BioRender.com.

METHODS

Animal Models

Mice

All animal procedures were approved and performed in accordance with the UCLA and Northwestern University Institutional Animal Care and Use Committee. C57BL/6J (#000664) and Icam1-/- (#002867) mice were purchased from Jackson Laboratories. CD11c-/- mice were a gift from Matthew Flick at UNC Chapel Hill. All mouse strains were maintained on a C57BL/6J background. Mice were genotyped using Transnetxy. Males and females were used in approximately equal numbers for all experiments. For the E18.5 and P5 aortae data sets, both sexes were used (littermates). Unless specified, all adult mice used were 8-10wks of age.

Rhesus macaques

Ethics Statement: In total, 5 macaques (*Macaca mulatta*) were utilized for this study. 4 macaques were housed at the Tulane National Primate Research Center (TNPRC, Covington, LA) and 1 macaque at Bioqual, Inc. (Rockville, MD) in accordance with the "Guide for the Care and Use of Laboratory Animals". Both the TNPRC and Bioqual, Inc. are fully accredited by the Association for Assessment and Accreditation of Laboratory Animal Care International. All primate studies at TNPRC were reviewed and approved by the Tulane University Institutional Animal Care and Use Committee (IACUC) under protocol numbers P0452 and P0447. All primate studies at Bioqual were reviewed and approved by the Bioqual, Inc. IACUC under protocol number 20-V865-052P.

At TNPRC, 3 animals were inoculated with $1.1x10^5$ plaque forming units (PFU) of the WA1 strain of SARS-CoV2 via intranasal (1mL) and intratracheal (1mL) routes. On days 8 (n=1) and 9 (n=2) post-infection, macaques were necropsied and aortal tissues were collected. Additionally, 1 uninfected, control animal was also necropsied with aortal tissues collected. At Bioqual, Inc. 1 animal was inoculated with $1.1x10^5$ PFU of the WA1 strain of SARS-CoV2 via intranasal (1mL) and intratracheal (1mL) routes. This animal was necropsied 3 days post-infection with aortal tissues collected. All tissues upon removal were placed into 4% PFA with infected tissues remaining in a BSL3 environment for at least 3 days following collection. Afterwards, all samples were shipped overnight to Northwestern University.

Aorta *en face* harvest

Adult mice were injected intra-peritoneal with 10mg of methacholine for smooth muscle cell relaxation that helps lay aortae flat for *en face* imaging. Immediately after injection, adult mice were sacrificed and perfused with 10mLs of 2% paraformaldehyde (PFA) through the left ventricle (for embryos and neonates, we perfused 0.5-3mLs of 2% PFA). Following perfusion, the aorta was removed from the mouse and the adventitia was carefully removed under a dissecting microscope. The aortae were opened longitudinally and transferred to a 35mm silicon-coated dish filled with 2% PFA. The aorta sheet was then pinned to lay flat, exposing the endothelium. Fixation proceeded for one additional hour at 4^{o}C followed by washes in phosphate buffered saline (PBS).

Aortic *en face* immunostaining

For immunostaining, mouse and rhesus macaque aortae were washed 3 times with 1X HBSS and then incubated in blocking/permeabilization buffer (0.3% Triton-X, 0.5% Tween-20, 3% Normal Donkey Serum) for 1hr at room temperature. Primary antibody cocktail was prepared in the blocking/permeabilization buffer and incubated overnight at 4^{o}C (endothelial marker ERG, VE-cadherin, or Pecam1 were always used in conjunction with other markers in order to label the endothelium). The following day aortae were washed three times with 1X HBSS and incubated with secondary antibodies with DAPI for 1hr at room temperature. After final set of washes in 1X HBSS, aortas were mounted on glass slides with prolong gold without DAPI (cat# P36930). Primary antibodies: CD45 (BD #550539), fibrinogen (Abcam #ab10900171), Icam-1 (Biolegend #116102), Vcam-1 (BD #550547), ERG (Abcam #ab92513), Pecam1(2H8, gift from William Mueller Laboratory, NU).

Aortic *en face* imaging and image processing

Stained aortae were mounded on glass slides with lumen facing the coverslip. For rhesus macaque aortae, imaging spacers (Grace Bio-Labs, #654006-S) were used to help mount the thicker tissue. Aortae were imaged using either an LSM880 confocal microscope (ZEISS) or an A1R HD25 confocal microscope (Nikon). Z-stack and tile scan features were used to image the large, wavy surfaces of the aortae. The resulting tiles were then stitched into a single large image (ZEN 2.0 Black software, ZEISS or NIS-Elements, Nikon), which enabled the visualization of the large aortic arch with high resolution. Imaris software (Imaris 9.5.1 and 9.7.0 Bitplane) was used to visualize images in 3D. Additionally, Denoise.AI (Nikon) was employed to

remove Poisson shot noise in certain images. Images were acquired using either 20x or 63x oil objective.

scRNA-seq

For cell isolation in E18.5 and P5 aortae, fetus and neonates were sacrificed and aortae were dissected in versene. Following dissection, aortae were minced into small pieces and placed in 1mL of digestion buffer containing DNase1, 1M HEPES, Liberase, and HBSS at 37^{o}C for 20mins. Once tissue was digested into a single cell suspension, the reaction was neutralized with sc-HBSS and centrifuged for 5 min at 300g. Cells were passed through a 40μm filter and final cell suspension was in 0.04%BSA. To obtain sufficient cell numbers, 8 (E18.5) and 9 (P5) aortae were used per library (littermates).

scRNA-seq libraries were generated using 10X Genomics Chromium Single Cell 3' Library & Gel Bead Kit v2 (8wk arch & aged descending (78wk) A,B) and v3 (E18.5 and P5 aortae). Cells were loaded accordingly following the 10X Genomics protocol with an estimated targeted cell recovery of 5000 cells. Sequencing was performed on Illumina HiSeq4000 (Pair-end, 100 base pairs per read, 8wk arch & aged descending A,B) and NovaSeq6000 (E18.5 and P5 aortae). The digital expression matrix was generated by demultiplexing, barcode processing, and gene unique molecular index counting using the Cellranger count pipeline (version 4.0.0, 10X Genomics). Multiple samples were merged using the Cellranger aggr pipeline. To identify different cell types and find signature genes for each cell type, the R package Seurat (version 3.1.2) was used to analyze the digital expression matrix. Specifically, cells that express <100 genes or <500 transcripts were filtered out. Variable genes were selected using the FindVariableGenes function for further analysis. The data were normalized using the NormalizeData function with a scale factor 10,000. The genes were then scaled and centered using the ScaleData function. Principal component analysis (PCA), *t*-distributed stochastic neighbor embedding (t-SNE) and Uniform Manifold Approximation and Projection (UMAP) were used to reduce the dimensionality of the data. In the aggregated analysis of arch, E18.5 and P5 aortae, Harmony was used to remove potential batch effects with the Seurat function RunHarmony. Cell clusters were identified using the FindClusters function. The cluster marker genes were found using the FindAllMarkers function. Cell types were annotated based on the cluster marker genes. Heatmaps, violin plots and gene expression plots were generated by DoHeatmap, VlnPlot, FeaturePlot functions, respectively.

***In vivo* Vcam-1 inhibition**

C57BL/6 mice were intravenously injected with Vehicle (IgG) or Vcam-1 neutralizing antibody (Bio X cell #BE0027) for 3-days. Mice were then sacrificed and the aortae were analyzed for Mac^{AIR} accumulation.

QUANTIFICATION AND STATISTIAL ANALYSIS

Treatments were randomized; investigators were blinded to allocation for outcome assessment.

Quantification of intimal immune cells in aortae was done using the spots function in Imaris 9.5.1 or 9.7.0 (Bitplane) on maximum intensity Z-projections. Only cells with clearly distinguishable bodies and nuclei (DAPI, not shown) were quantified.

Data was calculated as the mean for at least three independent samples, where error bars represent the standard deviation of the mean (for details, see legends). To determine whether two datasets were significantly different, we calculated P values with unpaired, non-parametric student's *t*-test followed by Mann-Whitney test; $P < 0.05$ was considered significant and $P < 0.05$, 0.01, 0.001 and 0.0001 were represented by *,**,***, and ****. Statistical analyses were performed with Excel (Microsoft Office) or Prism 8 (GraphPad Software).

FIGURES

Figure 5.1

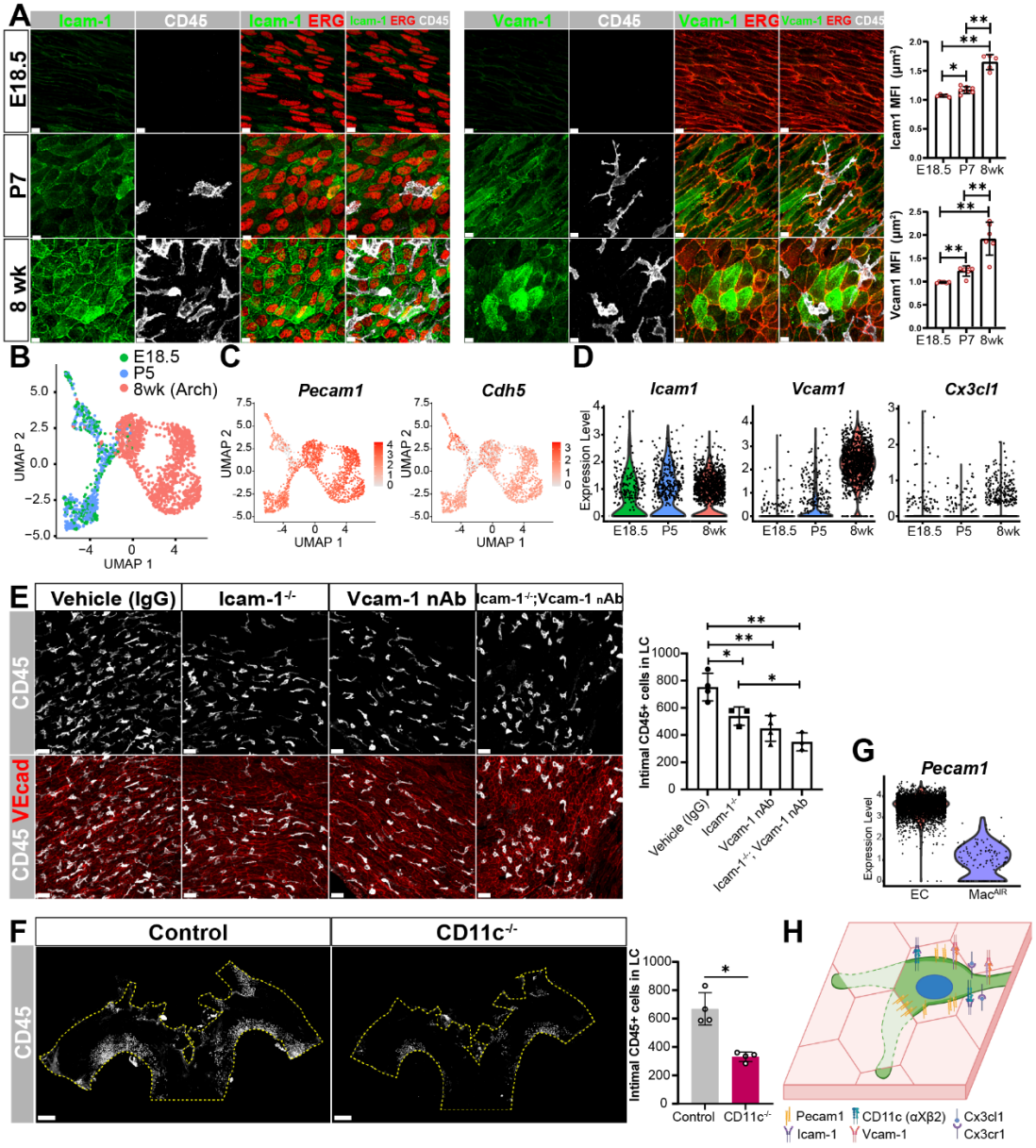

Figure 5.1 Turbulent-flow induction of Icam-1 and Vcam-1 in the endothelium is necessary for recruitment and retention of MacAIRs

(A) *En face* images stained for Icam-1 or Vcam-1 in the lesser curvature of E18.5, P7, and 8wk old aortae (Scale bar, 7μm). Mean fluorescent intensity (MFI) of Icam-1 and Vcam-1 were determined in areas of the lesser curvature and normalized to areas of the greater curvature (GC) (n=3-6, Mann-Whitney T-test, ± SD, *p ≤ 0.05, **≤ 0.01). See also Figure S6A and S6B.

(B) UMAP plot of the endothelial cells captured from three independent scRNAseq libraries:

E18.5, P5, and 8wk (arch, Extended Data Fig. 3) old aortae. See also Figure S6C-6E. **(C)** Expression of *Pecam1* and *Cdh5* denotes endothelial cells. **(D)** Violin plots showing expression of *Icam1*, *Vcam1*, and *Cx3cl1* in endothelial cells at the indicated age. **(E)** 8wk old Icam-1$^{-/-}$ and control mice were treated with either vehicle (IgG) or Vcam-1 neutralizing antibody (nAb) for three days. Representative images of the lesser curvature (LC) to evaluate the effects of treatment on Mac^{AIRs}. Scale bar, 30μm. Adjacent graph represents the total number of intimal CD45+ cells in the lesser curvature of treated mice (n=3-4, T-test, ± SD, *p ≤ 0.05, **≤0.01). **(F)** Whole mount, *en face* images staining for CD45 of the aortic arch in 8wk old control and CD11c$^{-/-}$ mice (Scale bar, 500μm). Adjacent graph represents the total number of intimal CD45+ cells in the lesser curvature of control and CD11c$^{-/-}$ mice (n=4, Mann-Whitney T-test, ± SD, *p ≤ 0.05). **(G)** Expression of Pecam-1 mRNA in endothelial cells and Mac^{AIRs} from scRNA-seq (young arch and aged descending A,B libraries; Figure S2). **(H)** Summary illustrating the many molecular players involved in the retention of the Mac^{AIRs} in the tunica intima.

Figure 5.2

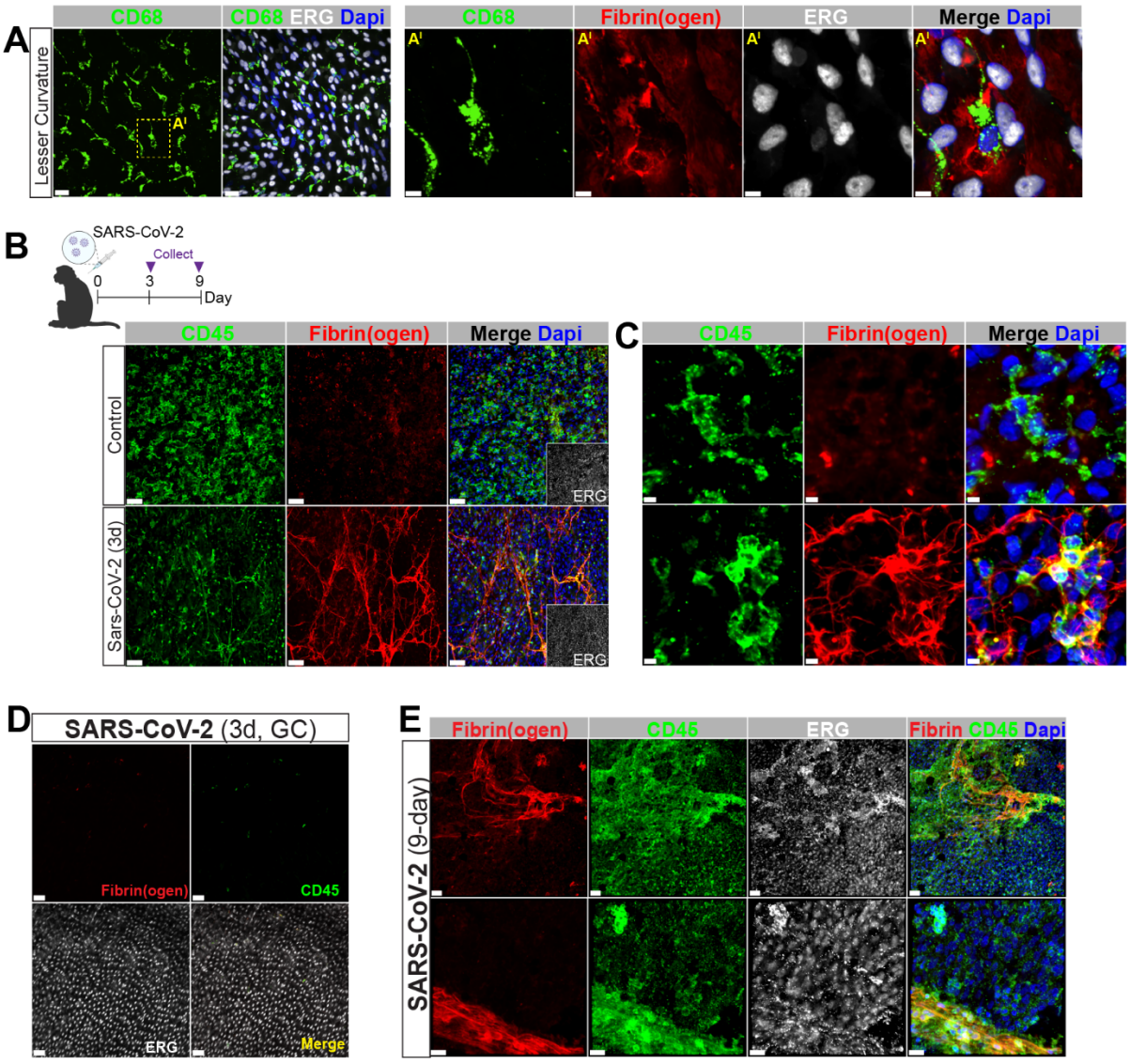

Figure 5.2. SARS-CoV-2 infection causes detachment of intimal myeloid cells and fibrin accumulation in rhesus macaque aortae

(A) En face, whole mount images of healthy, adult rhesus macaque aortae reveal the accumulation of intimal CD68+ myeloid cells (green) and nominal fibrin(ogen) (red) (n=3, Scale bar, 20μm and 7μm (A')). **(B)** Rhesus macaques were challenged with Sars-CoV-2 for up to either 3- or 9- days and aortae were collected for whole-mount *en face* confocal imaging. Images represent the tunica intima of the lesser curvature of the aortic arch of Sars-CoV-2 infected or uninfected controls (n=4, Scale bar, 50μm). See also Figure S7J and S7K. (**C**) Higher

magnification of the intimal immune cells to highlight differences in morphology and fibrin accumulation (n= 3, Scale bar, 5μm).

SUPPLEMENTAL FIGURES

Supplemental Figure 5.1

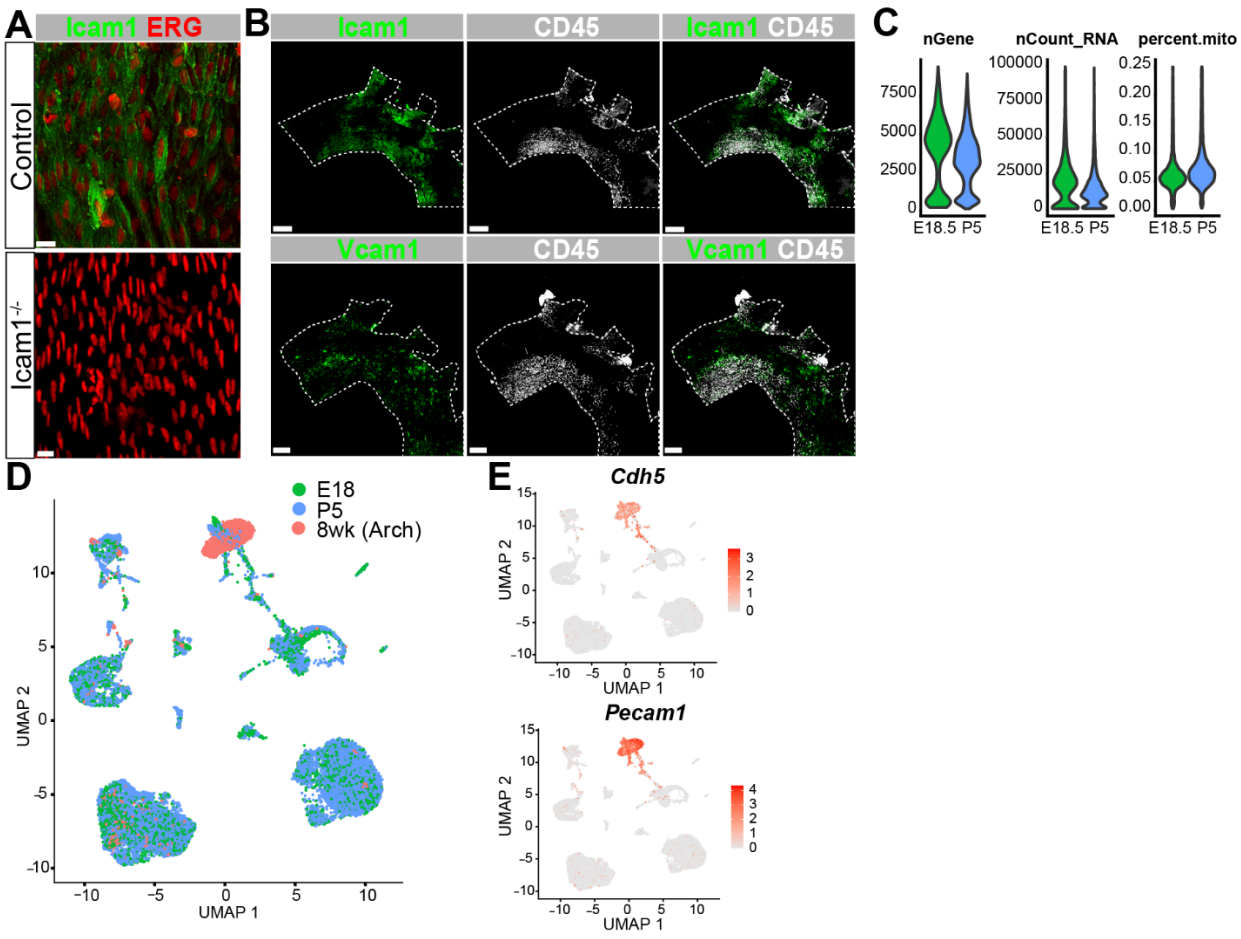

Supplemental Figure 5.1. Turbulent flow creates a unique endothelial cell niche

(A) Validation of Icam-1 antibody using control and Icam-1-/- aortae (Scale bar,15μm). **(B)** Icam-1 and Vcam-1 staining of the aortic arch of adult aortae (Scale bar, 400μm (Icam-1) and 300μm (Vcam-1)). **(C)** Violin plots representing the QC metrics for the E18.5 and P5 aortae scRNAseq libraries: the number of genes per cell (nGene), the absolute number of observed transcripts per cell (nCount_RNA), and percentage of transcripts arising from the mitochondria genome (percent mito). **(D)** UMAP plots of three independent libraries: E18.5, P5, and 8wk (arch – Extended Data Fig. 3) aortae. 8-9 aortae were used per time point. **(E)** UMAP and heat-map style representation of Cdh5 and Pecam1 expression.

REFERENCES

Aid, M., Busman-Sahay, K., Vidal, S.J., Maliga, Z., Bondoc, S., Starke, C., Terry, M., Jacobson, C.A., Wrijil, L., Ducat, S., et al. (2020). Vascular Disease and Thrombosis in SARS-CoV-2-Infected Rhesus Macaques. Cell *183*, 1354–1366.e13.

Chiu, J.-J., and Chien, S. (2011). Effects of disturbed flow on vascular endothelium: pathophysiological basis and clinical perspectives. Physiol. Rev. *91*, 327–387.

Garvin, M.R., Alvarez, C., Miller, J.I., Prates, E.T., Walker, A.M., Amos, B.K., Mast, A.E., Justice, A., Aronow, B., and Jacobson, D. (2020). A mechanistic model and therapeutic interventions for COVID-19 involving a RAS-mediated bradykinin storm. Elife *9*.

Gustafson, E.J., Lukasiewicz, H., Wachtfogel, Y.T., Norton, K.J., Schmaier, A.H., Niewiarowski, S., and Colman, R.W. (1989). High molecular weight kininogen inhibits fibrinogen binding to cytoadhesins of neutrophils and platelets. J. Cell Biol. *109*, 377–387.

Hernandez GE, Ma F, Martinez, G, Firozabadi NB, Salvador J, Juang LJ, Zhao P, López DA, Ardehali R, Beaudin AE, Kastrup CJ, Pellegrini M, Flick M, Iruela-Arispe ML. (2021) Aortic intimal resident macrophages are essential for maintenance of the non-thrombogenic intravascular state. Under Review.

Khan, M.M., Bradford, H.N., Isordia-Salas, I., Liu, Y., Wu, Y., Espinola, R.G., Ghebrehiwet, B., and Colman, R.W. (2006). High-molecular-weight kininogen fragments stimulate the secretion of cytokines and chemokines through uPAR, Mac-1, and gC1qR in monocytes. Arterioscler. Thromb. Vasc. Biol. *26*, 2260–2266.

Nakashima, Y., Raines, E.W., Plump, A.S., Breslow, J.L., and Ross, R. (1998). Upregulation of VCAM-1 and ICAM-1 at atherosclerosis-prone sites on the endothelium in the ApoE-deficient mouse. Arterioscler. Thromb. Vasc. Biol. *18*, 842–851.

Roufaiel, M., Gracey, E., Siu, A., Zhu, S.-N., Lau, A., Ibrahim, H., Althagafi, M., Tai, K., Hyduk, S.J., Cybulsky, K.O., et al. (2016). CCL19-CCR7-dependent reverse transendothelial migration of myeloid cells clears Chlamydia muridarum from the arterial intima. Nat. Immunol. *17*, 1263–1272.

Teuwen, L.-A., Geldhof, V., Pasut, A., and Carmeliet, P. (2020). COVID-19: the vasculature unleashed. Nat. Rev. Immunol. *20*, 389–391.

CONCLUSION

My dissertation research not only challenged several dogmas but also provided key resources that will help advance the fields of vascular and immunology biology. When I joined the Arispe Lab in the summer of 2017, the it was thought that immune cells only interact with the endothelium transiently summoned by acute injury/infection or during instances of pathology, like atherosclerosis. The notion that there could be a resident-myeloid population that resides side-by-side the endothelium in *healthy* aortae was unprecedented, especially since the aorta has been a very well-studied blood vessel. However, thanks to advances in technology, we were able to definitively demonstrate the presence of a tissue-resident macrophage population that is embedded within the endothelium in regions of disturbed blood flow. Importantly we demonstrated that these macrophages play an essential role in clearing fibrin(ogen) deposits and maintaining a non-thrombogenic intravascular surface. The findings emerging from the research shift several important paradigms. One of this is the notion that the endothelial layer is composed by a single cell type facing the lumen, this should now be amended to include macrophages in areas of disturbed blood flow.

Using scRNAseq, we were able to unbiasedly identify these cells as a unique macrophage population found only in the intima of the aorta (Mac^{AIR}). Additionally, using transgenic mouse models, we were able to elucidate their anatomical location, perform lineage tracing, and understand the mode of replenishment of the Mac^{AIRs}. Furthermore, advances in confocal microscopy allowed us to perform whole-mount, en face imaging of aortae, which prompted us to take large scans, painting a picture of the whole aorta and allowing visualization of regions that would normally would have been missed. With this, and our technical ability to dissect aortae from developmental stages, allowed us to show that the closure of the ductus arteriosus promotes the seeding on intima-macrophages. This was an important finding because it proved that Mac^{AIR} accumulation in regions of disturbed blood flow was not pathology provoked but rather, developmentally-programmed.

Fibrin(ogen) deposition in the vascular wall is accepted to be indicative of impaired junctions and exposed basement membrane. My dissertation research revealed for the first time that fibrin(ogen) accumulates in regions of disturbed blood flow during steady-state. This fibrinogen is not associated with breaches of the endothelial barrier that exposes the underlying matrix, it is instead accumulated on the surface of the endothelium and can pose a threat if allowed to form fibrin fibrils as we found that thrombin also accumulates in regions of disturbed flow. These surprising results reveals yet another way the arterial wall is impacted by flow dynamics and the physiological processes in place to counter-act pathological outcomes.

Our findings indicate that intravascular clotting in arteries is constantly antagonized in regions of disturbed flow and “aged” endothelium. While the non-thrombogenic function of vessels was attributed exclusively to the endothelium, the data presented here provides clear evidence that in some regions of the vascular tree, fibrin removal could only be accomplished with aid of macrophages. The relevance of this endothelial-macrophage partnership cannot be overstated as per the devastating intravascular clotting sequelae associated with some conditions including COVID19.

Lastly, patent ductus arteriosus (PDA), which is failure to close the ductus arteriosus immediately post-birth, accounts for approximately 5-10% of all congenital heart defects. Despite our advances in understanding the molecular mechanisms that regulate this process, there is still much unknown. Therefore, I was the first to perform scRNAseq on the ductus arteriosus and aorta at E18.5, P0.5, and P5, creating publically available data sets that allow us understand how the ductus arteriosus undergoes drastic changes at the single-cell level. Making use of this data set, we were able to identify the intermediate filament, Vimentin, as a key protein essential for the closure of the ductus arteriosus. We showed that genetic depletion of Vimentin results in patent ductus arteriosus.

In summary, the breadth of information presented in this dissertation provides a substantial foundation for understanding how hemodynamic changes shape the vascular wall

and how vascular endothelial cells profit from this unique interaction with Mac^{AIRs} to preserve a non-thrombogenic surface, prevent intravascular clotting, and ensure vascular health. As a result, my work has generated novel data that should benefit many fields of study.